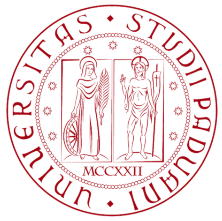

UNIVERSITÀ DEGLI STUDI DI PADOVA

Dipartimento di Fisica e Astronomia "Galileo Galilei"

Corso di Laurea Magistrale in Fisica

Tesi di Laurea

Strong light-matter coupling in tunable doped two-dimensional materials

Relatore

Prof. Luca Salasnich

Correlatore

Prof. Francesca Maria Marchetti

Laureando

Antonio Tiene

Anno Accademico 2017/2018

UNIVERSITÀ DEGLI STUDI DI PADOVA

Dipartimento di Fisica e Astronomia "Galileo Galilei"

Corso di Laurea Magistrale in Fisica

Tesi di Laurea

Strong light-matter coupling in tunable doped two-dimensional materials

Relatore

Prof. Luca Salasnich

Correlatore

Prof. Francesca Maria Marchetti

Laureando

Antonio Tiene

Abstract

This master thesis focusses on studying and developing the theoretical tools necessary to model doped bilayer structures in the presence of strong matter-light coupling. In the last years, an intense research activity was carried towards the search of excitonic superfluidity in semiconductor heterostructures. We briefly review in Chapter 1 the concept of excitons in direct gap semiconductors such as GaAs, with a particular interest to 2D quantum wells. These structures have been recently embedded into a cavity, where the strong coupling between light and matter leads to the formation of new composite strongly coupled matter-light quasiparticles named exciton polaritons. One of the most promising set-ups for the search of excitonic superfluidity is given by electron-hole bilayers. In Chapter 2 we shortly summarize the experimental achievements in this area, describing the most common ways to obtain an electron-hole bilayer. Of particular interest is the technique to realize bilayers with two GaAs quantum well structures and the possibility to control the electron and hole populations in each layer independently, via doping or gating. Novel promising realizations of a similar configuration have also been carried on in graphene bilayers and other pure 2D materials such as transition metal dichalcogenides (TMDCs). In Chapter 3 we review the theoretical description of a condensate of excitons in the limit where the electron and hole densities are the same, and how this description changes when electrons and holes are strongly coupled to light. In particular we offer a brief review on the existing theory of the BCS-BEC crossover for excitonic systems, describing the construction of a wavefunction that interpolates between two extreme limits: in the low density limit, excitons behave as tightly bound bosons and, at low enough temperatures, undergo Bose-Einstein condensation (BEC). In the high density limit, excitons overlap and their fermionic composite nature blocks the occupation of electrons and holes up to the Fermi momentum. In this limit, electron-hole pairs can condense in a form similar to Cooper pairs in conventional BCS superconductors. In this chapter, we will also show how this description changes when electrons and holes strongly couple to cavity light. In Chapter 4 we enter the main topic of this thesis which is about single and double layers of electrons and holes in the extremely imbalanced limit. Considering the extreme imbalanced limit, where there is a single particle in one layer interacting via Coulomb and via the cavity photon field with a Fermi liquid in the other layer, allows to address the problem in a controlled manner. At the same time, for imbalanced mixtures, the inter-specie pairing is frustrated, and one expects more exotic pairing scenarios (such as FFLO spatially modulated phases) to compete with a conventional superfluid phase. In Chapter 4 we thus re-derive the results found in Ref. [49], and extend them considering not only the case in which the Coulomb interaction is fully screened via the Random Phase Approximation (RPA). We also describe in detail the other extreme case where interactions are unscreened. This is also useful in view of the description of materials such as TMDCs, where the screening is not so effective. Chapter 5 is the chapter that contains the majority of original results of this master thesis. The main focus of our research was to characterize the possibility to achieve an FFLO phase in imbalanced electron-hole 2D structures embedded into an optical cavity. While long-range Coulomb interactions promote the formation of the finite momentum

FFLO condensed phase, strong coupling to ultra-low mass photons tends to suppress such a phase (or conversely the formation of an FFLO phase suppresses the coupling to light). The competition between these two effects leads to interesting results, enhanced by the possibility to tune the population densities as well as the energy detuning of the photon field. Our study shows that the FFLO phase survives the coupling to light only at positive detunings and preferentially only for unscreened interations. In presence of screening, the FFLO phase is overtaken by a phase where the finite momentum coupling between electrons and holes is only mediated by finite momentum photons. Further, we have been able to show that the strongest mixing between light and matter only occurs, at intermediated densities, in a small interval of photon detuning, in a phase where polariton condensation occurs, as expected, at zero center of mass momentum.

Contents

Chapter 1

Introduction to excitons and microcavity polaritons

Nowdays, semiconductors have become fundamental in the developing of new technologies. The optical stimulation of these materials can create interesting new bound states of electrons and holes. What we will do in the following chapter is to give a brief introduction on this particular states, especially focusing our attention on a material widely used for the construction of semiconductors: the Gallium Arsenide. The discussion on the above mentioned bound states will be furthermore extended to the case in which a semiconductor is confined in a optical microcavity. We will highlight the presence of new bound states, generated by the interaction between electrons holes and cavity photons. The interest in these states is motivated by the rich research activity with the objective to find the ideal candidate to achieve a Bose Einstein condensation at higher temperatures than the ones obtained until now.

1.1 Direct band gap semiconductor

Semiconductors are a class of materials that have an electrical conductivity value fallin between that of a conductor and an insulator. The electronic properties of a crystalline material are generally determined by the electronic band structure of the material. The highest occupied band, called valence band, is separated from the lowest conduction band by an energy gap. Electrons can be excited from the valence band to the conduction band via thermal excitation or by absorption of light. In our study we are not interested in temperature effects, and so we will focus only on the optical excitation. To schematically describe the optical interaction, in Fig. 1.1 we represent the energy bands structures in the momentum space. At the highest energy of the valence band and the lowest energy of conduction band, the band structure can be locally approximated as $\epsilon_{\mathbf{k},c} = E_g + \frac{\hbar^2\mathbf{k}^2}{2m_c^*}$ and $\epsilon_{\mathbf{k},v} = -\frac{\hbar^2\mathbf{k}^2}{2m_v^*}$ with $m_{v,c}^*$ the two effective masses.

When a photon of energy $\hbar\omega$, greater then the band gap E_g, is incident on a semiconductor, a free electron is created and an empty state is left in the valence band. This empty state could be reinterpreted introducing the concept of electron-hole, a quasi-particle positively charged and with a negative effective mass. So its energy will be $\epsilon_{\mathbf{k},h} = \frac{\hbar^2\mathbf{k}^2}{2m_h^*}$. It is important to notice that in a direct gap semiconductor, the optical excitation could happen with low-momentum transition between electron and photon, this because the minimal-energy state in the conduction band and the maximal-energy state in the valence band have the same lattice momentum. In the indirect gap semiconductors instead, the transition from the highest energy-state of the valence band to the lowest state of the conduction one needs a momentum exchange between photon and electron, because there is a non null relative lattice momentum between the valence band

and the conduction band. We will see that in our study we need low-momentum transitions, and so we will take in account only direct band gap materials.

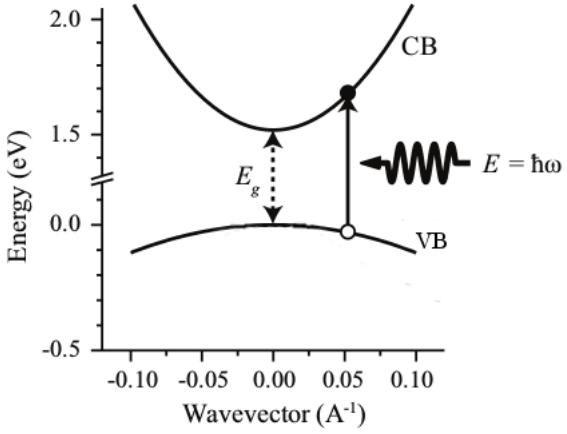

Figure 1.1: Band structure of bulk GaAs showing the conduction (CB) and valence sub-bands (VB). The direct band-gap E_g is indicated. A photon with energy $\mathrm{E} = \hbar\omega$ can excite an electron, indicated by the solid circle, from a valence band to the conduction band leaving behind a hole, indicated by the empty circle, in the valence band. This figure has been adapted from Ref. [1]

1.2 Excitons in bulk semiconductor

The interesting aspect of the optical excitation of GaAs structures is the creation of a bound quasiparticle state between electron and hole. When the electron is excited into the conduction band, and the hole appears in the valence band, in GaAs (and also in other semiconductors) the attractive Coulomb interaction could create a bounded electron-hole pair, known as exciton. This quasiparticle has an energy equal to the band gap energy minus the binding energy of the exciton E_0. Excitons may be treated in two limiting cases, depending on the properties of the material. In materials with a small dielectric constant, the Coulomb interaction is strong, thus the exciton tends to be small. This is the Frenkel exciton, named after Yakov Frenkel, which studied the effect of Coulomb attraction between electron-hole pair in the same crystal cell [2]. Instead, for a reduced Coulomb interaction, the result is the Wannier exciton [3], that has a larger radius – of the order of tens of lattices constants – Fig. 1.2. For GaAs, excitons are the Wannier-Mott type, due to the high dielectric constant.

The wave function $\psi(\mathbf{r}_e, \mathbf{r}_h)$ of an exciton is the solution of a Schrödinger equation similar to the hydrogen one, with different masses and dielectric constant

$$\left[\frac{\hat{\mathbf{p}}_e^2}{2m_e} + \frac{\hat{\mathbf{p}}_h^2}{2m_h} - \frac{e^2}{4\pi\epsilon|\mathbf{r}_e - \mathbf{r}_h|}\right]\psi(\mathbf{r}_e, \mathbf{r}_h) = (E - E_g)\psi(\mathbf{r}_e, \mathbf{r}_h)\ . \tag{1.1}$$

Changing variables

$$\mathbf{r} = \mathbf{r}_e - \mathbf{r}_h \tag{1.2a}$$

$$\mathbf{R} = \frac{m_e\mathbf{r}_e + m_h\mathbf{r}_h}{m_e + m_h}\ , \tag{1.2b}$$

Eq. (1.1) becomes

$$\left[-\frac{\hbar^2\nabla^2(\mathbf{R})}{2M} - \frac{\hbar^2\nabla^2(\mathbf{r})}{2\mu} - \frac{e^2}{4\pi\epsilon r}\right]\psi(\mathbf{r}, \mathbf{R}) = (E - E_g)\psi(\mathbf{r}, \mathbf{R})\ . \tag{1.3}$$

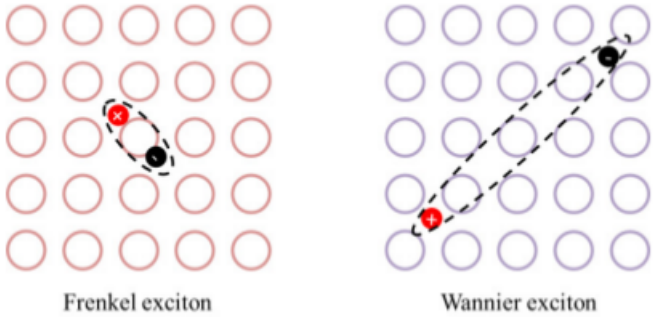

Figure 1.2: Excitons with different radii. On the left the Frenkel exciton, on the right the Wannier exciton, with bigger radius and lower binding energy. Picture taken from Ref. [4]

with $\frac{1}{\mu} = 2\left(\frac{1}{m_e} + \frac{1}{m_h}\right)$ half of the reduced mass. The new coordinate systems allows to factorize the wave function into a product of functions depending on $\mathbf{R}$ and $\mathbf{r}$. For the center of mass part, the solution is a planar wave with energy $\hbar^2 K^2/2M$. The equation for the relative coordinate is

$$\left[-\frac{\hbar^2\nabla^2(\mathbf{r})}{2\mu} - \frac{e^2}{4\pi\epsilon r}\right]\phi(\mathbf{r}) = -E_0\phi(\mathbf{r})\ . \tag{1.4}$$

Solving Eq. (1.4) we obtain the excitonic energy spectrum. For the ground state $\phi(\mathbf{r}) = \varphi_{1s}^{3D}(\mathbf{r}) = \frac{1}{\sqrt{\pi a_B^3}}\exp(-r/a_0)$ we have

$$E = E_g + \frac{\hbar^2 K^2}{2M} - E_0 \tag{1.5}$$

$$E_0 = \frac{\mu e^4}{32\pi^2\hbar^2\epsilon_r^2\epsilon_0^2} = \frac{\hbar^2}{2\mu a_0^2} \tag{1.6}$$

$$a_0 = \frac{4\pi\epsilon_r\epsilon_0\hbar^2}{\mu e^2}\ . \tag{1.7}$$

For a typical exciton in GaAs, $E_0 = 4.7$ meV and $a_0 = 115\mathring{A}$ [5].

1.3 Excitons in confined systems: quantum wells

Nowadays it is possible to realize low-dimensional semiconductor structures, where electrons and holes are confined in one or two dimensions [6]. Therefore, it is interesting to explore how the exciton properties change due to the quantum confinement. Whereas without confinement, the total energy of the exciton is simply the energy of the free electron-free hole pair (i.e. the band gap) minus the exciton binding energy E_0, in a confined system there are additional components due to the electron and hole confinement energies. For our purposes, we focus our attention on a 2D system, realized with a thin layer – a few nanometers thick – of a low band gap semiconductor, sandwiched between a higher band gap material, which acts as the barrier [7]. One of the most widely used QW structure is the combination between gallium arsenide (GaAs) and the alloy $Al_xGa_{1-x}As$. The name quantum well derives from the quantization of the light modes introduced by the reduced dimension of the system. In such a geometry, the translational symmetry is broken along the direction orthogonal to the semiconductor plane. As a consequence, the total wavevector $\mathbf{k}$ is no more conserved in these structures, while the only conserved quantity is the in-plane component. The effect of confinement becomes meaningful when the size is comparable to the spatial extent of the exciton [8], and it mainly changes the

Bohr radius, decreasing it with respect the unconfined case, and consequently increasing the binding energy of the exciton [9, 10].

To demonstrate this, let's consider the Schrödinger equation for an exciton in a 2D system

$$\left[\frac{\hat{\mathbf{p}}_e^2}{2m_e} + \frac{\hat{\mathbf{p}}_h^2}{2m_h} - \frac{e^2}{4\pi\epsilon|\mathbf{r}_e - \mathbf{r}_h|} + V_e(z_e) + V_h(z_h)\right]\psi(\mathbf{r}_e, \mathbf{r}_h) = (E - E_g)\psi(\mathbf{r}_e, \mathbf{r}_h)\ , \tag{1.8}$$

where $V_e(z_e)$ and $V_h(z_h)$ are step-like quantum-well confining potentials for electrons and holes along the z axis. Solving this equation is not easy. It is possible to find different suggestions in the literature [11, 12]. For example using a variational approach over different trial function ($\mathbf{r} = (\boldsymbol{\rho}, z)$)

$$\psi(\mathbf{r}_e, \mathbf{r}_h) = F(\mathbf{R})\phi(\boldsymbol{\rho})\chi_e(z_e)\chi_h(z_h)\ , \tag{1.9}$$

where the exciton centre of mass coordinate $\mathbf{R}$ and the relative in-plane radius-vector of electron and hole $\boldsymbol{\rho}$ are

$$\boldsymbol{\rho} = \boldsymbol{\rho}_e - \boldsymbol{\rho}_h \tag{1.10a}$$

$$\mathbf{R} = \frac{m_e\mathbf{r}_e + m_h\mathbf{r}_h}{m_e + m_h}\ . \tag{1.10b}$$

Eq. (1.9) describes the exciton centre of mass, the relative in-plane and normal to the plane components of motion. The normalization conditions

$$\int |\chi_e(z_e)|^2 dz_e = 1, \tag{1.11}$$

$$\int |\chi_h(z_h)|^2 dz_h = 1, \tag{1.12}$$

$$\int_0^\infty |\phi(\rho)|2\pi\rho d\rho = 1 \tag{1.13}$$

$$\int_0^\infty |F(R)|^2 2\pi R dR = 1\ . \tag{1.14}$$

After substitution of Eq. (1.9) and integration over R, Eq. (1.8) becomes:

$$\left\{-\frac{\hbar^2}{2m_e}\frac{\partial^2}{\partial z_e^2} - \frac{\hbar^2}{2m_h}\frac{\partial^2}{\partial z_h^2} - \frac{1}{\rho}\frac{\partial}{\partial\rho}\left(\frac{\hbar^2}{2\mu}\rho\frac{\partial}{\partial\rho}\right) - \frac{e^2}{4\pi\epsilon\sqrt{\rho^2 + (z_e - z_h)^2}} + V_e(z_e) + V_h(z_h) - E + E_g\right\}\phi(\rho)\chi_e(z_e)\chi_h(z_h) = 0\ . \tag{1.15}$$

Eq. (1.15) can be transformed into a system of three coupled differential equations. To obtain the equation for $\phi(\rho)$ one have to multiply for $U_e^*(z_e)U_h^*(z_h)$ and integrating over z_e and z_h. In the same way to obtain the equation for $\chi_{e,h}(z_{e,h})$ one have to multiply for $f^*(\rho)U_{e,h}^*(z_{e,h})$ and then integrate over ρ and $z_{e,h}$. The resulting coupled equations are

$$-E_0^{QW}\phi(\rho) = \left\{-\frac{1}{\rho}\frac{\partial}{\partial\rho}\left(\frac{\hbar^2}{2\mu}\rho\frac{\partial}{\partial\rho}\right) - \frac{e^2}{4\pi\epsilon}\int\int\frac{|\chi_e(z_e)|^2|\chi_h(z_h)|^2}{\sqrt{\rho^2 + (z_e - z_h)^2}}dz_e dz_h\right\}\phi(\rho) \tag{1.16}$$

$$E_{e,h}\chi_{e,h}(z_{e,h}) = \left\{-\frac{\hbar^2}{2m_{e,h}}\frac{\partial^2}{\partial z_{e,h}^2} + V_{e,h} - \frac{e^2}{4\pi\epsilon}\int\int\frac{|\phi(\rho)|^2|\chi_{h,e}(z_{h,e})|^2}{\sqrt{\rho^2 + (z_e - z_h)^2}}2\pi\rho d\rho dz_{h,e}\right\}\chi_{e,h}(z_{e,h})\ , \tag{1.17}$$

where E_0^{QW} is modulus of the exciton binding energy for a quantum well and $E_{e,h}$ is the electron/hole confinement energy. In the ideal 2D case $|\chi_{e,h}(z_{e,h})|^2 = \delta(z_{e,h})$, and so

$$\left\{-\frac{\hbar^2}{2\mu}\frac{1}{\rho}\frac{\partial}{\partial\rho}\left(\rho\frac{\partial}{\partial\rho}\right) - \frac{e^2}{\epsilon\rho}\right\}\phi(\rho) = -E_0^{2D}\phi(\rho)\ , \tag{1.18}$$

which is now exactly solvable (the 2D hydrogen atom problem), and it is equivalent to

$$\phi(\rho) = \varphi_{1s}^{2D}(\rho) = \sqrt{\frac{2}{\pi}}\frac{1}{a_0^{2D}}\exp(-\rho/a_0^{2D})\ , \tag{1.19}$$

with

$$E_0^{2D} = \frac{\mu e^4}{8\pi^2\hbar^2\epsilon_r^2\epsilon_0^2} = 4E_0 \tag{1.20}$$

$$a_0^{2D} = \frac{2\pi\epsilon_r\epsilon_0\hbar^2}{\mu e^2} = \frac{a_0}{2}\ . \tag{1.21}$$

In a more realistic case, without an infinite well, the binding energy could be found using a trial function

$$\phi(\rho) = \sqrt{\frac{2}{\pi}}\frac{1}{a}exp(-\rho/a)\ , \tag{1.22}$$

where a is now a variational parameter, and minimizing

$$E_X^{QW}(a) = -\frac{\hbar^2}{2\mu a^2} + \frac{e^2}{4\pi\epsilon}\int\int\int\frac{|\phi(\rho)|^2|\chi_e(z_e)|^2|\chi_h(z_h)|^2}{\sqrt{\rho^2+(z_e-z_h)^2}}2\pi\rho d\rho dz_e dz_h\ , \tag{1.23}$$

where E_0^{QW} ranges from E_0 to E_0^{2D}.

1.3.1 The electron-hole problem: variational approach

The very same results can be re-obtained by making use of a variational approach. In the following chapters this method will be generalized to the case of finite density of either electrons and holes. We now consider the following Hamiltonian in the momentum space (we set $\hbar = 1$)

$$\hat{H} = \hat{H}_0 + \hat{H}_{int} \tag{1.24}$$

$$\hat{H}_0 = \sum_{\mathbf{k},\sigma=e,h}\epsilon_{\mathbf{k},\sigma}c^\dagger_{\mathbf{k},\sigma}c_{\mathbf{k},\sigma} \tag{1.25}$$

$$\hat{H}_{int} = -\frac{1}{\Omega}\sum_{\mathbf{kk'q}}\frac{2\pi e^2}{\epsilon\mathbf{q}}c^\dagger_{\mathbf{k},e}c^\dagger_{\mathbf{k'},h}c_{\mathbf{k'+q},h}c_{\mathbf{k-q},e}\ , \tag{1.26}$$

where $c^\dagger_{\mathbf{k},e}$ and $c^\dagger_{\mathbf{k},h}$ are the creation operators for the electron and the hole and $\epsilon_{\mathbf{k},e/h}$ the respective energy. The variational molecular ground state chosen is

$$|\Psi\rangle = \frac{1}{\sqrt{\Omega}}\sum_{\mathbf{k}>k_F}\varphi_{\mathbf{k}}c^\dagger_{-\mathbf{k},h}c^\dagger_{\mathbf{k},e}\left|0\right\rangle_e\otimes\left|0\right\rangle_h\ , \tag{1.27}$$

where $|0\rangle_{e,h}$ are the vacuum states. After the minimization of the expectation value $\langle\Psi|\left(\hat{H}-E\right)|\Psi\rangle$ with respect to the complex amplitude $\varphi_{\mathbf{k}}$, one obtains an eigenvalue equation for the exciton energy E:

$$E\varphi_{\mathbf{k}} = \left(\epsilon_0 - \mathbf{k}, h + \epsilon_{\mathbf{k},e}\right)\varphi_{\mathbf{k}} - \frac{1}{\Omega}\sum_{\mathbf{k'}}\frac{2\pi e^2}{\epsilon(\mathbf{k}-\mathbf{k'})}\varphi_{\mathbf{k'}}\ . \tag{1.28}$$

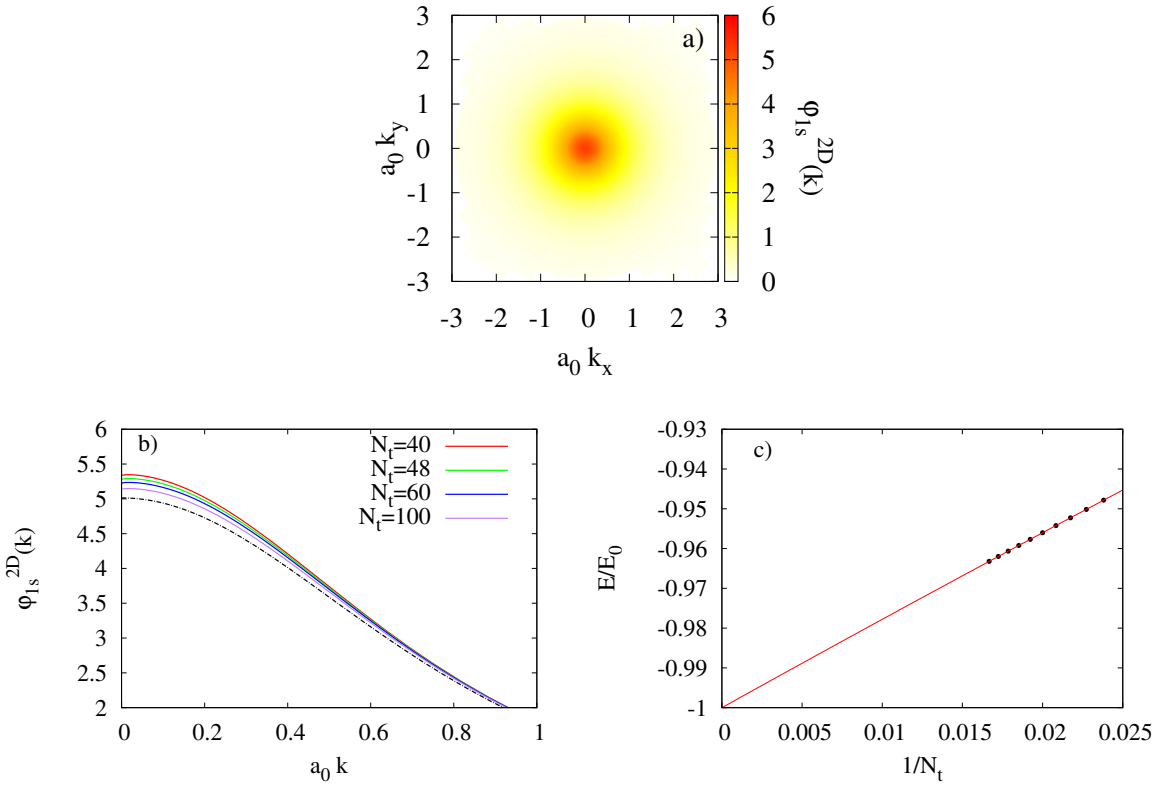

Figure 1.3: a) 2D map of the rescaled exciton wavefunction $\varphi_{1s}^{2D}(\mathbf{k})$ as a function of $\mathbf{k}$. b) Excitonic eigenfunction $\varphi_{1s}^{2D}(\mathbf{k})$ as a function of $|\mathbf{k}|$ for different values of N_t and $N_k = 3N_t/2$. The numerical eigenvectors tend to the expected exact solution (1.29) – dashed line – for an increasing number of points. In particular, for $N_t \to \infty$, the fitted parameter $a_0^{\text{fitted}}/a_0 \to 1.003$. c) Convergence of the excitonic energy, measured with respect E_0, to the expected value -1, as a function of N_t.

where for simplicity we set E_g to zero. This is exactly Eq. (1.18) in the momentum space. In order to solve this eigenvalues problem, we convert this equations into a numerical solvable matrix equation, through the Gauss-Legendre quadrature, described in Appendix A. In Fig. 1.3 the numerical results of our calculations are shown. In Fig. 1.3 a) the resulting wave function is depicted

$$\varphi_{1s}^{2D}(\mathbf{k}) = \frac{2\sqrt{2\pi}a_0}{(1+(a_0 k)^2)^{3/2}} \tag{1.29}$$

However our method depends on the number of points chosen for the Gauss-Legendre quadrature. In 1.3 b) the calculated excitonic wavefunction is plotted as a function of $a_0 k$, for different selected number of points. The numerical eigenvectors tend to the expected exact solution (1.29) increasing the number of points N_t used. In particular, for $N_t \to \infty$, the fitted parameter $a_0^{\text{fitted}}/a_0 \to 1.003$. In Fig. 1.3 c) we show the convergence of the excitonic energy, measured with respect E_0, to the expected value -1 increasing the number N_t of point used for the Gauss-Legendre quadrature

1.4 Optical microcavities: distributed Bragg reflectors

The exciton is stable for a short period of time. The excited electron can recombine with the hole by transferring energy through photon emission. So exciton has a finite lifetime, of the order of nanoseconds, influenced by many factors including temperature and scattering with other excitons. In general, emission of light can occur in two distinct regimes, depending on the coupling between the active medium and the electromagnetic field. In the weak coupling a photon produced has a negligible probability of being reabsorbed by the medium. Thus the excitation is dissipated. In the strong coupling, the photon can re-excite the medium and creating new mixed states, superposition of exciton and cavity photons. This coupling is difficult to achieve, because the frequency of emission and absorption has to overwhelm damping rates. For this reason strong coupling is favored as soon as an active medium is inserted inside a cavity.

Optical microcavities (see Fig. 1.4) are optical resonators close to, or below, the dimension of the wavelength of light. An example is the well-know Fabry-Pérot interferometer [13], a microcavity in which two high reflectivity mirrors – with a refraction index n – are brought at a distance L, where the resulting cavity mode are equally spaced in frequency. After each one-roud trip, the photon beam gain a phase shift of

$$\delta = \frac{2\pi k_\perp}{\lambda} = \left(\frac{2\pi}{\lambda}\right) 2nL\cos\theta \tag{1.30}$$

with respect to the previous beam. If L is equal to a integer number of wavelength λ, the interference is constructive, and hence the cavity frequency increases. In the ideal case, we can approximate the Fabry-Pérot interferometer as an infinite well, perfectly confining the photon mode. Thus in this case $k = \frac{m\pi}{L}$, and the normal modes of the system are

$$\phi_m(x) = \sqrt{\frac{2}{L}}\sin(\frac{m\pi}{L}x)\ , \tag{1.31}$$

where m is an integer number. So now one can rewrite the dispersion relation in the following way ($\mathbf{k} = (\boldsymbol{\kappa}, k_z)$)

$$\omega_{\mathbf{k},C} = \frac{c|k|}{n} = \frac{c}{n}\sqrt{|\kappa|^2 + k_z^2} = \frac{c}{n}\sqrt{|\kappa|^2 + \left(\frac{m\pi}{L}\right)^2}\ , \tag{1.32}$$

where z is the confinement axis. Supposing a strong confinement, $k_z \gg |\kappa|$

$$\omega_{\kappa,C} = \frac{c}{n}\frac{m\pi}{L}\sqrt{1 + \left(\frac{L}{m\pi}\right)^2 |\kappa|^2} \approx \frac{c}{n}\frac{m\pi}{L}\left[1 + \frac{1}{2}\left(\frac{L}{m\pi}\right)^2 |\kappa|^2\right] = \omega_{0,C} + \frac{|\kappa|^2}{2m_C^*}\ , \tag{1.33}$$

with

$$\omega_{0,C} = \frac{c}{n}\frac{m\pi}{L} = \frac{c^2}{n^2}m_C^* \tag{1.34}$$

$$m_C^* = \frac{n}{c}\frac{m\pi}{L}\ . \tag{1.35}$$

The dispersion relation is now quadratic with respect to the wavevector, and the photon gain an effective mass m_C^* that depends on the cavity length. Of course there are always possible losses from the mirror, and so an infinite well approximation is not reliable. To increase the reflection efficiency, a widely used mirror is the DBR, made of different layers of alternating high and low refractive indices. The most frequently used design is that of a quarter-wave mirror, where each optical layer thickness – a and b respectivelly – are chosen so that

$$n_a a = n_b b = \frac{\lambda}{4}\ . \tag{1.36}$$

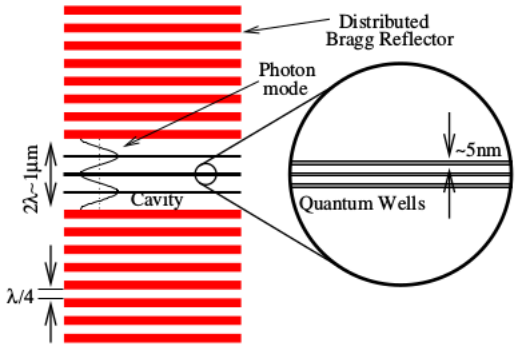

Figure 1.4: Schematic representation of a microcavity, using distributed Bragg reflector stacks. Image taken from Ref. [14]

The light reflections of this layers create a destructively interference, creating a stop band for transmission [12]. In this configuration, the effective length of the microcavity $\tilde{L}$ is extended up the stop band. There are some key physical measures that characterize the cavity quality.

The quality factor The quality factor, known as Q-factor, is the ratio of the resonance cavity wavelength λ and the FWHM of the resonance:

$$Q = \frac{\lambda}{\delta\lambda} \tag{1.37}$$

This factor measures the number of photon's travels inside the cavity before going out. So it is the rate at which optical energy decays from within the cavity. Another related element is the finesse

$$\mathcal{F} = \frac{\pi(R_1 R_2)^{1/4}}{1-(R_1 R_2)^{1/2}} \,, \tag{1.38}$$

that is an intrinsic measure of the confinement ability of the cavity, excluding propagation effects – R_1 and R_2 represents the reflectivity of the mirrors. Q and $\mathcal{F}$ are related from the following identity

$$Q = \frac{n_{eff} L_C}{\lambda} \mathcal{F} \,, \tag{1.39}$$

where n_{eff} is the effective index of refraction of the cavity, and L_C the length [15].

Field enhancement Due to confinement, the strenght of electric field is enhanced compared to that in free space. If R is the total reflectivity

$$\frac{E_{cavity}}{E_{free}} \approx \frac{1}{1-R} \,. \tag{1.40}$$

Tuneability and mode separation We see that the longitudinal modes, and the cavity photon energy as consequence, is inversely proportional to the cavity length. An useful parameter to introduce is the cavity detuning, defined as

$$\delta = \omega_{0,C} - \omega_{0,X} \,, \tag{1.41}$$

where $\omega_{0,C}$ and $\omega_{0,X}$ are respectively the photon and exciton energy, at zero momentum. So using a cavity with two mirrors, where one is inclined respect an axis (wedged mirror) one obtains different lengths, and so a different detunings, along the cavity. Through a localized pump is possible to exactly select the detuning needed.

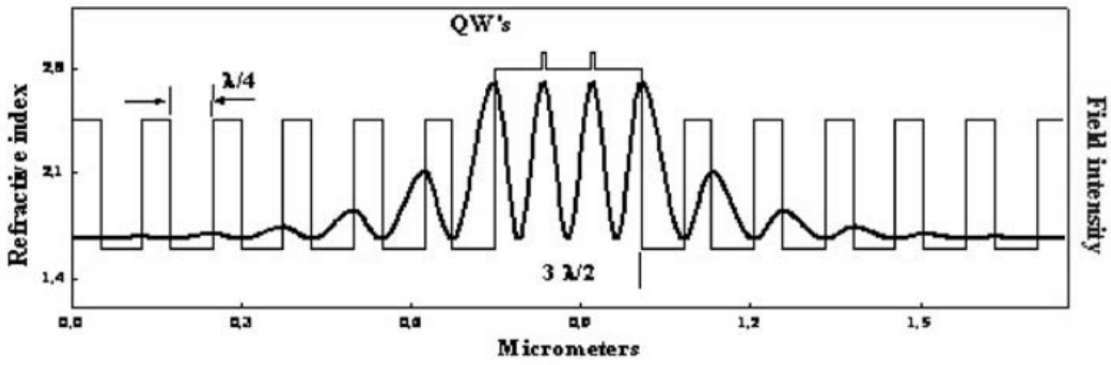

Figure 1.5: Refractive-index profile and intensity of electric field of the eigenmode of a typical planar microcavity. The effective cavity length is extended up to the stop band. Ref. [12]

Purcell effect When an emitter is put inside a microcavity, the spontaneous emission is enhanced. The enhancement of a quantum system's spontaneous emission rate by its environment is known as the Purcell effect [16]. The emission lifetime in the cavity τ, with respect to the free space one, τ_0 is proportional to the Purcell factor

$$\frac{\tau_0}{\tau} \propto F_P = \frac{3}{4\pi^2}\frac{\lambda_c^3}{n^3}\frac{Q}{V_{eff}}\,, \tag{1.42}$$

with n the refractive index of the cavity, V_{eff} the effective volume, Q the quality factor and λ_c the cavity photon wavelength.
The ratio Q/V_{eff} is crucial to allows the emitter to emit much faster then the decay ratio.

Strong coupling Embedding a resonant absorber inside a microcavity, the regime of strong coupling can be reached. One approach to describe theoretically the strong-coupling effects is to consider the coupled-oscillators model, where the dielectric polarization generated by the exciton $\mathbf{P}$ and the electric field of the cavity mode $\mathbf{E}$ are treated semi.classically, and are assumed to obey the oscillator like equations

$$i\dot{\mathbf{P}} = (\omega_X - i\gamma)\,\mathbf{P} + g\mathbf{E}, \tag{1.43}$$

$$i\dot{\mathbf{E}} = (\omega_C - i\kappa)\,\mathbf{E} + g\mathbf{P}, \tag{1.44}$$

where γ and κ are the dampings, respectiveley of the exciton and the cavity photon, g is the coupling strenght and $\omega_{X/C}$ are the exciton and cavity resonances. For the harmonic time dependence of $\mathbf{P}, \mathbf{E} \propto e^{-i\omega t}$, the eigenfrequency ω can be found solving the coupled Schrödinger equations, obtaining

$$(\omega - \omega_X + i\gamma)\,(\omega - \omega_C + i\kappa) = g^2 \tag{1.45}$$

In the most trivial and instructive case $\omega_C = \epsilon_X = \omega_0$, and the previous equation can be solved as

$$\omega_\pm = \omega_0 - i\frac{\gamma+\kappa}{2} \pm \frac{\Omega_R}{2} \tag{1.46}$$

Here $\Omega_R = \sqrt{4g^2 - (\gamma-\kappa)^2}$ is the Rabi frequency. In the strong coupling $g > |\gamma - \kappa|/2$, and so Ω_R is real, and it is linked with the so called vacuum Rabi splitting $\hbar\Omega_R$ [17], the energy splitting between the two resulting frequencies $\omega_\pm$. In the weak coupling limit is imaginary, and so the coupling to light affects only the dumping rates, enhancing the emission, and so generating a Purcell effect.

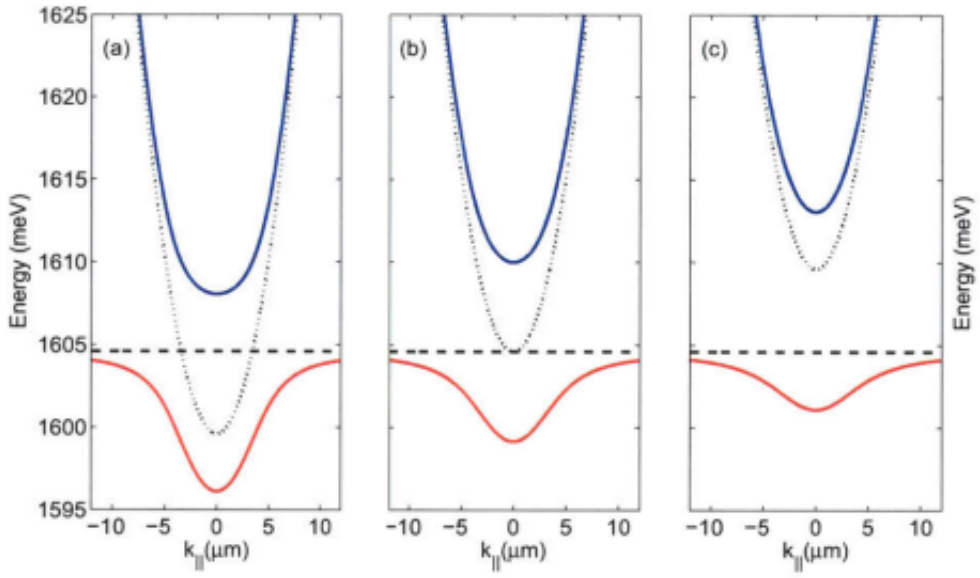

Figure 1.6: Dispersion curves of polariton modes at different cavity detunings (a) δ = -5 meV, (b) $\delta = 0$ meV, and (c) $\delta = 5$ meV. The dotted lines show the cavity photon modes, and the dashed lines the bare exciton modes. The blue and red solid lines indicate the upper polariton (UP) and lower polariton (LP) branches, respectively. This figure has been taken from Ref.[15]

1.5 Coupling to light: coupled oscillator model

There are different theoretical approach to study a QW in an optical microcavity. Considering the exciton as tightly bound boson, the dynamics of photons and excitons in a 2D microcavity are described by the Hamiltonian (we set $\hbar = 1$)

$$\begin{aligned}
\hat{H} &= \hat{H}_X + \hat{H}_C + \hat{H}_{X-C} \\
\hat{H}_X &= \int \frac{d^2\mathbf{k}}{(2\pi)^2} \omega_{\mathbf{k},X} c^\dagger_{\mathbf{k},X} c_{\mathbf{k},X} \\
\hat{H}_C &= \int \frac{d^2\mathbf{k}}{(2\pi)^2} \omega_{\mathbf{k},C} c^\dagger_{\mathbf{k},C} c_{\mathbf{k},C} \\
\hat{H}_{X-C} &= \int \frac{d^2\mathbf{k}}{(2\pi)^2} \frac{\Omega_R}{2} [c^\dagger_{\mathbf{k},X} c_{\mathbf{k},C} + h.c.] \,,
\end{aligned} \tag{1.47}$$

where $c^{(\dagger)}_{\mathbf{k},C}$ and $c^{(\dagger)}_X(\mathbf{k})$ are the annihilation (creation) operator for the cavity photon and for the excitons respectively, $\omega_{\mathbf{k},C}$ and $\omega_{\mathbf{k},X}$ their energy, and Ω_R the Rabi energy. The Hamiltonian could be diagonalized through the following orthogonal transformation, called Hopfield transformation [18],

$$c_{\mathbf{k},LP} \equiv \cos\theta_{\mathbf{k}} c_{\mathbf{k},X} - \sin\theta_{\mathbf{k}} c_{\mathbf{k},C} \tag{1.48}$$

$$c_{\mathbf{k},UP} \equiv \sin\theta_{\mathbf{k}} c_{\mathbf{k},X} + \cos\theta_{\mathbf{k}} c_{\mathbf{k},C} \,, \tag{1.49}$$

with the so-called Hopfield coefficients $\cos\theta_{\mathbf{k}}$ and $\sin\theta_{\mathbf{k}}$. The transformation is canonical, and the operators $c_{\mathbf{k},LP/UP}$ follow a bosonic algebra such as $c_{\mathbf{k},X}$ and $c_{\mathbf{k},C}$. They are annihilation operators of two bosonic quasiparticles that are a superposition of an exciton and a photon in the strong coupling regime, called lower polariton (LP) and upper polariton (UP) [19, 20].

From the diagonalized Hamiltonian

$$\hat{H} = \int \frac{d^2\mathbf{k}}{(2\pi)^2} \sum_{\sigma} [\omega_{\mathbf{k},LP} c^{\dagger}_{\mathbf{k},LP} c_{\mathbf{k},LP} + \omega_{\mathbf{k},UP} c^{\dagger}_{\mathbf{k},UP} c_{\mathbf{k},UP}] \ , \tag{1.50}$$

the upper and lower polariton (see Fig. 1.6) dispersion is

$$\omega_{\mathbf{k},UP/LP} = \frac{\omega_{\mathbf{k},C} + \omega_{\mathbf{k},X}}{2} \pm \left[\frac{\Omega_R^2}{4} + \frac{(\omega_{\mathbf{k},C} - \omega_{\mathbf{k},X})^2}{4} \right]^{1/2} \ . \tag{1.51}$$

If $\omega_{\mathbf{k},C} - \omega_{\mathbf{k},X} = 0$, the Rabi energy Ω_R is exactly the Rabi splitting between low and upper polariton. As seen in Fig. 1.6, the polariton dispersion at small $\mathbf{k}$ depends on the detuning, going from a photon-like behavior with negative detuning, to a more excitonic-like one for positive detuning. The Hopfield coefficient are related to the mixing angle, and their square correspond to the photon or exciton fraction of the polariton.

$$|\cos\theta_{\mathbf{k}}|^2 = \frac{1}{2}\left(1 + \frac{\omega_{\mathbf{k},C} - \omega_{\mathbf{k},X}}{\sqrt{(\omega_{\mathbf{k},C} - \omega_{\mathbf{k},X})^2 + \Omega_R^2}}\right) \tag{1.52}$$

$$|\sin\theta_{\mathbf{k}}|^2 = \frac{1}{2}\left(1 - \frac{\omega_{\mathbf{k},C} - \omega_{\mathbf{k},X}}{\sqrt{(\omega_{\mathbf{k},C} - \omega_{\mathbf{k},X})^2 + \Omega_R^2}}\right) \tag{1.53}$$

$$\tag{1.54}$$

From the curvatures of the dispersion relations Eq.(1.51), is possible to obtain the effective masses $m_{LP/UP}$.

1.5.1 The electron-hole-photon problem

Instead of considering the exciton as a tightly bound boson, let us consider the actual problem of interacting electron-hole-photon. The Hamiltonian of the problem, in the momentum space, is

$$\hat{H} = \hat{H}_0 + \hat{H}_{int} + \hat{H}_{e-h-ph} \tag{1.55}$$

$$\hat{H}_0 = \sum_{\mathbf{k},\sigma=e,h} \epsilon_{\mathbf{k},\sigma} c^{\dagger}_{\mathbf{k},\sigma} c_{\mathbf{k},\sigma} + \sum_{\mathbf{q}} \omega_{\mathbf{q},C} c^{\dagger}_{\mathbf{q},C} c_{\mathbf{q},C} \tag{1.56}$$

$$\hat{H}_{int} = -\frac{1}{\Omega} \sum_{\mathbf{k}\mathbf{k}'\mathbf{q}} \frac{2\pi e^2}{\epsilon q} c^{\dagger}_{\mathbf{k},e} c^{\dagger}_{\mathbf{k}',h} c_{\mathbf{k}'+\mathbf{q},h} c_{\mathbf{k}-\mathbf{q},e} \tag{1.57}$$

$$\hat{H}_{e-h-ph} = \frac{g}{\sqrt{\Omega}} \sum_{\mathbf{k},\mathbf{q}} \left(c^{\dagger}_{\mathbf{k},e} c^{\dagger}_{\mathbf{q}-\mathbf{k},h} c_{\mathbf{q},C} + \text{h.c.} \right) \ , \tag{1.58}$$

where g is the coupling strenght. In this model the interaction between light and matter is a simple contact interaction. However in principle the sum over $\mathbf{k}$ is infinite, and so after a Fourier transformation of this term in the real space, one expects a UV divergence. A way to solve this problem is considering a renormalization of the interaction. Taking

$$\hat{H}_{e-h-ph} = \frac{g}{\sqrt{\Omega}} \sum_{\mathbf{k},\mathbf{q}} e^{-(\frac{k}{k_c})^2} \left(c^{\dagger}_{\mathbf{k},e} c^{\dagger}_{\mathbf{q}-\mathbf{k},h} c_{\mathbf{q},C} + \text{h.c.} \right) \ , \tag{1.59}$$

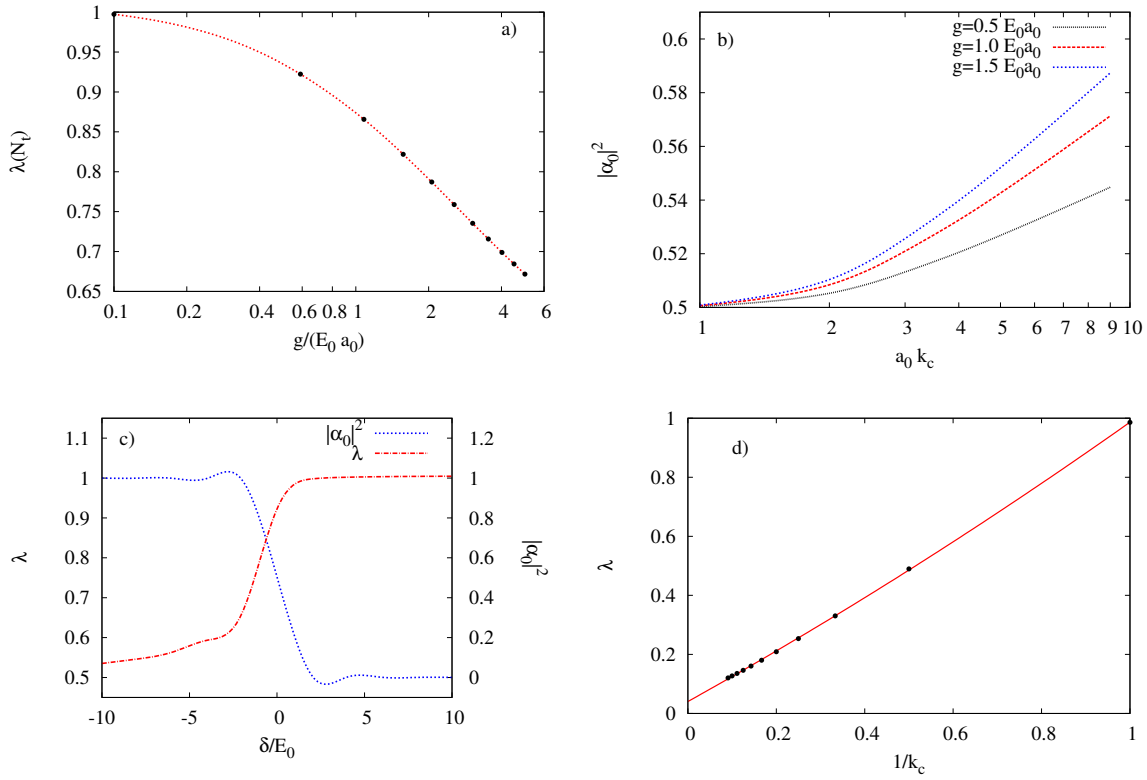

Figure 1.7: a) λ factor as a function of the coupling strenght g, evaluated at $\delta = 0$ $k_C = 2/a_0$ using a fixed number of point N_t in the Gauss-Legendre quadrature. b) Photon fraction as a function of momentum cut-off, for different values of g. $\delta = 0$. c) Comparison between the photon fraction and the λ factor - now extrapolated for $N_t \to \infty$ (with $g = 0.5E_0a_0$ and $k_C = 2/a_0$). d) λ as a function of $1/k_c$ in the photonic regime ($\delta = -100$). It is almost a linear dependency.

where the momentum cutoff is $e^{-(k/k_c)^2}$. Through the Fourier transformation of $\hat{H}_{eh-ph}$

$$\hat{H}_{eh-ph}(k_c) = \frac{gk_c}{\sqrt{2\Omega}} \int d\mathbf{x} \int d\mathbf{x}' e^{-\left[\frac{k_c(\mathbf{x}-\mathbf{x}')}{2}\right]^2} \hat{\psi}_1^\dagger(\mathbf{x})\hat{\psi}_2^\dagger(\mathbf{x}')\hat{\phi}(\mathbf{x}') \,, \tag{1.60}$$

(where $\hat{\psi}^\dagger(\mathbf{x}) = \sum_k e^{-i\mathbf{k}\cdot\mathbf{x}} c^\dagger_{\mathbf{k},e}$ is the fermionic wave function and $\hat{\phi}(\mathbf{x}) = \sum_k e^{i\mathbf{k}\cdot\mathbf{x}} c_{\mathbf{k},C}$ the photonic one) we see that the effective photon-matter interaction is now vanishing in the real space and the UV divergence is healed. This cut-off will depend on the particular geometry and dimension of the cavity considered. Usually it is smaller or roughly equal to the inverse of lattice spacing. The Variational molecular ground state considered in our study is

$$|\Psi(\mathbf{Q})\rangle = \frac{1}{\sqrt{\Omega}} \sum_{\mathbf{k}} \varphi_{\mathbf{k},\mathbf{Q}} c^\dagger_{\mathbf{Q}-\mathbf{k},h} c^\dagger_{\mathbf{k},e} |0\rangle_1 \otimes |0\rangle_2 \otimes |0\rangle_{ph} + \alpha_{\mathbf{Q},C} c^\dagger_{\mathbf{Q},C} |0\rangle_e \otimes |0\rangle_h \otimes |0\rangle_{ph} \,, \tag{1.61}$$

With the normalization condition $1 = \langle\Psi|\Psi(\mathbf{Q})\rangle = \frac{1}{\Omega}\sum_{\mathbf{k}} |\varphi_{\mathbf{k},\mathbf{Q}}|^2 + |\alpha_{\mathbf{Q},C}|^2$.
Minimizing the expectation value $\langle\Psi(\mathbf{Q})|\,(\hat{H}-E)\,|\Psi(\mathbf{Q})\rangle$ with respect to the complex amplitudes

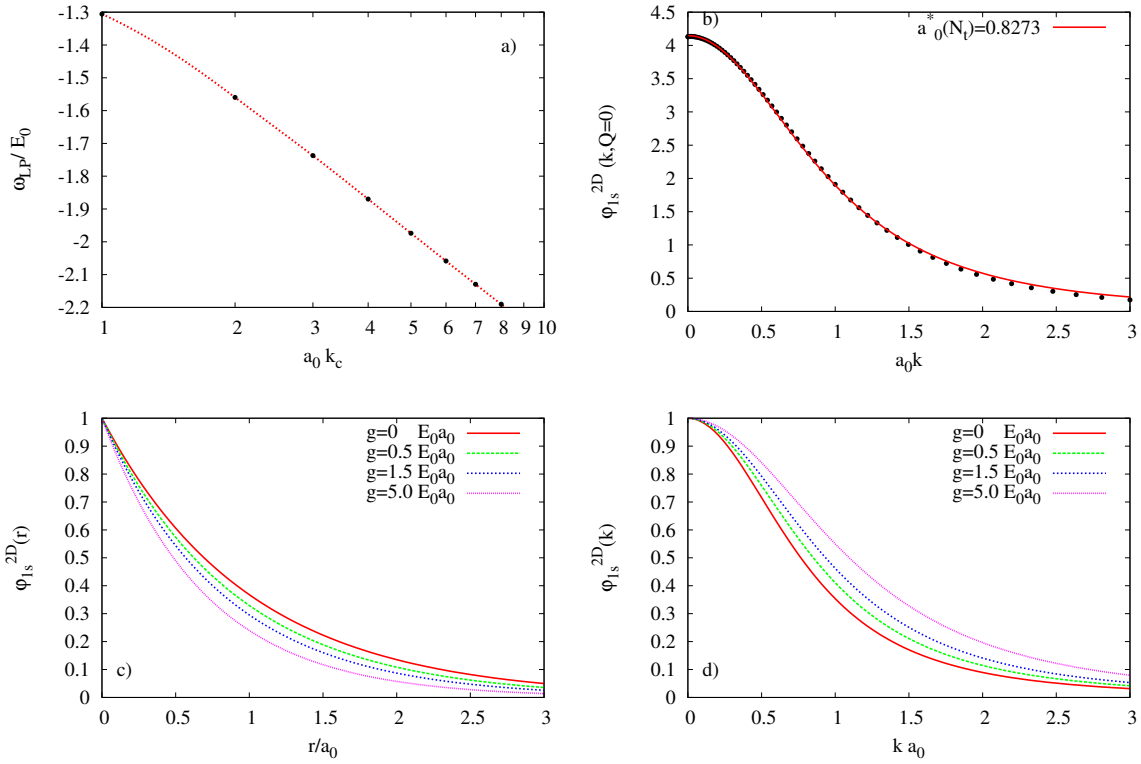

Figure 1.8: a) Logarithmic divergence of the lower polariton energy with respect to the momentum cutoff, at $g = 1.5E_0a_0$. b) Excitonic wavefunction at $g = 1.5E_0a_0$, $k_c = 2/a_0$ evaluated with the Gauss-Legendre method, using a fixed number of point, $N_t = 66$, fitted by Eq. (1.64). c, d) Excitonic wavefunction profiles at different value of g in real and momentum space.

$\varphi_{\mathbf{k},\mathbf{Q}}$ and $\alpha_{\mathbf{Q},C}$, we obtain two coupled eigenvalue equations for the polariton energy E:

$$E\varphi_{\mathbf{k},\mathbf{Q}} = (\epsilon_{\mathbf{Q}-\mathbf{k},h} + \epsilon_{\mathbf{k},e})\,\varphi_{\mathbf{k},\mathbf{Q}} - \frac{1}{\Omega}\sum_{\mathbf{k}'}\frac{2\pi e^2}{\epsilon(\mathbf{k}-\mathbf{k}')}\varphi_{\mathbf{k}',\mathbf{Q}} + ge^{-(k/k_c)^2}\alpha_{\mathbf{Q},C} \tag{1.62}$$

$$E\alpha_{\mathbf{Q},C} = \omega_{\mathbf{Q},C}\alpha_{\mathbf{Q}} + \frac{g}{\Omega}\sum_{\mathbf{k}} e^{-(k/k_c)^2}\varphi_{\mathbf{k},\mathbf{Q}}\,. \tag{1.63}$$

As already done for the electron-hole problem, we solve this Schrödinger coupled equations with the Gauss-Legendre method, obtaining a numerically solvable matrix equation (in detail in Appendix A). To start with, we consider the case of a zero exciton-photon detuning, $\delta = 0$. The first interesting things to stress is the important role of the momentum cutoff. In Fig. 1.8(a) we show the logarithmic divergence of the lower polariton energy with respect to the momentum cutoff, even at $\delta = 0$. So, considering a renormalized contact interaction in the electron-hole-photon problem, one avoids problem linked with the logarithmic divergence of polariton energy. The other open question is about the effect of photons on the exciton wavefunction. The numerically extracted 2D wavefunction $\varphi_{\mathbf{k}}/\sqrt{1-|\alpha_0|^2}$ can be fitted extremely well to the following expressions in momentum and real space:

$$\varphi^{2D}_{1s}(\mathbf{k}) = \frac{2\sqrt{2\pi}a^*_0(N_t)}{(1+(a^*_0(N_t)\mathbf{k})^2)^{3/2}} \qquad \varphi^{2D}_{1s}(\mathbf{r}) = \sqrt{\frac{2}{\pi}}\frac{1}{a^*_0(N_t)}e^{-\mathbf{r}/a^*_0(N_t)}\,. \tag{1.64}$$

Thus, the coupling to light preserves the same form that the excitonic wavefunction had without the coupling to light but changes the effective spreading $\lambda(N_t) = a^*_0(N_t)/a_0$, where

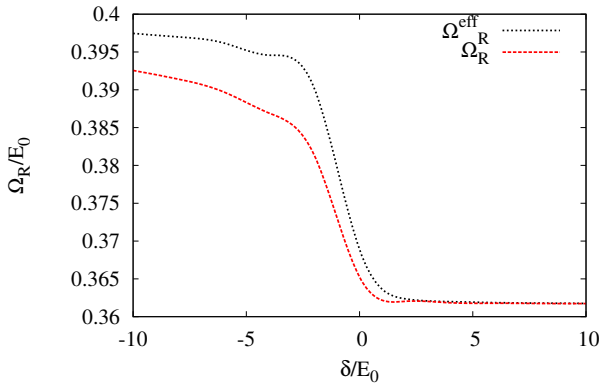

Figure 1.9: Comparison between exact Rabi splitting, obtained with (1.67), and the effective one, (1.65), at $\tilde{k}_c = 2/a_0$ and $g = 0.5E_0a_0$.

$a_0^*(N_t) = a_0^{\text{fitted}}(N_t)$ is extracted by fitting the numerical result $\varphi_{\mathbf{kQ}=\mathbf{0}}/\sqrt{1-|\alpha_{\mathbf{0}}|^2}$ with the above expression, at a fixed number N_t of points chosen for the Gauss-Legendre method (see Fig. 1.8 (b)). Interestingly, we find that $\lambda(N_t) < 1$ for any finite value of the coupling to light g and thus the excitonic wavefunction is more spread out in momentum space and more localized in real space than for $g = 0$ (see Fig. 1.8(c, d)). Further, λ decreases as a function of g, and for $g \gg 1$ it has a logarithmic dependency (see Fig. 1.7(b)). At the same time, we do find that, at the fixed detuning $\delta = 0$, the photon fraction of the polaritonic state $|\alpha_{\mathbf{0}}|^2$ is not 1/2 as naively expected for a two-oscillator model, rather numerically we find that $|\alpha_{\mathbf{0}}|^2 > 0.5$ for any value of $k_c a_0 > 1$ and finite $g \neq 0$ (see Fig 1.7(c)). To highlight the relationship between the photon fraction and the factor λ, in Fig. 1.7(c) we plot them as a function of the detuning δ. For $\delta \gg 0$, the photon fraction is low, as expected, and $\lambda \approx 1$. In the other limit, for $\delta \ll 0$, the high presence of photons implies a smaller radius. It is important to highlight that, when the photon influence is strong, the exciton radius is of the same order of magnitude as the lattice constant $\approx 1/k_c$ (see Fig. 1.7(d)). This shorter radius, that clearly implies a stronger binding energy, will be important in the study of the polaritons problem, presented in the next chapters.

1.5.2 Rabi splitting

From the results above we have seen that, as a consequence of a strong coupling to light, the effective exciton spreading is smaller than in absence of photons, i.e., $a_0^* < a_0$, and the effective photon fraction is $|\alpha_{\mathbf{0}}|^2 > 0.5$ even at zero detuning. Thus we expect that the coupled oscillator model will not give an accurate approximation of the real electron+hole+photon problem, at negative detunings, and thus we have to re-define an effective Rabi splitting and, for fixed values of g and k_c, see how it varies as a function of δ. As shown by MacDonald *et al.* [21], the effective Rabi splitting is related to the coupling to light g, the cut-off k_c and the excitonic wavefunction by:

$$\Omega_R^{\text{eff}} = 2g \int \frac{d\mathbf{k}}{(2\pi)^2} e^{-(k/k_c)^2} \frac{\varphi_{\mathbf{kQ}=\mathbf{0}}}{\sqrt{1-|\alpha_{\mathbf{0},C}|^2}} \,. \tag{1.65}$$

We evaluated it numerically with the Gauss-Legendre method, for different fixed values of N_t and then sending $N_t \to \infty$. We compare this expression of an effective Rabi splitting with those obtained by comparing the lowest energy E evaluated numerically with the expression of the lower polariton:

$$\omega_{\mathbf{q},LP} = \frac{\omega_{\mathbf{q},X} + \omega_{\mathbf{q},C}}{2} - \frac{1}{2}\sqrt{(\omega_{\mathbf{q},C} - \omega_{\mathbf{q},X})^2 + \Omega_R^2} \,. \tag{1.66}$$

evaluated at zero momentum; from this we obtain the real Rabi splitting of the problem

$$\Omega_R = \sqrt{(2\omega_{0,X} + \delta - 2\omega_{0,LP})^2 - \delta^2}\,, \tag{1.67}$$

where $\omega_{\mathrm{LP}\mathbf{0}} = E$ is the eigenvalue we evaluate numerically. We compare in Fig 1.9 the exact Rabi splitting Ω_R evaluated according to (1.67) and the effective Rabi splitting $\Omega_R^{\mathrm{eff}}(N_t)$ evaluated numerically according to (1.65) as a function of detuning and for fixed values of N_t, g and k_c. We can appreciate that, as expected, the two definitions agree when $\delta \gg E_0$, and instead, at smaller detuning, the Rabi coupling is stronger, due to the reduced matter-excitation size in presence of photons.

Chapter 2

Doped structures and gating

Over the past years, different studies on excitonic systems were carried on, with particular attention on the search for an excitonic Bose Einstein condensate. Even though there are not definitive proofs of excitonic condensation so far, notable advances in this direction have been made for indirect excitons in coupled quantum wells. Indirect excitons are coupled electron-hole pairs, where electrons and holes are separated in different wells. Spatial separation prevents recombination and the reduced overlap of the carrier wave functions enhances the exciton lifetime up to hundreds of ns. In this chapter we illustrate the different experimental realizations of electron-hole bilayers. We mainly focus on GaAs quantum well structures, describing the different configurations as well as the techniques that nowdays allow to independently control the populations of electrons and holes in the two layers. However we will briefly introduce new type of semiconductor structures, such as graphene and transition metal dichalcogenide (TMDC) structures, which are both strictly 2D systems offering new opportunities in this field.

2.1 GaAs heterostructures

Gallium arsenide (GaAs) is a compound of the elements gallium and arsenic. The use of GaAs compounds is multiple. For example complex layered structures of gallium arsenide in combination with aluminum arsenide (AlAs) or the alloy $Al_xGa_{1-x}As$ are used to implement heterostructure devices, where a layer of low band gap material (GaAs) is sandwiched between two high band gap layers (i.e. AlAs). If the middle layer is made thin enough, a quantum well can be fabricated due to the difference in the band structures of the two different semiconductors. The advantage of a this devices is in the greater quantity of electron-hole pairs in the active region, where free electrons and holes exist simultaneously confined to the thin middle layer.

2.2 GaAs bilayers

An important application of the GaAs materials is in the creation of separate quantum well, where electrons and holes can be confined separately. This structures are called e-h bilayers. At low densities of carriers, one electron in one layer can form a bound state with one hole in the other layer, leading to the formation of what is called indirect exciton. As we will see in the following sections, there are different ways to achieving this regime. Further, when the distance between the layers is comparable to the average separation between particles in the same layer, the combination of interlayer and intralayer Coulomb interaction is predicted to led to new phenomena with no counterpart in the single-layer case , such as a supersolid Wigner crystal in one or both layers [23, 24], as well as a condensate of indirect excitons displaying

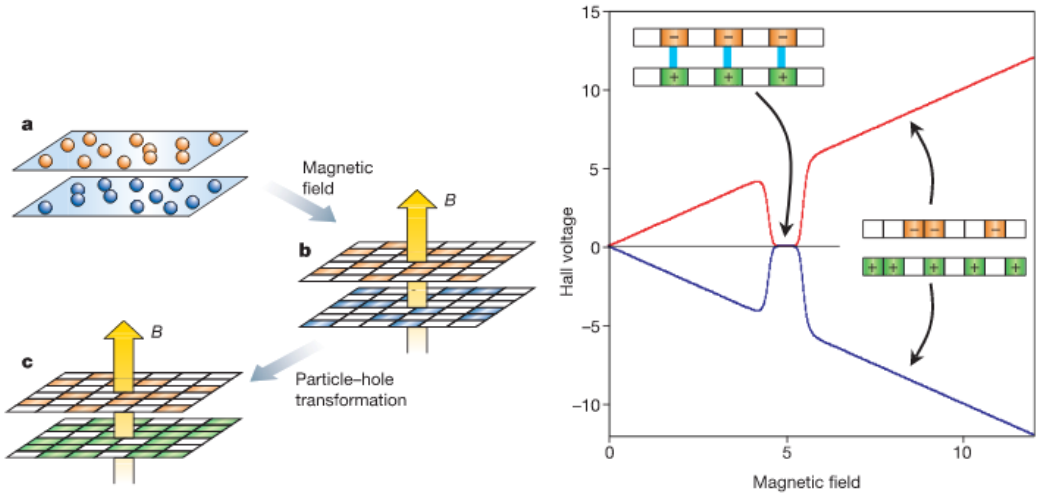

Figure 2.1: Left panel: schematic representation of two parallel layers filled with a 2D electron gas (2DEG) (a). When the magnetic field B is applied orthogonally to the layers, the kinetic energy is quantized into Landau energy levels (b). This state are highly degenerate, but if the field is strong enough, all electrons reside in the lowest Landau level, and only occupy a fraction of the other levels. A particle-hole transformation applied in the lower layer replaces the unoccupied states with the concept of electron-holes (c). An electron-electron bilayer system in a strong magnetic field is equivalent to an electron-hole bilayer. Right panel: schematic reproduction of the expected Hall voltage measurement. The red and blue traces represent the Hall voltage in the two layers as a function of the magnetic field, with an opposite sign because the current is opposite directions. But, when the magnetic field is such that the number of particles is nearly equal in the two layers ($\nu = 1/2$), the exciton condensation can occur and the current in the two layers is carried by uniform flow of excitons in one direction. Due to the charge neutrality no Lorentz force is present, and so the Hall voltage is expected to vanish. Figures taken by Ref. [26].

superfluid properties [25]. We describe in the following three sections the three experimental realization of electron-hole bilayers.

2.2.1 Double quantum well in a strong magnetic field

One way to realize an effective e-h bilayers in GaAs structures is by considering the case where GaAs quantum wells are embedded in a strong perpendicular magnetic field B. Due to the Lorentz force, the electron trajectories are bended into circles – cyclotron orbits. In a 2D system these orbits are quantized, and the set of orbits with same energy are called Landau levels. These levels are usually highly degenerate. However with an high magnetic field, it is possible to enter a regime where the total number of electrons or holes is less then the number of states contained in the lowest Landau level. The filling factor ν represents the ratio between the number of particles and the number of available states.

To easily figure out the creation of exciton condensation in bilayers filled with a 2D electron gas (2DEG), is convenient to make particle-hole transformation in one of the two layers. For instance, if one layer, containing electrons, is characterized by a filling factor ν, in the other one we can keep track of only the empty states, changing the sign of the carrier charge, the sign of the kinetic energy of the valence-band holes, and with a filling factor of $1-\nu$ (see Fig. 2.1). This transformation is equivalent to the more familiar mapping of unoccupied valence-band electron states in holes. In this way, we are now considering a electron-hole bilayers, with attraction

interaction between particles.

An excitonic BEC occurs when holes bind together with electrons, and this is most likely possible when the populations of electrons and holes are nearly the same. Experimentally it was proved that in the case $\nu = 1/2$ in each layer, the system exhibit a quantized Hall effect. In particular the Hall resistance measured when a current flows in one layer is quantized and equal to h/e^2 [27]. This effects depends on a complex combination of Landau quantization and Coulomb interaction. One way to detect the presence of a bound state is through an Hall voltage measurement. In the right panel of Fig. 2.1 a schematic representation is shown. In the two layers a current, with different sign, is flowing. When in the two layers is not present an equal filling factor, or when the distance is too high, no condensation is seen. But when the system has the right conditions, one expects a vanishing Hall-voltage, due to the creation of neutral charged pairs. This prediction was tested in different publications, with strong evidences for condensation into a macroscopic quantum state at very low temperatures [28, 26] .

2.2.2 Zero magnetic field: induced electron-hole bilayer

Even though there has been evidence of exciton condensation in electron-electron bilayer structures in presence of strong magnetic field, for the zero magnetic field case, exciton condensation and superfluidity still remain elusive. Another possibility to achieve exciton condensation comes from considering actual electron and hole bilayers, where electrons and holes are confined in two different parallel quantum wells. By confining electrons and holes in separate layers, tunneling through the barrier is suppressed when the thickness is large enough and the tunneling suppression leads to increased lifetimes of the so called indirect excitons, formed by interlayer pairs, with a consequent increasing in the possibility to observe collective phenomena in almost equilibrium conditions. One way to create a stable electron-hole bilayer is by electrical generation. Through two separate gate, is possible to control independently the electron-hole densities, applying a gate voltage. The steps to obtain this situation are explained here. In an intrinsic semiconductor (with no doping), the Fermi level is lying exactly in the middle of the energy band gap – we are considering the case of low temperatures. In this situation, electrons (holes) do not have enough energy to occupy the conduction band (valence band) (see Fig. 2.2a)). When a voltage V_G^{top} is applied on the top gate (see Fig. 2.2 b)) the Fermi level is shifted towards the conduction band. The presence of an electric field also modified the valence and conduction band dependency on the direction perpendicular to the wells. When the potential exceeds a threshold value, the Fermi level crosses the conduction energy band of the nearest quantum well, and the electrons start to populate that well. In the same way, applying a voltage with a reversed sign on the other gate V_G^{back} (see Fig. 2.2 c)) is possible to let the Fermi level overcome the valence energy band, and so the holes start to populate it. The final step to reach a population of electrons in the first well and of holes in the other one, is obtained by introducing an external bias, V_{e-h}, to keep the two layers at different electrochemical potential. In this way the Fermi level goes from the valence band of one layer to the conduction band of the other (see Fig. 2.2 d)).

Another method employed to obtain stable e-h bilayers is by introducing doped materials, where instead of applying a voltage, the introduction of impurities changes the Fermi level, resulting in the same final stable situation, where electrons and holes result confined in two separate quantum wells.

Both approaches allow to study transport phenomena in electron-hole bilayers while keeping control of population densities in both layers. In general, it was seen that electrical transport measurements in this structures give information about the state of the system. A widely used technique is the one of the Coulomb drag. Here long-range Coulomb interaction between charge carriers in two closely spaced but electrically isolated conductors induces a voltage in one of

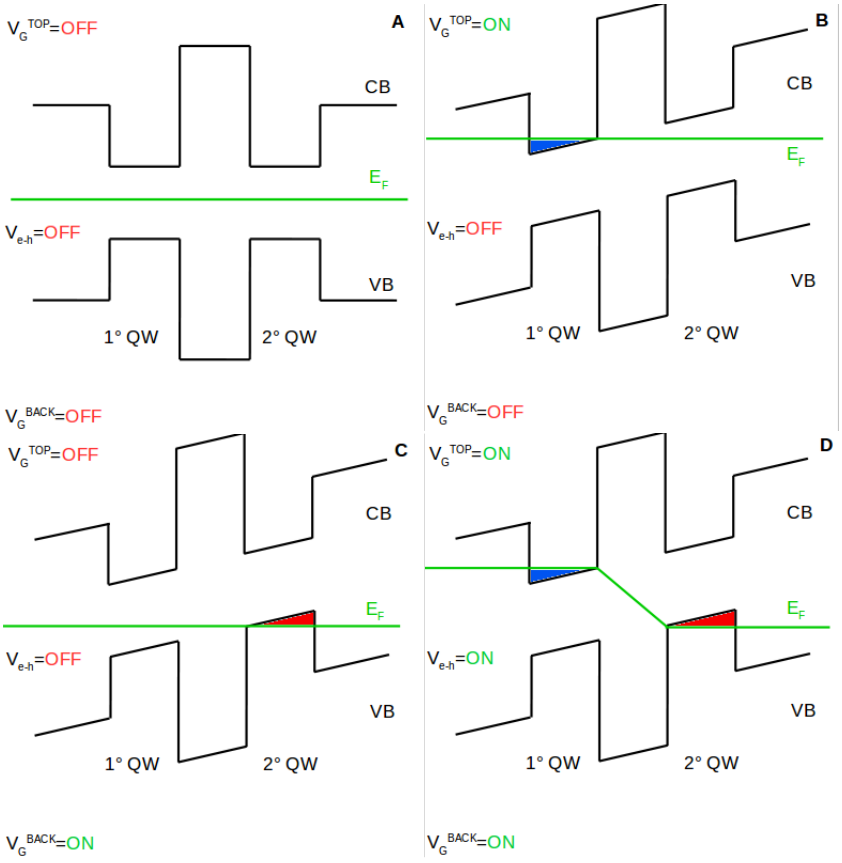

Figure 2.2: a) In an intrinsic semiconductor, the Fermi level is lying exactly in the middle of the energy band gap for low temperatures. b) When a voltage V_G^{top} is applied on the top gate, the Fermi level is shifted towards the conduction band. The presence of an electric field also modified the valence and conduction band dependency respect the direction perpendicular to the wells. So the electrons start to populate it. c) Applying a voltage with a reversed sign on the back gate is possible to let the Fermi level overcome the valence band energy, and so the holes start to populate it. d) Introducing an external bias, V_{e-h}, the two layers are kept at different electrochemical potential. In this way the Fermi level goes from the valence band of one layer to the conduction band of the other.

the conductors when an electrical current is passed through the other (see Fig. 2.3). The drag resistivity, defined as

$$R_{drag} = V_{drag}/I_{drive} \ , \tag{2.1}$$

represents a direct measurement of the interlayer scattering. This means that, for a weakly coupled Fermi liquid, the drag resistance decreases with the temperature, due to the vanishing phase space for scattering. However it was reported in Ref. [30, 31] an anomalous increase of the drag at low temperatures, suggesting the emergence of a non-Fermi liquid phase. Despite different theoretical works predicted unambiguously this anomaly to occur at the onset of an excitonic condensation [32, 33], some doubts and unanswered questions still exist about the nature of this effect.

2.2.3 Optically generated indirect excitons

In absence of doping and gate contacting, indirect excitons can be generated optically. In this set up, there are several experiments on indirect excitons in GaAs structures with and without

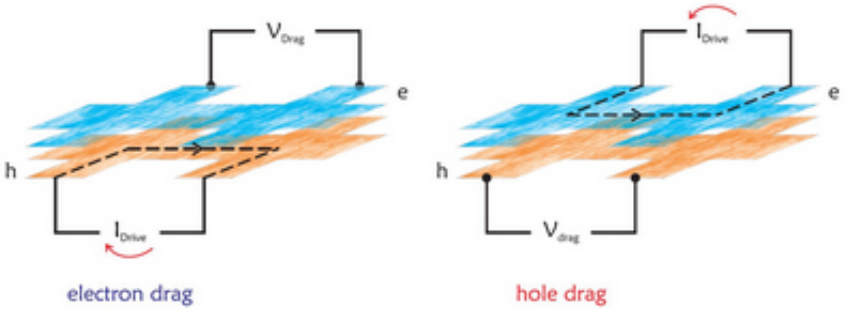

Figure 2.3: Schematic representation of a Coulomb drag experiment. A current flows through one layer: the carriers interact, exchanging momentum and energy, with the particles of the other layer. As a result is an open-loop voltage forms across the second layer. Picture taken from Ref. [29]

a cavity confining the photons. How indirect excitons can be generated via an optical pump is schematically explained in Fig. 2.4. We have seen in the previous section that applying a gate voltage across the quantum wells, and thus generating an electric field perpendicular to the growth direction, results in a tilting of the conduction and valence bands. This creates different energy gaps weather we consider valence and conduction bands in the same or in different wells. When an optical pump is injected in the system, one generates an equal population of electron and holes in each well, thus creating direct excitons (DXs) as well as indirect excitons (IXs). However direct excitons, which belongs to the same well, do recombine quickly. Because of the band tilting, only electrons in the lowest energy conduction band and holes in the higher energy valence band are left. Because they belong to different wells, only indirect excitons are left behind after direct ones have recombined. If now one confines this quantum system in a microcavity (see Fig. 2.4 c)), one can describe the system via a three-coupled oscillator model: direct excitons are optically coupled to cavity photons via the Rabi coupling Omega; at the same time, direct and indirect excitons are coupled via tunneling J. A simple Hamiltonian model coupling these states $|DX\rangle, |IX\rangle, |C\rangle$ is

$$\hat{H} = \hbar \begin{pmatrix} \omega_{IX} & -J/2 & 0 \\ -J/2 & \omega_{DX} & -\Omega/2 \\ 0 & -\Omega/2 & \omega_C \end{pmatrix} , \tag{2.2}$$

where $\omega_{IX,DX,C}$ are respectively the energies of indirect exciton, direct exciton and cavity photon. Diagonalization of $\hat{H}$ yields to three different modes

$$|MP\rangle = \alpha \left[\Omega|IX\rangle - J|C\rangle\right] \tag{2.3}$$

$$\begin{vmatrix} UP \\ LP \end{vmatrix} = \beta \left[J|IX\rangle + \Omega|C\rangle + (\delta \pm \sqrt{\Omega^2 + J^2 + \delta^2})|DX\rangle\right] , \tag{2.4}$$

with δ the cavity detuning. The resulting quasiparticles which are a superposition of a DX, and IX and a cavity photon are similar to the exciton polaritons formed out of DXs only, with the difference that now posses a large dipole moment inherited from the IX component [37]. In these structures is not possible to control independently the electron and hole density. Nevertheless, it is possible to tune the dipolariton interaction strength by increasing the density of indirect excitons, i.e., by optically pumping stronger the system. [35, 38].

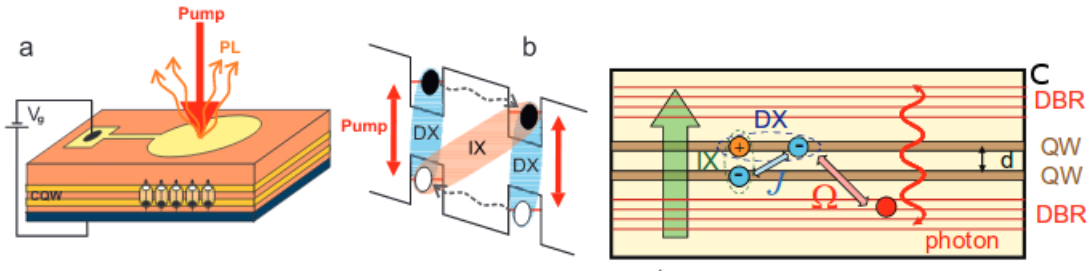

Figure 2.4: a), b) Schematic representation of the optical creation of an electron-hole bilayers. On the quantum wells a perpendicular electrical filed is applied. This field changes the geometry of the valence and conduction band. When an optical pump is injected in the system, direct excitons (DXs) and indirect excitons (IXs) are created. Figures taken from Ref. [34]. c) Schematic representation of bilayers confinement. The application of the electric field – green arrow – allows the creation of indirect excitons (IX) coupled with direct excitons (DX) via the tunneling rate J. The DBR mirrors confine the cavity photons, that result coupled with the direct excitons via Rabi frequency Ω. Picture taken from Ref. [35]

2.3 2D materials: graphene and TMDC monolayers

Novel technical advances in exfoliation, deposition and irradiation techniques, has led to the ability to produce 2D atomic layers materials. The most well-known is graphene, a single layer of carbon atoms in a honeycomb lattice. Thinking about bilayers structures, graphene offers a stronger interlayer interaction, thanks to a small dielectric constant and the possibility to reduce the distance between layers of an order of magnitude smaller than the one achieved in GaAs structures. This favours for example Coulomb drag measurements not only when the distance d between layer is greater or nearly equal to the characteristic distance L between carriers, such as in GaAs, but also in the limit of $d/L \ll 1$, exploring the Fermi liquid regime – E_F larger than k_BT – as well as the less explored Boltzmann regime – $E_F < k_BT$ [39].

With graphene, also other 2D materials are actually used in optical devices. An example are the layered transition metal dichalcogenides (TMDC), thin direct band gap semiconductors of the type MX_2, with M a transition metal atom (Mo, W, etc.) and X a chalcogen atom (S, Se, or Te). One layer of M atoms is sandwiched between two layers of X atoms. The direct band gap allows the optical excitation of excitonic state, and the reduced dielectric screening joined by the quantum size effect present in these ultra-thin material make the binding energy of resulting excitons much stronger than those in traditional semiconductors (like GaAs). This is a key prerequisite for an ideal material system in polariton research, and jointly with the electrical injection, highly desirable for any practical optoelectronic device into atomic monolayers, that is proven more feasible in TMDC respect in quasi 2D materials, and an absorption of light up to 20% per monolayer, nowdays exciton-polaritons in cavity structures with atomic TMDC monolayers are preferred to the conventional quasi-two-dimensional semiconductors like GaAs.

One of the first steps in the investigation of new physics involving TMDC structures was made by Sidler, Imamoglu et *et al.* [40], where they use gate- tunable monolayer $MoSe_2$ embedded in a microcavity. In their research they stress out the important of this materials not only for the physics of exciton-polaritons, but also other kind of optical response of embadded semiconductor, like trions and polarons. Their findings represent one of the first step in the investigation of new physics involving degenerate Bose-Fermi mixtures.

Chapter 3

Theory of exciton and polaritons condensation

In Chapter 1, we have discussed the formation of an electron hole bound pair, i.e., an exciton, in a direct gap semiconductor. One expects that, at low densities, excitons behave as bosonic particles and thus, at sufficiently low temperatures, undergo Bose-Einstein condensation. By increasing the exciton density, however, their composite fermionic nature becomes relevant, the occupation of the low momentum states is blocked by the Pauli exclusion principle, and, condensation is reminiscent of the BCS theory for superconductors. Because, differently from a superconductor, pairing is between particles of opposite charge, this phase takes the name of exciton insulator. In this chapter we review the existing theory about the BEC-BCS crossover for excitonic systems. In particular, we review how to construct an appropriate wavefunction interpolating between a BEC of excitons at low densities and an exciton insulator at higher densities [41, 45, 42]. Further, we describe how the crossover changes when a 2D exciton gas in embedded in a microcavity confining the photon [43, 44, 21].

3.1 From exciton condensation to the exciton insulator

The starting point of our study is the "d exciton gas. In 2D there is no condensate at finite temperature for a non interacting gas of boson, whereas in presence of interaction the superfluid transition is a Berezinskii-Kosterlitz-Thouless and not a Bose-Einstein condensation. In our work we consider $T = 0$ where BEC can occur again. We didn't consider the effects of temperature. The Hamiltonian of the electron-hole system is

$$\hat{H} = \hat{H}_0 + \hat{H}_{int} \,, \tag{3.1}$$

where

$$\hat{H}_0 = \sum_k \left[\epsilon_{\mathbf{k},e} c^\dagger_{\mathbf{k},e} c_{\mathbf{k},e} + \epsilon_{\mathbf{k},h} c^\dagger_{\mathbf{k},h} c_{\mathbf{k},h} \right] \tag{3.2}$$

and

$$\hat{H}_{int} = \frac{1}{2} \sum_q \left[U^{ee}_{\mathbf{q}} \rho^e_{\mathbf{q}} \rho^e_{-\mathbf{q}} + U^{hh}_{\mathbf{q}} \rho^h_{\mathbf{q}} \rho^h_{-\mathbf{q}} - 2U^{eh}_{\mathbf{q}} \rho^e_{\mathbf{q}} \rho^h_{-\mathbf{q}} \right] \,, \tag{3.3}$$

The creation operators $c^\dagger_{\mathbf{k},e}$ and $c^\dagger_{\mathbf{k},h}$ are respectively for electrons and holes, and the density operators are defined as $\rho^e_{\mathbf{q}} = \sum_k c^\dagger_{\mathbf{k+q},e} c_{\mathbf{k},e}$ and $\rho^h_{\mathbf{q}} = \sum_k c^\dagger_{\mathbf{k+q},h} c_{\mathbf{k},h}$. $U_{\mathbf{q}}$ is the Coulomb interaction, and for an homogeneous 2D system $U^{ee}_{\mathbf{q}} = U^{hh}_{\mathbf{q}} = U^{eh}_{\mathbf{q}} = 2\pi/\epsilon\Omega q$, with Ω being the system volume. If one instead is considering the confinement of electrons and holes in two

different layers, $U^{ee}_{\mathbf{q}} = U^{hh}_{\mathbf{q}} = 2\pi/\epsilon\Omega q$, $U^{eh}_{\mathbf{q}} = 2\pi e^{-qd}/\epsilon\Omega q$, where d is the inter-layer distance. Finally we remind that for parabolic bands $\epsilon_{\mathbf{k},e} = \hbar^2 k^2/2m_e$ and $\epsilon_{\mathbf{k},h} = E_g + \hbar^2 k^2/2m_h$. At extremely low electron and hole densities, one recover the two-body problem already discussed in Chapter 1. We have seen that the exciton Bohr radius a_0^{2D} (see Eq. (1.21)) and Rydberg energy E_0^{2D} (see Eq. (1.20)) represent the natural units of the problem, and it is convenient to measure the densities of the system as a function of that radius, by defining the dimensionless parameter r_s

$$\frac{1}{n} = \pi (r_s a_0^{2D})^2 \ , \tag{3.4}$$

where $n = n_e = n_h = \frac{1}{\Omega}\sum_k c^\dagger_{\mathbf{k},e} c_{\mathbf{k},e}$. The Hamiltonian discussed is a simply model to describe dynamics regarding possible phase transitions, with only few relevant parameters, such as the density, the mass ratio between the two Fermi species and, for the 2D bilayer, the distance.

What we want to do now is to write down a wavefunction that, in the low density limit, could describe a BEC of bound excitons. The exciton operator is just a wavepacket of one electron hole pair, i.e. an exciton, at finite center of mass momentum $\mathbf{Q}$

$$\Phi_{\mathbf{Q}} = \sum_k \varphi_{\mathbf{k},\mathbf{Q}} c_{\mathbf{k},e} c_{\mathbf{Q}-\mathbf{k},h} \ , \tag{3.5}$$

composed of electron and hole annihilation operators $c_{\mathbf{k},e}$ and $c_{\mathbf{Q}+\mathbf{k},h}$. Eq. (3.5) describes an exciton with center of mass momentum $\mathbf{Q}$, and $\varphi_{\mathbf{k},\mathbf{Q}}$ is the Fourier transform of the internal exciton wavefunction. A possible state with N condensed excitons has a wave function

$$|\Psi_0^N\rangle = \Phi_0|0\rangle \tag{3.6}$$

We expect that the occupancy number of kth fermionic state is $n_{\mathbf{k}} = \langle\Psi_0^N|c^\dagger_{\mathbf{k},e}c_{\mathbf{k},e}|\Psi_0^N\rangle = N|\varphi_{\mathbf{k},0}|^2$, and so for $r_s \propto \frac{1}{Na_0^2} \gg 1$, and so $Na_0^2 \ll 1$, one obtains $n_{\mathbf{k}} \ll 1$. Furthermore it is possible to show that

$$\left[\Phi_{\mathbf{Q}}, \Phi^\dagger_{\mathbf{Q}'}\right] = \delta_{\mathbf{Q},\mathbf{Q}'} - \varphi_{\mathbf{k},\mathbf{Q}}\varphi^\dagger_{\mathbf{k},\mathbf{Q}'} c^\dagger_{\mathbf{Q}'+\mathbf{k},h} c_{\mathbf{Q}+\mathbf{k},h} - \varphi_{\mathbf{k},\mathbf{Q}}\varphi^\dagger_{\mathbf{k},\mathbf{Q},\mathbf{Q}'} c^\dagger_{\mathbf{Q}+\mathbf{k}-\mathbf{Q}',e} c_{\mathbf{k},e} \approx \delta_{\mathbf{Q},\mathbf{Q}'} - \mathcal{O}(Na_0^2) \tag{3.7}$$

We can conclude that at low densities it is possible to neglect the exclusion principle, and the exciton behave as a boson.

When the interparticle spacing becomes smaller than the exciton Bohr radius, $a_0^{2D} = \frac{2\pi\epsilon_r\epsilon_0}{\mu e^2}$, then excitons cannot be considered as structurless bosons, rather their fermionic nature start to dominate. In particular, the occupation of the low momentum states becomes blocked by Pauli exclusion principle. Now pairing can only occur for those states close to the Fermi surface in a form similar to Cooper pairing in conventional superconductors. The resulting BCS-like state of condensed electron-hole Cooper pairs is usually called exciton insulator. This is because electrons and holes form neutral pairs and thus this condensed phase corresponds to a insulating phase rather than a conducting one.

The interpolating wavefunction between a BEC condensate of tightly bound excitons and a higher density exciton insulator state was build for the first time by Keldysh and Kopaev [45]. In particular, in the low density limit, excitons can be described as tightly bound bosons and we can write a BCE-like coherent ground state

$$|\Psi_0^{GS}\rangle = e^{\lambda\Phi_0^\dagger}|0\rangle = \prod_k e^{\lambda\varphi_{\mathbf{k},0}c^\dagger_{\mathbf{k},e}c^\dagger_{-\mathbf{k},h}}|0\rangle \ . \tag{3.8}$$

The number of particles in the condensate is fixed by the modulus of λ

$$\langle\Psi_0^{GS}|\Phi_0^\dagger\Phi_0|\Psi_0^{GS}\rangle = |\lambda|^2 \tag{3.9}$$

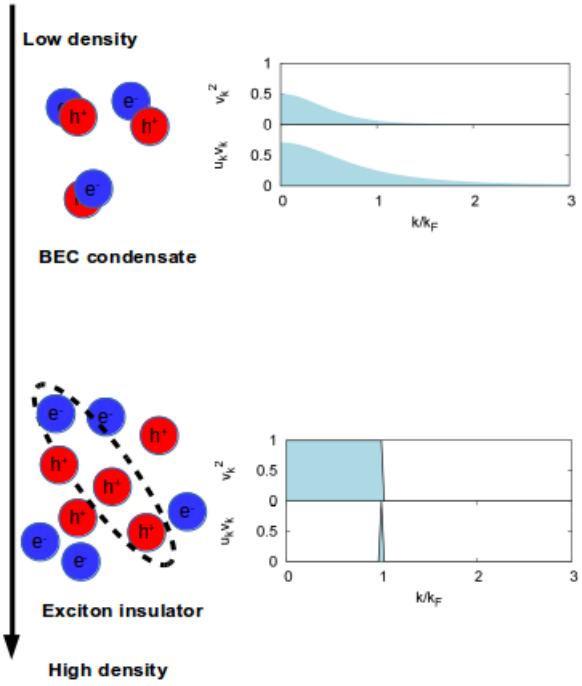

Figure 3.1: Increasing the electron-hole density, the system changes from a Bose-Einstein condensate to an excitonic insulator. In the low density limit the e-h pairs are tightly bound, with the occupancy $v_{\mathbf{k}}^2 \propto 1/(1+k^2)^3$ and the condensate wavefunction $u_{\mathbf{k}}v_{\mathbf{k}} \approx v_{\mathbf{k}} \propto 1/(1+k^2)^{3/2}$. In the high density limit the e-h pairs are dilute and weakly bounded, with an occupancy that approach a step function up to a Fermi momentum k_F, and a condensate wavefunction that is peaked at k_F.

Expanding the exponential and remembering that electrons and holes are fermions ($\left(c^\dagger_{\mathbf{k},e}c^\dagger_{-\mathbf{k},h}\right)^n = 0$ for each $n > 1$), one can rewrite the coherent state in an equivalent form as

$$|\Psi_0^{GS}\rangle = \prod_k [1 + \lambda\varphi_{\mathbf{k},0}c^\dagger_{\mathbf{k},e}c^\dagger_{-\mathbf{k},h}]|0\rangle \ , \tag{3.10}$$

After the normalization, this equation reads as

$$|\Psi_0^{GS}\rangle = \prod_k [u_{\mathbf{k}} + v_{\mathbf{k}}c^\dagger_{\mathbf{k},e}c^\dagger_{-\mathbf{k},h}]|0\rangle \ , \tag{3.11}$$

where

$$u_{\mathbf{k}} = \frac{1}{\sqrt{1+|\lambda\varphi_{\mathbf{k},0}|^2}} \tag{3.12}$$

$$v_{\mathbf{k}} = \frac{\lambda\varphi_{\mathbf{k},0}}{\sqrt{1+|\lambda\varphi_{\mathbf{k},0}|^2}} \ , \tag{3.13}$$

that is the typical BCS wavefunction, describing a Bose condensation of dilute excitons (see Fig. 3.1). The interesting parameters are now the occupancy $|v_{\mathbf{k}}|^2$ and the condensate wavefunction $u_{\mathbf{k}}v_{\mathbf{k}}$. In Fig. 3.1 they are sketched as a function of k, both in the high and low density limit. In the low density regime $u_{\mathbf{k}} \approx 1$ and $v_{\mathbf{k}} \approx \lambda\varphi_{\mathbf{k},0} \propto \lambda/(1+k^2)^{3/2}$, and so the occupancy is not saturated and spreads over k – so the BEC approximation is reliable – as well as the condensate

fraction. Instead, in high density limit the saturation is reached – $|v_{\mathbf{k}}|^2$ is a step function with respect to k_F – and $u_{\mathbf{k}}v_{\mathbf{k}}$ is peaked in $|\mathbf{k}| = k_F$. Because the same wavefunction (3.10) describes both the low and high density limit at T=0, we can use it to describe the intermediate density regime, revealing a crossover between the BEC and the BCS limits. We can conclude that this is a good wavefunction to describe the exciton problem. Now, introducing the chemical potential μ to fix the particle number, and minimizing the free energy – where we are fixing $N_e = N_h = N = \sum_k c^\dagger_{\mathbf{k},e} c_{\mathbf{k},e}$

$$F = \langle H \rangle - \mu \langle N \rangle \tag{3.14}$$

with respect to the variational parameter $v_{\mathbf{k}}$, one finds a set of self-consistent equations, similar to the BCS case [41]:

$$\begin{aligned}
\xi_{\mathbf{k}} &= \epsilon_{\mathbf{k}} - \mu - 2\sum_{k'} U^{ee}_{\mathbf{k}-\mathbf{k}'} n_{\mathbf{k}'} \\
&= \epsilon_{\mathbf{k}} - \mu - \sum_{k'} U^{ee}_{\mathbf{k}-\mathbf{k}'} \left(1 - \frac{\xi_{\mathbf{k}'}}{E_{\mathbf{k}'}}\right), \qquad (3.15) \\
\Delta_{\mathbf{k}} &= 2\sum_{k'} U^{eh}_{\mathbf{k}-\mathbf{k}'} \langle c^\dagger_{\mathbf{k},e} c^\dagger_{-\mathbf{k},h} \rangle \\
&= \sum_{k'} U^{eh}_{\mathbf{k}-\mathbf{k}'} \frac{\Delta_{\mathbf{k}'}}{E_{\mathbf{k}'}}, \qquad (3.16) \\
E^2_{\mathbf{k}} &= \xi^2_{\mathbf{k}} + \Delta^2_{\mathbf{k}} \qquad (3.17)
\end{aligned}$$

$\xi_{\mathbf{k}}$ is the renormalized single pair energy. $\Delta_{\mathbf{k}}$ is the gap-function and is also the order parameter of the BCS theory. $E_{\mathbf{k}}$ is the energy cost of taking one pair out from the condensate. Simple algebra yields to

$$\begin{aligned}
u_{\mathbf{k}} v_{\mathbf{k}} &= \frac{\Delta_{\mathbf{k}}}{2E_{\mathbf{k}}} \qquad (3.18) \\
|v_{\mathbf{k}}|^2 &= \frac{1 - \xi_{\mathbf{k}}/E_{\mathbf{k}}}{2} \qquad (3.19) \\
|u_{\mathbf{k}}|^2 &= \frac{1 + \xi_{\mathbf{k}}/E_{\mathbf{k}}}{2}\,, \qquad (3.20)
\end{aligned}$$

and so we linked the condensate wavefunction to the BEC-BCS crossover order parameter $\Delta_{\mathbf{k}}$.

3.2 Theory of polariton condensation

We now want to describe the condensation of electrons and holes when their density increases, in presence of a strong coupling to light confined in a microcavity. In the very low density limit, we have already introduce in Chapter 1 the electron-hole-photon problem, where the photon contribution enhances the electron-hole coupling. This leads to the formation of a new quasiparticle, namely the polariton. When the electron-hole density increases, we want to resume here how the form of the condensate changes. Recent papers have already suggested how to address this problem, such as Ref. [43, 44, 21]. We will give a short overview on these work.

The starting point is the Hamiltonian

$$\hat{H} = \hat{H}_0 + \hat{H}_{int} + \hat{H}_{ph} + \hat{H}_{e-h-ph}\,, \tag{3.21}$$

where $\hat{H}_0$ and $\hat{H}_{int}$ are the same as before and

$$\hat{H}_{ph} = \sum_q \omega_{\mathbf{q},C} c^\dagger_{\mathbf{q},C} c_{\mathbf{q},C} \tag{3.22}$$

$$\hat{H}_{e-h-ph} = g \sum_{k,q} e^{-(\frac{k}{k_c})^2} \left[c^\dagger_{\mathbf{k},e} c^\dagger_{\mathbf{q}-\mathbf{k},h} c_{\mathbf{q},C} + h.c. \right] , \tag{3.23}$$

with $c_{\mathbf{q},C}$ the annihilation operator of for the cavity photon, $\omega_{\mathbf{q},C}$ the photon energy, g the coupling strength of cavity photon and electron-hole pairs and k_c the momentum cut-off. The chemical potential μ is used to fix the density, where $N = c^\dagger_C c_C + \frac{1}{2}\sum_k [c^\dagger_{\mathbf{k},e} c_{\mathbf{k},e} + c^\dagger_{\mathbf{k},h} c_{\mathbf{k},h}]$. Minimizing $F = \langle \hat{H} \rangle - \mu \langle N \rangle$, using a BCS ground state ansatz of the form

$$|\Psi^{GS}\rangle = e^{\alpha_C c^\dagger_{0,C}} \prod_k [u_{\mathbf{k}} + v_{\mathbf{k}} c^\dagger_{\mathbf{k},e} c^\dagger_{-\mathbf{k},h}]|0\rangle , \tag{3.24}$$

where one considers the coherent state of exciton condensate and of the emitted photon. Again, minimizing the free energy, is possible to obtain the self consistent-field equations [21]

$$\xi_{\mathbf{k}} = \epsilon_{\mathbf{k}} - \mu - \sum_{k'} U^{ee}_{\mathbf{k}-\mathbf{k}'} \left(1 - \frac{\xi_{\mathbf{k}'}}{E_{\mathbf{k}'}} \right), \tag{3.25}$$

$$\Delta_{\mathbf{k}} = \sum_{k'} U^{eh}_{\mathbf{k}-\mathbf{k}'} \frac{\Delta_{\mathbf{k}'}}{E_{\mathbf{k}'}} - g e^{-(\frac{k}{k_c})^2} \alpha_C \tag{3.26}$$

$$E^2_{\mathbf{k}} = \xi^2_{\mathbf{k}} + \Delta^2_{\mathbf{k}} \tag{3.27}$$

This equations are identical to those that appear in the exciton case, apart from the contribution of $g \exp(-k^2/k_c^2)\alpha_C$ to the gap equation and the gap energy. Now the variational parameters $u_{\mathbf{k}}$ and $v_{\mathbf{k}}$ satisfy

$$\langle c^\dagger_{\mathbf{k},e} c_{\mathbf{k},e} \rangle = v^2_{\mathbf{k}} = \frac{1}{2} \left(1 - \frac{\xi_{\mathbf{k}}}{E_{\mathbf{k}}} \right) \tag{3.28}$$

$$\langle c^\dagger_{\mathbf{k},e} c_{-\mathbf{k},h} \rangle = u_{\mathbf{k}} v_{\mathbf{k}} = \frac{\Delta_{\mathbf{k}} - g e^{-(\frac{k}{k_c})^2} \alpha_C}{2E_{\mathbf{k}}} \tag{3.29}$$

In Fig. 3.2 we report the results obtained by Byrnes *et al.* [35], where the occupancy $v^2_{\mathbf{k}}$ is plotted with respect to wavevector $\mathbf{k}$. In their system the number of particles is defined as $N = c^\dagger_C c_C + \sum_k [c^\dagger_{\mathbf{k},e} c_{\mathbf{k},e} + c^\dagger_{\mathbf{k},h} c_{\mathbf{k},h}]$, and the coupling to light is renormalized differently, However these changes are likely not to cause qualitative changes. In the low density limit the momentum distribution coincides with the one expected without the coupling to light, where $v_{\mathbf{k}} \approx \frac{1}{(1+k^2)^{3/2}}$. The BEC limit is recovered. When the density is increased, for an BCS state without coupling, we expect a moment distribution that approaches a step function. However, in the coupled case Byrnes *et al.* [44] found that for high densities the moment distribution spreads out to higher momenta. One may ask what is the origin of this effect. The explanation is in the different particles statistics. Photons are bosons, hence any number of them can occupy the ground state with a constant energy $\omega_{0,C}$. Excitons are instead composite bosons. To excite more fermionic particles, electrons and holes with greater momenta must be generated. So we expect a jump in the photon number when the density is greater than a critical one, because is favorable to excite photons rather than excitons to minimize the energy. So, when α_C is big, the photon operator could be substituted by a c-number, and the Hamiltonian is reduced to

$$\hat{H} \approx g\alpha_C \sum_k \left[c^\dagger_{\mathbf{k},e} c^\dagger_{-\mathbf{k},h} + h.c. \right] + |\alpha_C|^2 \omega_{0,C} , \tag{3.30}$$

where we neglected the terms that do not contain the factor α_C. In this limit, the BCS gap equation is $\Delta_{\mathbf{k}} \approx E^{min}_{\mathbf{k}} \approx 2g \exp(-k^2/k_c^2)\alpha_C$. Thus with increasing density, also the gap

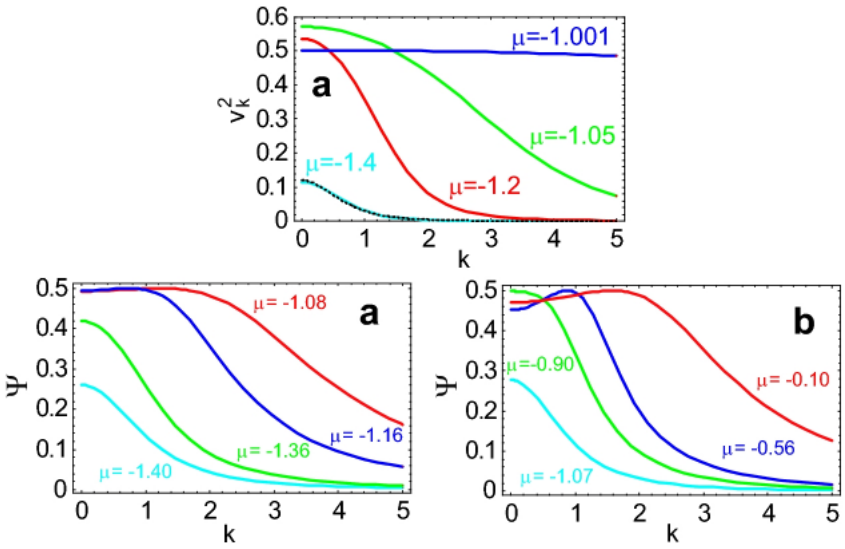

Figure 3.2: Top panel: occupancy number $|\mathbf{k}|^2$ as a function of k, in the coupling to light case. In the low-density limit – small μ – the occupancy is low, as expected in the BEC state. In the other limit – higher μ – $|\mathbf{k}|^2$ spreads out to higher momenta, precisely the opposite behavior expected for the BEC-BCS crossover. Bottom panel a: pair wavefunction $\Psi = u_{\mathbf{k}} v_{\mathbf{k}}$ as a function of k, in the coupling to light case, with a zero detuning ($\omega_{0,C} = \omega_{0,X}$). The low density limit gives what expected in the case where there is no coupling to light. When increasing the chemical potential μ the momentum peak is at a non-zero value of $\mathbf{k}$, but the pair wavefunction in these case is broader and not sharper as in the purely excitonic BCS-state. Bottom panel b: pair wavefunction $\Psi = u_{\mathbf{k}} v_{\mathbf{k}}$ as a function of k, in the polariton case, with positive detuning. In the high density limit the pair wavefunction starts to resembles the expected behavior. Figures taken from [43]

energy increases, contrarily to what expected in the standard BCS case, and, from Eq. (3.28), $|v_{\mathbf{k}}|^2 \to 1/2$.

The other interesting parameter in the BEC-BCS theory is $u_{\mathbf{k}} v_{\mathbf{k}}$. In the exciton BCS state, it is peaked near the Fermi momentum. In the case where there is coupling to cavity photons, as shown in Fig. 3.2, the non zero momentum peak is present, but instead to be sharper with increasing density, here the function becomes broader. However, increasing the cavity detuning, is possible to obtain something more "BCS-like". This is because by increasing the photon energy, the photon number is decresed and polaritons have a more excitonic-like nature.

We are now able to describe the typical and expected phase diagram. In Fig. 3.3 we show the result obtained by Kamide *et al.* [43], where they considered a GaAs based semiconductor confined in a microcavity, with a coupling strength $g = E_0 a_0$ and a momentum cut-off of $k_c a_0 = 30$ – in their paper the momentum cut-off represents simply a restriction on the momentum of the contributing electronic states to polariton formation. Clearly the phase diagram depends on the detuning. For large value of detuning the system shows four different phases: exciton BEC in the low density limit, e-h BCS when we are approaching the high density, e-h polariton BEC when the density is so high to allow the mixing between e-h pairs and the great quantity of photons generated, and the photonic BEC, in the extreme high density limit, where is energetically more convenient to excite only photons. Instead for low values of detuning, only two phases are present: the polariton BEC, where the e-h pairs and photons are mixed, with a dominant presence of exciton for high values of r_s – exciton polariton BEC, and the photonic BEC, already described. The shaded pink region represent the area in which the interaction is a Coulomb

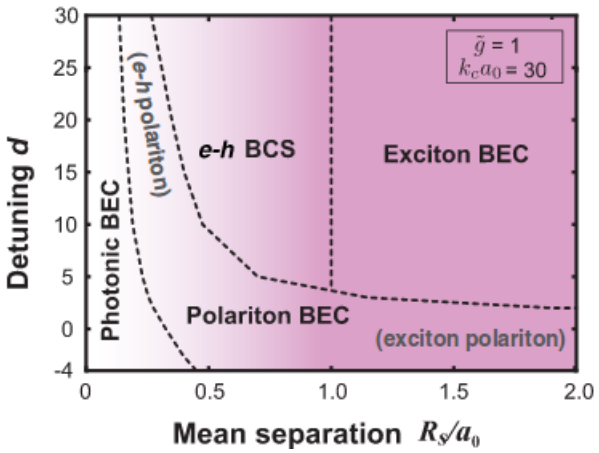

Figure 3.3: Phase diagram at zero temperature as a function of the detuning and the mean separation. $g = E_0 a_0$ and $k_c a_0 = 30$. The pink region shows the area in which the interaction is mostly a Coulomb attraction, changing into a photon-mediated attraction increasing the density. Ref. [43]

attraction, changing to a photon-mediated attraction when the density is increased.

We have analyzed the crossover between low and high density limits of exciton-polariton condensates, using a BCS-like wavefunction approach. The main differences between excitonic and polaritonic case is that, in the latter, the cavity photon influence allows in the high density limit state with a non saturated occupancy, where is still possible to identify a condensate of bosonic quasiparticles.

Chapter 4

Electron-hole bilayer with large density imbalance

Previously, we discussed experimental systems in which to explore pairing phenomena, particularly in the context of electron-hole systems. The possibility to independently control the densities of electrons and holes in the two separate quantum wells allows to explore the richer scenario of possible ground states, when the densities of the two interacting fermionic species are imbalanced, and so their pairing is frustrated. One of the most interesting possible ground states is the one in which the electron and hole generate a bound state having a finite center of mass momentum. This state is analogous to the Fulde-Ferrel-Larkin-Ovchinnikov (FFLO) phase [46, 47], a spatially modulated state predicted for the first time in a superconducting systems. The 2D bilayer represents the ideal condition for FFLO, because the reduced dimension of the system limits the normal phase, and the intra-layer Coulomb repulsion avoid macroscopic phase separation. Recent papers provide strong evidence for the existence of this exotic pairing in electron-hole bilayers, such as Varley *et al.* [48], who investigates FFLO superfluidity in imbalanced electron-hole systems via a Ginzburg-Landau model. However, we will focus our attention on the extremely imbalanced case, with only one particle in one of the quantum well layer, as already done by M.M. Parish *et al* [49]. As a first step, we are going to re-derive the results obtained in that paper, and then extend the results considering two different situation: the RPA screened Coulomb interaction and the unscreened one. The interest in considering the extreme imbalanced limit is that it allows to address the problem in a controlled manner.

4.1 Model

We start writing the basic Hamiltonian for a 2D electron-hole bilayer – $\hbar = 1$ and Ω is the system area:

$$\hat{H} = \hat{H}_0 + \hat{H}_{int} \tag{4.1}$$

$$\hat{H}_0 = \sum_{\mathbf{k},\sigma} \epsilon_{\mathbf{k},\sigma} c^\dagger_{\mathbf{k},\sigma} c_{\mathbf{k},\sigma} \tag{4.2}$$

$$\hat{H}_{int} = -\frac{1}{\Omega} \sum_{\mathbf{kk'q}} V_{\mathbf{q}} c^\dagger_{\mathbf{k},1} c^\dagger_{\mathbf{k'},2} c_{\mathbf{k'+q},2} c_{\mathbf{k-q},1} + \frac{1}{2\Omega} \sum_{\mathbf{kk'q}\sigma} U_{\mathbf{q}} c^\dagger_{\mathbf{k},\sigma} c^\dagger_{\mathbf{k'},\sigma} c_{\mathbf{k'+q},\sigma} c_{\mathbf{k-q},\sigma} \,, \tag{4.3}$$

where, $\sigma = 1, 2$ indicates the different species of fermions (either electrons or holes) and, in case of bilayers, also indicates the different 2D layers (Fig. 4.1). Both particles have quadratic dispersion with masses m_1 and m_2, $\epsilon_{\mathbf{k},\sigma} = \mathbf{k}^2/2m_\sigma$. The electron-hole gap energy E_g is set

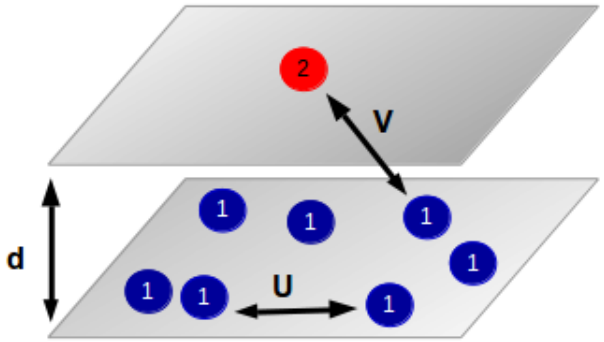

Figure 4.1: Schematic representation of an electron-hole bilayer in the fully imbalanced limit. The majority particles 1 are confined in the bottom layer, while the minority particle 2 is confined in the top layer. The distance between layers is d, and the majority particles interact repulsively between them via Coulomb interaction U and attractively via Coulomb interaction V with the minority particle.

to zero. The bare Coulomb intra- and inter-layer interactions are respectively given by $U_{\mathbf{q}} = 2\pi e^2/\epsilon\mathbf{q}$ and $V_{\mathbf{q}} = U_{\mathbf{q}} e^{-qd}$, where d is the bilayer distance, and reducing $d \to 0$, we can easily switch from bilayers to single layer case.

In order to have useful measurement units to study our system, introducing twice the reduced mass $m = 2(1/m_1 + 1/m_2)^{-1}$, we can define the exciton Bohr radius a_0 and the exciton Rydberg E_0 as

$$a_0 = \frac{\varepsilon}{me^2} \qquad\qquad E_0 = \frac{e^2}{\varepsilon a_0} = \frac{1}{ma_0^2} \,. \tag{4.4}$$

The other important parameter for the theory is the density, and in the extremely imbalanced case, where fermion 1 is the majority particle and forms a Fermi liquid of density n_1, we define the dimensionless density as:

$$r_s \equiv \frac{2}{k_F a_0} \,, \tag{4.5}$$

where $k_F = 2\sqrt{\pi n_1}$ is the Fermi wavevector. The minority particle 2 can be either a hole or an electron, and the two cases can be obtained by inverting the mass ratio $\alpha = m_2/m_1$ – for example in GaAs the electron-hole mass ratio is 4, and so if the minority particle is the electron $\alpha = 0.25$, and if it is the hole $\alpha = 4$. In terms of this mass ratio α, the free particle 1 and 2 dispersion reads as

$$\epsilon_{\mathbf{k},1} = \frac{\alpha}{1+\alpha}\frac{\mathbf{k}^2}{2m} \qquad\qquad \epsilon_{\mathbf{k},2} = \frac{1}{1+\alpha}\frac{\mathbf{k}^2}{2m}. \tag{4.6}$$

4.2 Variational molecular ground state

To establish the system phase diagram, we consider a variational ground state approach. To start with, the variational state for an excitonic quasi-particle generated by the interaction of a minority particle with a Fermi sea of majority particles is :

$$|\Psi(\mathbf{Q})\rangle = \frac{1}{\sqrt{\Omega}} \sum_{\mathbf{k}>k_F} \varphi_{\mathbf{k},\mathbf{Q}} c^\dagger_{\mathbf{Q}-\mathbf{k},2} c^\dagger_{\mathbf{k},1} \, |FS\rangle_1 \otimes |0\rangle_2 \,, \tag{4.7}$$

where $|FS\rangle_1$ represents the Fermi sea of 1-particles filled up to wave vector k_F, and we use the notation $\sum_{\mathbf{k}>k_F} \equiv \sum_{\mathbf{k}} \theta(|\mathbf{k}-k_F|)$. The normalization condition requires

$$1 = \langle \Psi(\mathbf{Q}) | \Psi(\mathbf{Q}) \rangle = \frac{1}{\Omega} \sum_{\mathbf{k}>k_F} |\varphi_{\mathbf{k},\mathbf{Q}}|^2 \, . \tag{4.8}$$

This variational state coincides in the low-density limit with the two-body state, already treated in Chapter 1, and in the high density one expects to find the non interacting state

$$|\Psi_N\rangle = c^\dagger_{\mathbf{0},2} c^\dagger_{k_F\hat{\mathbf{k}},1} |FS\rangle_1 \otimes |0\rangle_2 \ , \tag{4.9}$$

corresponding to $\varphi_{\mathbf{k},\mathbf{Q}} = \delta_{\mathbf{k},\mathbf{k}_F}\delta_{\mathbf{Q},\mathbf{k}_F}$. In this case the particles barely interact and the minority particle is not bound, occupying a state with zero momentum.

As already said, we are describing the extremely imbalanced limit. The only information about ground state that we can obtain is if particle 2 is bound to the Fermi sea of particles 1 or not. In particular we are interest in the momentum $\mathbf{Q}$ of the possible bound state. Nothing in this limit can condensate. What we expect is that, in the case there is a small density of particles 2, and thus now there can be condensation of excitons, there is a 1 to 1 correspondence with the ground states found in the extremely imbalanced limit. So in our case, if the minimum occurs for $\mathbf{Q} = 0$, then the ground state would be an ordinary SF state, while if $\mathbf{Q} \neq 0$, it will be interpret as the analogous of the FFLO state, because these are the expected phase if one slightly increase the minority particle density. To achieve these information, we need to minimize the expectation value $\langle \Psi(\mathbf{Q}) | \hat{H} - E | \Psi(\mathbf{Q}) \rangle$ with respect to the complex amplitude $\varphi_{\mathbf{k},\mathbf{Q}}$, obtaining an eigenvalue equation for the exciton energy E:

$$E\varphi_{\mathbf{k},\mathbf{Q}} = \left(\epsilon_{\mathbf{Q}-\mathbf{k},2} + \epsilon_{\mathbf{k},1} - \frac{1}{\Omega} \sum_{\mathbf{k}'<k_F} U_{\mathbf{k}-\mathbf{k}'} \right) \varphi_{\mathbf{k},\mathbf{Q}} - \frac{1}{\Omega} \sum_{\mathbf{k}'>k_F} V_{\mathbf{k}-\mathbf{k}'} \varphi_{\mathbf{k}',\mathbf{Q}} \, . \tag{4.10}$$

However, the minimum energy found have to be compared with the energy related to the normal state

$$E_N = \epsilon_{0,2} + \epsilon_{\mathbf{k}_F,1} - \frac{1}{\Omega} \sum_{\mathbf{k}'<k_F} U_{\mathbf{k}_F-\mathbf{k}'} \ , \tag{4.11}$$

to detect the presence of an unbound ground state. This energy could be calculated analytically when the interaction considered is $U_{\mathbf{q}} = 2\pi e^2/\epsilon\mathbf{q}$, and expressing it in dimensionless variables

$$\frac{E_N}{E_0} = \frac{\alpha}{1+\alpha}\left(\frac{2}{r_s}\right)^2 - \frac{4}{\pi r_s} \tag{4.12}$$

4.2.1 Screening

The expected ground states of (4.1) in the extreme limits of high ($r_s \to 0$) and low density ($r_s \to \infty$) are the following: in the high density limit the fermionic species are expected to barely interact, while in the low density limit, the electron-hole pair form an exciton. To interpolate between this two regimes, one could start to add particle-hole excitations directly in the ground state. But, if for cold atoms is possible to consider only one excitation above the Fermi sea, because the inter species interaction is short-range and the Fermi sea is non-interacting, in our system the Coulomb interaction will generate an infinite number of particle-hole excitations and any perturbative approach is bound to fail due to the long-range interaction. Thus instead of considering a finite number of excitations in the wavefunction, we include an infinite number of them considering an RPA approximation. In this approximation the Coulomb interaction is

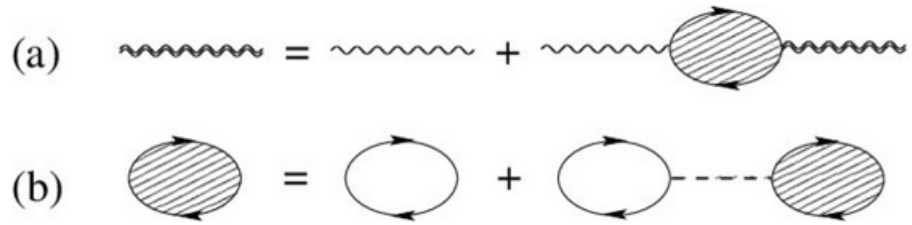

Figure 4.2: Dyson's equation for the photon propagator (a) where the Coulomb interactions is RPA screened (b).

dressed with an infinite number of electron-hole excitations. The screened interaction (Fig. 4.2 a)) is obtained considering the so called Dyson's equation, that expressed in the momentum representation is

$$U^{sc}_{\mathbf{q}} = U_{\mathbf{q}} + U_{\mathbf{q}}\Pi_{\mathbf{q}}U^{sc}_{\mathbf{q}} \,, \tag{4.13}$$

where the polarization $\Pi_{\mathbf{q}}$ gives the RPA approximation, containing all the possible first order excitations (see Fig. 4.2 b)). The polarization function is given by the Lindhard equation

$$\Pi_{\mathbf{q}} = \frac{N_s m_1}{2\pi}\left[\frac{\sqrt{q^2-4k_F^2}}{q}\theta(q-2k_F)-1\right] \,, \tag{4.14}$$

whit the number of particles flavours $N_s = 1$ for the spin polarised case. So the screened Coulomb potential will be

$$U^{sc}_{\mathbf{q}} = \frac{U_{\mathbf{q}}}{1-U_{\mathbf{q}}\Pi_{\mathbf{q}}} \qquad\qquad V^{sc}_{\mathbf{q}} = U^{sc}_{\mathbf{q}}e^{-qd} \,, \tag{4.15}$$

In our work we will consider not only the extreme case of full RPA approximation, but also the other one, the unscreened case, switching between them changing $N_s = 1$ into $N_s = 0$. The interest in this is because in some materials, like TMDC, the screening is not so effective, and so it is good to have the case without screening implemented.

A perspective for future researches is the comparison of the unscreened and RPA screened limits results with the calculation where the interaction is unscreened while we dress molecular state with a single particle-hole excitation. The variational state in this case will be

$$\begin{aligned}|\Psi(\mathbf{Q})\rangle = &\sum_{k>k_F}\varphi_{\mathbf{k},\mathbf{Q}}c^\dagger_{\mathbf{Q}-\mathbf{k},2}c^\dagger_{\mathbf{k},1}\,|FS\rangle_1\otimes|0\rangle_2 + \\ &+\frac{1}{2\Omega}\sum_{k,k',q}\varphi_{\mathbf{k},\mathbf{k}',\mathbf{q},\mathbf{Q}}c^\dagger_{\mathbf{Q}+\mathbf{q}-\mathbf{k}-\mathbf{k}',2}c^\dagger_{\mathbf{k},1}c^\dagger_{\mathbf{k}',1}c_{\mathbf{q},1}\,|FS\rangle_1\otimes|0\rangle_2 \,,\end{aligned} \tag{4.16}$$

4.3 Phase diagram

In order to get the phase diagram of the fully imbalanced bilayer system, we convert the eigenvalue equation Eq. (4.10) into a matrix equation and numerically solving it for the lowest energy eigenvalue. To do so we use Gauss-Legendre quadrature method, in detail in the Appendix A. To establish the minimal number of parameters we need to describe the diagram, we rescale energies by the exciton Rydberg E_0 and wave-vectors by the inverse exciton Bohr radius a_0 and introduce the dimensionless variables:

$$\tilde{k} = ka_0 \qquad \tilde{d} = \frac{d}{a_0} \qquad \tilde{\epsilon}_{\mathbf{k},1} = \frac{\epsilon_{\mathbf{k},1}}{E_0} = \frac{\alpha}{1+\alpha}\tilde{k}^2 \qquad \tilde{\epsilon}_{\mathbf{k},2} = \frac{\tilde{k}^2}{1+\alpha} \,. \tag{4.17}$$

4.3.1 Numerical implementation

The symmetric matrix equation obtained via Gauss-Legendre quadrature method is solved writing a Python code, with the aim of calculate the minimum eigenvalue for a fixed $\mathbf{Q}$, and then found $\mathbf{Q}_{min}$ at which the energy is the lowest possible. The code idea is quite simple.

First we define the matrix equation for a fixed number of point N_t and N_k, used for the discretization described in the Gauss method, and for a fixed value of $\mathbf{Q}$. Then we solve the problem using a routine of Python that calculates the eigenvalues and eigenvectors of the matrix, selecting the minimum. The value found will depend on the number of point used to approximate the integrals with the quadrature method. So what we do is to repeat this procedure for different values of N_t and N_k, fitting them for N_t, $N_k \to \infty$ with a polynomial function – for an explanation on the choice of N_t, N_k and the grade of the polynomial function, we remind at the Appendix B. The last step is to repeat this procedure for different values of $\mathbf{Q}$, selected using a bisection method, to reveal the one corresponding to the state with minimum energy.

4.3.2 Bilayer with RPA screening

To be able to compare our Python simulations with existing and known results, we start considering a situation with two layers at a distance $d = a_0$, using RPA screened interactions, the same configuration considered in Ref. [49]. Results are plotted in Fig 4.3. We fix the electron-hole mass ratio to 1 ($\alpha = 1$) and to 4, that is approximately the value in GaAs structures ($\alpha = \{0.25, 4\}$).

In the low density limit $r_s \to \infty$ we trivially recover the two-body limit, with a bound state at $Q = 0$. We refer to this state as superfluid state (SF). In the other limit, with small r_s, the screened interaction cause the exciton to unbind, and so we talk about normal phase (N) (see Eq. (4.9)). The interesting aspect is that, at intermediate densities, the phase diagram shows a ground state characterized by a bound state with finite momentum, exactly what we called FFLO state. From Fig. 4.5, the FFLO region is enhanced and shifted to larger r_s if the minority particle is lighter ($\alpha = 4$) than the other. The reason is that, to maintain a molecular state with $\mathbf{Q} = 0$, the minority particle have to sit above the Fermi sea. This implies a kinetic cost that is bigger if α is smaller. This favours the FFLO state, with the minority particle that now sits below the Fermi level. The FFLO region is also enhanced and shifted towards bigger value of r_s increasing the bilayer distance, because increasing d, the large momentum scattering is suppressed by $V^{sc}_{\mathbf{k}-\mathbf{k}'}$. Finally we note that, in each case, the transitions are second order (see Fig. 4.4).

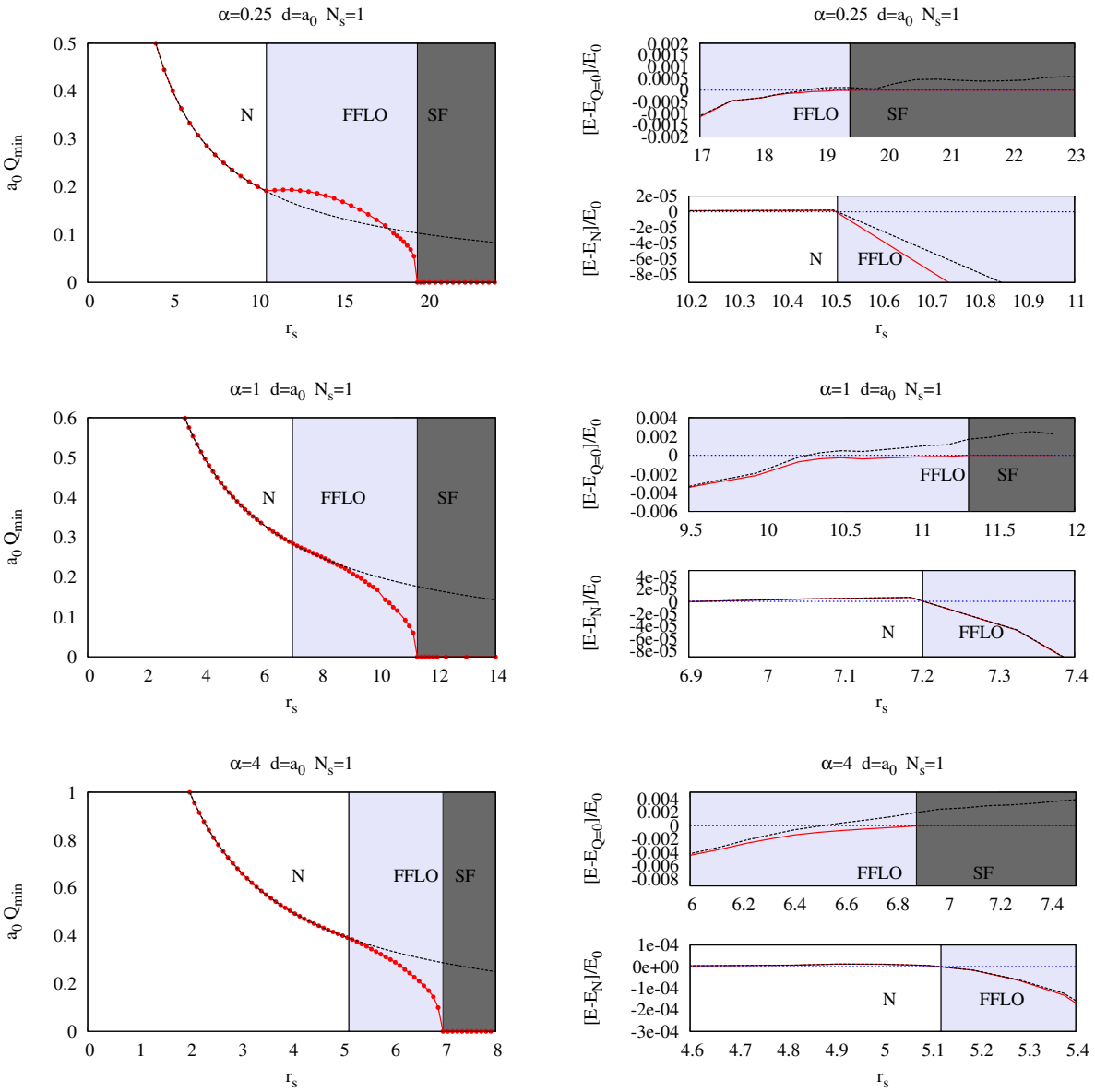

Figure 4.3: Left panels: Momentum Q_{min} minimizing the exciton's energy as a function of r_s for $\alpha = 0.25$ (top), $\alpha = 1$ (center), $\alpha = 4$ (bottom). $d = a_0$ and the interaction considered is an RPA screened Coulomb interaction ($N_s = 1$). The dashed black line correspond to the Fermi momentum $Q = k_F \equiv 2/r_s a_0$. Three different phases are present: the normal (N) unbound phase, the bound state with $Q \neq 0$ (FFLO), and the superfluid phase (SF). Q_{min} evolves continuously from 0 to k_F, with always a second order transition through the three phases (see Fig. 4.4). Right panels: values of the energy at $\mathbf{Q}_{min}$ as a function of r_s, rescaled respect the energy $E_{\mathbf{Q}=0} = E(\mathbf{Q} = 0)$ for intermediate values of r_s, and respect the normal energy $E_N = E(\mathbf{Q} = \mathbf{k}_F)$ for smaller value of r_s.

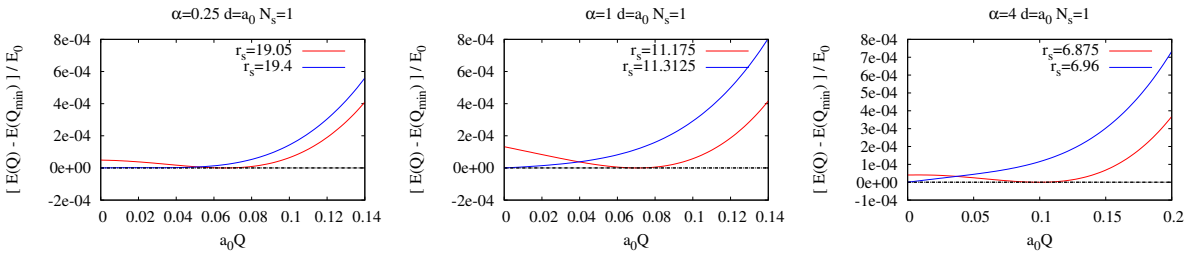

Figure 4.4: Energy of the ground state as a function of Q, for values of r_s before and after the FFLO-SF transition. $d = a_0$ and the interaction considered is an RPA screened Coulomb interaction ($N_s = 1$). In each case the transition is a second order.

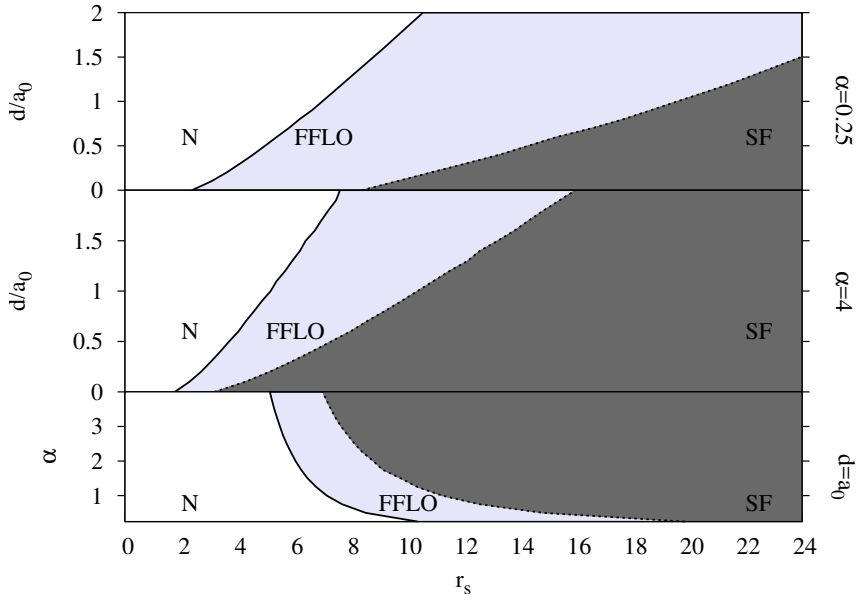

Figure 4.5: Comparison between different transition thresholds numerically calculated solving the eigenvalue equation (4.10), as a function of r_s. The interaction considered is an RPA screened Coulomb interaction ($N_s = 1$). In the top two panels, the mass ratio is fixed and the bilayer distance is changed. In the bottom panel the distance is fixed and the mass ratio is changed. Data taken from [49]

4.3.3 Single layer without RPA screening ($N_s = 0$)

We now treat the unscreened case, describing as an example the single layer case, and then extending the results at different values of d and α. What one expects is that the FFLO region depends on the particular screening considered. To understand this it is useful to note that the eigenvalue equation (4.10) coincides with the mean-field gap equation of the BEC-BCS crossover theory $\Delta_{\mathbf{k},\mathbf{Q}} = \frac{1}{\Omega}\sum_{k'>k_F} V^{sc}_{\mathbf{k}-\mathbf{k}'}\varphi_{\mathbf{k}',\mathbf{Q}}$. Neglecting the intra-layer Coulomb interaction, we obtain

$$\Delta_{\mathbf{k},\mathbf{Q}} = -\frac{1}{\Omega}\sum_{k'>k_F} V^{sc}_{\mathbf{k}-\mathbf{k}'}\frac{\Delta_{\mathbf{k}',\mathbf{Q}}}{E-\epsilon_{\mathbf{Q}-\mathbf{k}',2}-\epsilon_{\mathbf{k}',1}}\,. \tag{4.18}$$

In the unscreened case, writing it in a continuous form, one obtains

$$\Delta_{\mathbf{k},\mathbf{Q}} = \int_{k'>\frac{2}{r_s}} \frac{d\mathbf{k}'}{2\pi}\frac{e^{-d|\mathbf{k}-\mathbf{k}'|}}{|\mathbf{k}-\mathbf{k}'|}\frac{\Delta_{\mathbf{k}',\mathbf{Q}}}{-E+\epsilon_{\mathbf{Q}-\mathbf{k}',2}+\epsilon_{\mathbf{k}',1}}\,. \tag{4.19}$$

At the unbinding transition we have $\mathbf{Q} = \mathbf{k} = \mathbf{k}' = 2/r_s$ and $E = E_N = 4\alpha/r_s^2(1+\alpha)$ (see Appendix A). In this case the integral in Eq. (4.19) is logarithmically divergent, and we must take $r_s = 0$ to avoid it. So, for the unscreened interaction, the FFLO phase occupies the high density region, having always an energy lower than the N phase. Note that this is not the case when the interaction is screened, where the singularity at $\mathbf{k}' = \mathbf{k}$ is removed, leaving an integrable singularity at $\mathbf{Q} = \mathbf{k}' = \frac{2}{r_s}\hat{\mathbf{k}}$. This phenomenon is well represented in Fig. 4.6, where we plot the phase diagram for $\alpha = 0.25, 1, 4$, where the FFLO phase suppress completely the normal phase. The only transition in the system is the FFLO-SF, and studying its behavior, we found that for $\alpha = 0.25$ it is second order, whereas for $\alpha = 4$ and $\alpha = 1$ the transition is first order (see Fig. 4.7).

Let's now compare the effects of unscreened and screened interaction . In Fig. 4.8 we report the phase diagrams for the unscreened case, with also the screened FFLO-SF transition threshold – dashed lines. For $\alpha = 0.25$ we found very similar results. As already said the normal phase is completely suppressed, and the FFLO phase is preferred over the SF phase increasing the bilayer distance. The motivation is the same as before, with now a slightly shift for lower r_s, because the interlayer Coulomb attraction is greater, and can better balance the kinetic cost of the minority particle. In both case the transition is second order. For $\alpha = 4$ the FFLO again is enhanced increasing the distance, but now is strongly frustrated with respect the screened case. This because the low energy cost of the minority particle to occupy a state with $\mathbf{k} \neq 0$ is efficiently balanced by the stronger Coulomb inter-layer attraction, allows SF state for lower r_s then in the screened case. The other significant difference is in the transition behavior, that now is first order. The last panel of Fig. 4.8 shows a brief recap of what seen, with the two different behavior of the transition in the unscreened case, and with the transition threshold that, decreasing α, tends to the one calculated for the screened case.

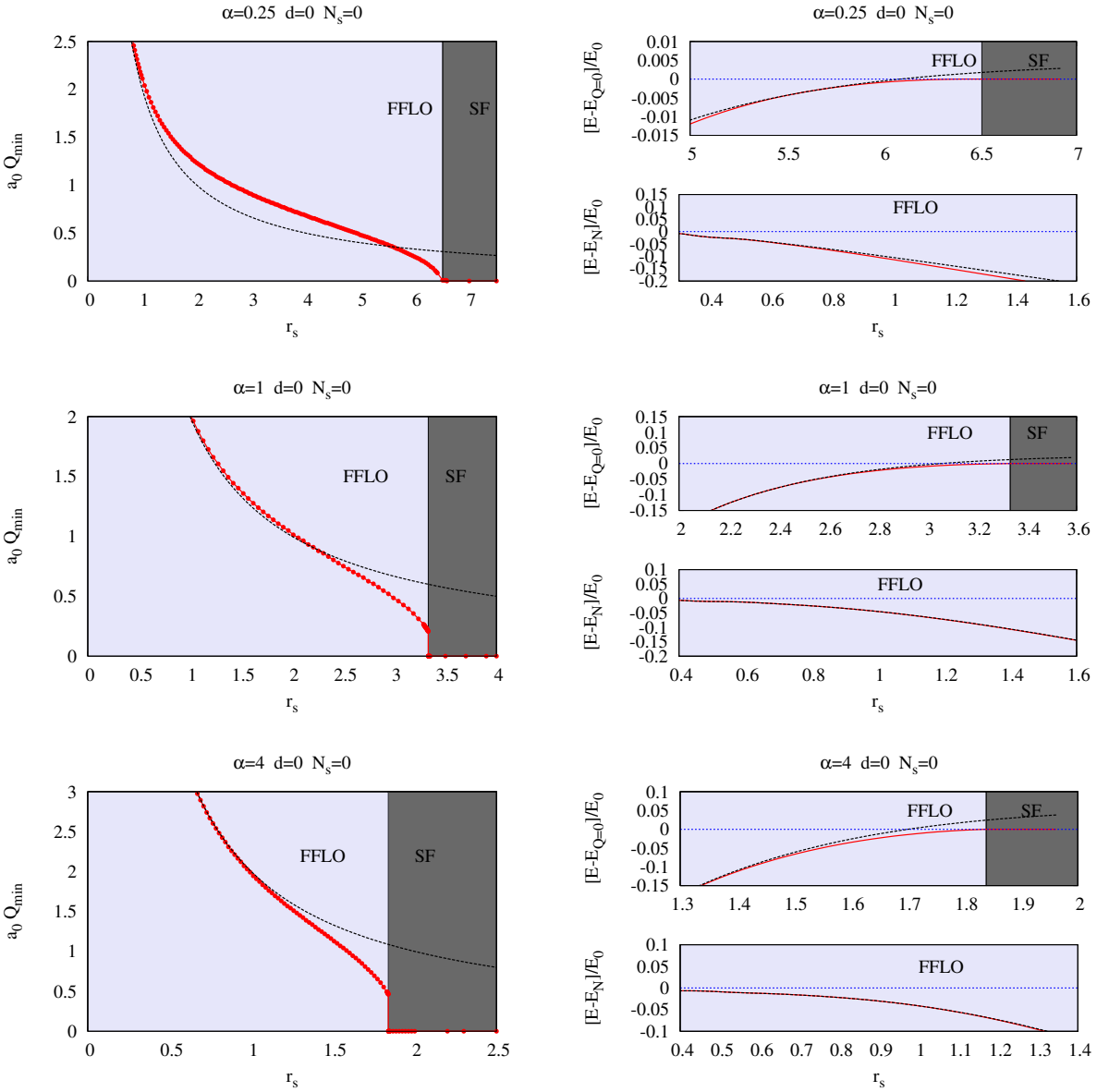

Figure 4.6: Left panels: Momentum Q_{min} that minimize the exciton's energy as a function of r_s for $\alpha = 0.25$ (top), $\alpha = 1$ (center), $\alpha = 4$ (bottom). The distance d is fixed at 0 and the interaction considered is a unscreend Coulomb interaction ($N_s = 0$). The dashed black line correspond to $Q = k_F \equiv 2/r_s a_0$, the Fermi momentum. Two different phases are present: the bound state with $Q \neq 0$ (FFLO), and the superfluid phase (SF). Q_{min} evolves continuously from 0 to k_F only for $\alpha = 0.25$, with a second order transition through the three phases. For different α first order transitions appear. Right panels: For great r_s, the exciton energy at $Q = Q_{min}$ (red line) and at $Q = k_F$ (black dashed line) are rescaled respect to the exciton's energy at $Q = 0$. For small r_s they are rescaled respect the unbound energy E_N.

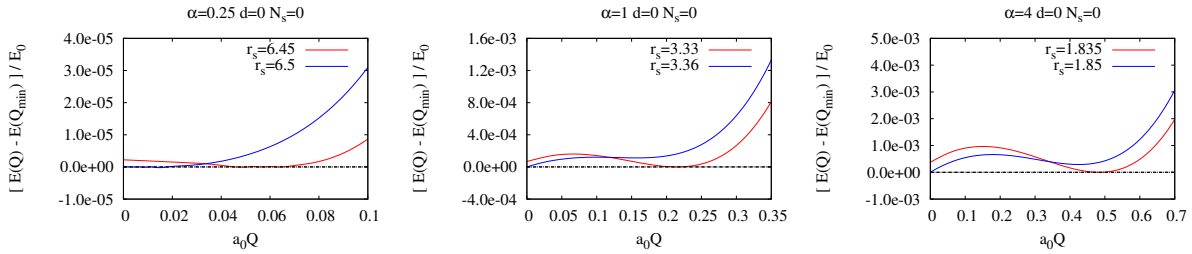

Figure 4.7: Energy of the ground state as a function of Q, for values of r_s before and after the FFLO-SF transition. The distance d is fixed at 0 and the interaction considered is an unscreened Coulomb interaction ($N_s = 0$). For $\alpha = 0.25$ the transition is second order, whereas for $\alpha = \{1, 4\}$ first order

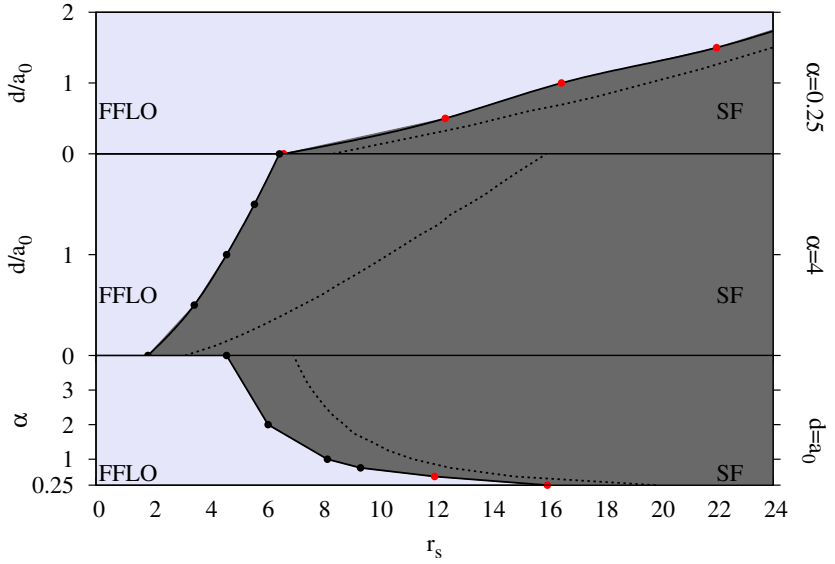

Figure 4.8: Phase diagrams numerically calculated solving the eigenvalue equation (4.10), as a function of r_s. The interaction considered is an unscreened Coulomb interaction ($N_s = 0$). For comparison, we plot also the FFLO-SF transition treshold for the screened case – dashed lines. In the top two panels, the mass ratio is fixed and the bilayer distance is changed. If $\alpha = 0.25$ the transition is second order – red dots – as in the screened case, whereas when $\alpha = 4$ the transition is first order – black dots. The bottom panel shows a brief recap of the difference between unscreened and screened case, where the distance is fixed and the mass ratio is changed.

4.4 Summary of results and conclusions

We have studied the full density imbalanced electron-hole layers and bilayers, considering both screened and unscreened Coulomb interactions. As predicted the elusive FFLO state was found in each case, and through the phase diagrams is possible to characterized its behavior. First of all we saw that the screening plays an important role. If the interaction considered is unscreened, the FFLO state is the dominant state in the high density regime. But in presence of screened interaction the FFLO phase for low values of r_s is suppressed by the unbound state. In the high density limit the situation is different, where an FFLO state in the screened case is preferred over the superfluid phase for higher values of r_s with respect the unscreened case, where the FFLO-SF transition is slightly shifted towards smaller r_s. The other interesting dependence is on the layers distance. The greater it is, the wider is the FFLO region, because now the less effective inter-layer Coulomb interaction allows states with $\mathbf{Q}_{min} = 0$ only for lower values of density. In the screened case also the normal phase is shifted towards greater r_s, but at fixed α the overall effect increasing the distance is to increase the range in which the FFLO state appears. The last aspect to consider is the dependence on the mass ratio. When the minority particle is lighter than the majority, the FFLO is allowed for greater values of r_s. This because lighter particles have a greater energy cost occupying a state with momentum $\mathbf{k}_F$, and so state with $\mathbf{Q} \neq 0$ are preferred over superfluid state. As in the previous discussion, in the screened case the normal phase have the same low density shifting, and the overall effect is that for lower values of α the FFLO region is greater.

In conclusion, we have shown that peculiar pairing phenomena like FFLO state are possible when the electron-hole bilayers are prepared with a density imbalance, giving also an overview on the behavior of this phase changing the typical tunable parameters of the system.

Chapter 5

Electron-hole layer and bilayer with large density imbalance coupled to light

The interesting and peculiar pairing phenomena found studying the electron-hole bilayers with large density imbalance are now analyzed for a case where the system is embedded into a microcavity. Again, in our study we consider the extreme imbalance case, whit only one minority particle, to address the problem in a more controlled manner and to allow the formation of exotic scenario, like FFLO states. The confinement also enhances the experimental detection of these states. In fact one way to observe signatures of the finite-momentum pairing , is through the angular emission of photon after the electron-hole recombination. Photon that is now confined and coupled with the exciton itself.

5.1 Model

The Hamiltonian we use to describe the electron-hole layer and bilayers confined in a cavity is – $\hbar = 1$ and Ω is the system volume:

$$\hat{H} = \hat{H}_0 + \hat{H}_C + \hat{H}_{int} + \hat{H}_{eh-ph} \tag{5.1}$$

$$\hat{H}_C = \sum_{\mathbf{q}} \omega_{\mathbf{q},C} c^\dagger_{\mathbf{q},C} c_{\mathbf{q},C} \tag{5.2}$$

$$\hat{H}_{eh-ph} = \frac{g}{\sqrt{\Omega}} \sum_{\mathbf{k},\mathbf{q}} e^{-(k/k_c)^2} \left(c^\dagger_{\mathbf{k},1} c^\dagger_{\mathbf{q}-\mathbf{k},2} c_{\mathbf{q},C} + \text{h.c.} \right) , \tag{5.3}$$

where $\hat{H}_0$ and $\hat{H}_{int}$ are the same as in the case without confinement, Eqs. (4.2) and (4.3), $c_{\mathbf{q},C}$ is the annihilation operator of the photon and $\omega_{\mathbf{q},C}$ its energy. Again, we consider both the unscreened and RPA screened interaction. The cavity photon dispersion relation is

$$\omega_{\mathbf{q},C} = \omega_{\mathbf{0},C} + \frac{q^2}{2m_{\mathrm{C}}} \qquad\qquad \omega_{\mathbf{0},C} = \delta - E_0 \, , \tag{5.4}$$

with the photon mass being typically $m_{\mathrm{C}} = 10^{-4} m_{\mathrm{X}}$, and we measure the lowest photon energy with respect the lowest excitonic one by introducing the cavity-photon detuning δ. Finally, for the matter-light coupling, we use the same renormalized contact interaction discussed in Chapter 1, where g is the coupling strength and k_c is the momentum cut-off.

5.2 Variational molecular ground state

Our purpose is to obtain information about the ground state at different densities and different values of the detuning δ, and to describe the resulting phase diagram. We do so using a variational approach. The variational state for an excitonic quasi-particle on top of a Fermi sea of majority particles, confined in a microcavity, is :

$$|\Psi(\mathbf{Q})\rangle = \frac{1}{\sqrt{\Omega}} \sum_{\mathbf{k}>k_F} \varphi_{\mathbf{k},\mathbf{Q}} c^\dagger_{\mathbf{Q}-\mathbf{k},2} c^\dagger_{\mathbf{k},1} |FS\rangle_1 \otimes |0\rangle_2 \otimes |0\rangle_{ph} + \alpha_{\mathbf{Q}} c^\dagger_{\mathbf{Q},C} |FS\rangle_1 \otimes |0\rangle_2 \otimes |0\rangle_{ph} \ , \quad (5.5)$$

similar to Eq. (4.7), where now we add a photonic coherent state. The normalization condition requires $1 = \langle\Psi(\mathbf{Q})|\Psi(\mathbf{Q})\rangle = \frac{1}{\Omega}\sum_{\mathbf{k}>k_F} |\varphi_{\mathbf{k},\mathbf{Q}}|^2 + |\alpha_{\mathbf{Q}}|^2$. Though the minimization of the expectation value $\langle\Psi(\mathbf{Q})|\,(\hat{H}-E)\,|\Psi(\mathbf{Q})\rangle$ with respect to the complex amplitudes $\varphi_{\mathbf{k},\mathbf{Q}}$ and $\alpha_{\mathbf{Q}}$, one obtains two coupled eigenvalue equations for the polariton energy E:

$$E\varphi_{\mathbf{k},\mathbf{Q}} = \left(\epsilon_{\mathbf{Q}-\mathbf{k},2} + \epsilon_{\mathbf{k},1} - \frac{1}{\Omega}\sum_{\mathbf{k}'<k_F} U^{(sc)}_{\mathbf{k}-\mathbf{k}'}\right)\varphi_{\mathbf{k},\mathbf{Q}} - \frac{1}{\Omega}\sum_{\mathbf{k}'>k_F} V^{(sc)}_{\mathbf{k}-\mathbf{k}'}\varphi_{\mathbf{k}',\mathbf{Q}} + g e^{-(k/k_c)^2}\alpha_{\mathbf{Q}} \quad (5.6)$$

$$E\alpha_{\mathbf{Q}} = \omega_{\mathbf{Q},C}\alpha_{\mathbf{Q}} + \frac{g}{\Omega}\sum_{\mathbf{k}>k_F} e^{-(k/k_c)^2}\varphi_{\mathbf{k},\mathbf{Q}} \ . \quad (5.7)$$

where the interaction between particles can be unscreened or screened. The minimum energy of the bound state have to be compared with the one of the possible normal states.

In this case one expects three different possibilities. The first two are related with the situation in which the exciton is in an unbound state and the photon is non interacting, occupying a zero momentum state

$$|\Psi_N\rangle_1 = c^\dagger_{\mathbf{0},2} c^\dagger_{k_F\hat{\mathbf{k}},1} |FS\rangle_1 \otimes |0\rangle_2 \otimes |0\rangle_{ph} \quad (5.8)$$

$$|\Psi_N\rangle_2 = c^\dagger_{\mathbf{0},C} |FS\rangle_1 \otimes |0\rangle_2 \otimes |0\rangle_{ph} \ . \quad (5.9)$$

The energy E^1_N related to the first normal state is exactly Eq. (4.11), whereas $E^2_N = \omega_{0,C}$.

The other expected normal state, instead, is characterized by the exciton in its normal state, with a relative momentum $\mathbf{k}_F$, interacting with the photon. Of course the photon needs to have a finite momentum $\mathbf{k}_F$.

$$|\Psi_N\rangle_3 = \xi c^\dagger_{\mathbf{0},2} c^\dagger_{k_F\hat{\mathbf{k}},1} |FS\rangle_1 \otimes |0\rangle_2 \otimes |0\rangle_{ph} + \sqrt{1-\xi^2} c^\dagger_{k_F\hat{\mathbf{k}},C} |FS\rangle_1 \otimes |0\rangle_2 \otimes |0\rangle_{ph} \ . \quad (5.10)$$

The energy E^N_3 can be found analytically, solving the coupled eigenvalue equations Eqs. (5.6) and (5.7) for $\mathbf{k} = \mathbf{q} = k_F\hat{\mathbf{k}}$, without the inter-layer Coulomb interaction contribution

$$E\xi = \left(\epsilon_{\mathbf{0},2} + \epsilon_{\mathbf{k}_F,1} - \frac{1}{\Omega}\sum_{\mathbf{k}'<k_F} U^{(sc)}_{\mathbf{k}_F-\mathbf{k}'}\right)\xi + \frac{g}{\sqrt{\Omega}} e^{-(k_F/k_c)^2}\sqrt{1-\xi^2} \quad (5.11)$$

$$E\sqrt{1-\xi^2} = \omega_{\mathbf{k}_F,C}\sqrt{1-\xi^2} + \frac{g}{\sqrt{\Omega}} e^{-(k_F/k_c)^2}\xi \ . \quad (5.12)$$

These coupled equations are now symmetric and can be diagonalized

$$E\begin{pmatrix} \xi \\ \sqrt{1-\xi^2} \end{pmatrix} = \begin{pmatrix} \epsilon_{\mathbf{0},2} + \epsilon_{\mathbf{k}_F,1} - \frac{1}{\Omega}\sum_{\mathbf{k}'<k_F} U^{(sc)}_{\mathbf{k}_F-\mathbf{k}'} & \frac{g}{\sqrt{\Omega}} e^{-(k_F/k_c)^2} \\ \frac{g}{\sqrt{\Omega}} e^{-(k_F/k_c)^2} & \omega_{\mathbf{k}_F,C} \end{pmatrix} \begin{pmatrix} \xi \\ \sqrt{1-\xi^2} \end{pmatrix} \ , \quad (5.13)$$

The solution will be something very similar to the lower and upper polariton energy

$$E_N^3 = \frac{\omega_{\mathbf{k}_F,C} + E_N^1}{2} - \left[\left(\frac{g}{\sqrt{\Omega}} e^{-(k_F/k_c)^2}\right)^2 + \frac{(\omega_{\mathbf{k}_F,C} - E_N^1)^2}{4}\right]^{1/2} , \tag{5.14}$$

where $E_N^1 = \epsilon_{\mathbf{0},2} + \epsilon_{\mathbf{k}_F,1} - \frac{1}{\Omega}\sum_{\mathbf{k}'<k_F} U^{(sc)}_{\mathbf{k}_F-\mathbf{k}'}$. In the high-density limit ($r_s \ll 1$) or when the detuning is very high, the photon energy is much more bigger then the other energies, and so the previous equation can be approximated as

$$E_3^N \xrightarrow{\omega_{\mathbf{k}_F,C} \gg g, E_1^N} E_1^N - \frac{(g e^{-(k_F/k_c)^2})^2}{\Omega \omega_{\mathbf{k}_F,C}} , \tag{5.15}$$

that implies $E_3^N \leq E_1^N$.

In conclusion, what we have to do is to calculate the minimum energy from Eqs. (5.6) and (5.7), comparing it with the normal energy E_3^N and E_2^N. To solve the eigenvalue equations, we convert them into a matrix equation and numerically solving it for the lowest energy eigenvalue. We use Gauss-Legendre quadrature method, described in the Appendix A, where we also simplify the notation with dimensionless variables, rescaling energies by the exciton Rydberg E_0 and wave-vectors by the inverse exciton Bohr radius a_0 and introduce

$$\tilde{k} = k a_0 \quad \tilde{d} = \frac{d}{a_0} \quad \tilde{\delta} = \frac{\delta}{E_0} \quad \tilde{\epsilon}_{\mathbf{k},1} = \frac{\epsilon_{\mathbf{k},1}}{E_0} = \frac{\alpha}{1+\alpha}\tilde{k}^2 \quad \tilde{\epsilon}_{\mathbf{k},2} = \frac{\tilde{k}^2}{1+\alpha} \quad \tilde{g} = \frac{g}{E_0 a_0} . \tag{5.16}$$

5.2.1 Unscreened interaction

To start with, we present in this section the unscreened Coulomb interaction case ($N_s = 0$) for both single layer and bilayers.

In the left panels of Figs. 5.1 5.2 we show the value of the momentum $\mathbf{Q}_{min}$, related with the energy $E(\mathbf{Q}_{min})$ that minimize Eqs. (5.6) and (5.7), as a function of detuning and the dimensionless density. In the resulting maps we clearly see a region, in the pictures delimited by a grey line, where the values of $\mathbf{Q}_{min}$ is not zero. Above each map, a section is shown at a fixed detuning. In the range of r_s at which the mentioned region is present, $\mathbf{Q}_{min}$ values are the same found in the previous chapter. If now we plot the photon fraction as a function of δ and r_s (see right panels of Figs. 5.1 and 5.2) one sees that the above mentioned region is characterized by a very low value of $|\alpha_{\mathbf{Q}}|^2$. We will refer at this region as excitonic region, because the behavior of the ground state inside it will be the same found in the not confined case.

Outside, $\mathbf{Q}_{min} = 0$ and the photon fraction starts to increase. We identify this state as a polariton superfluid. However, we already seen in Chapter 3 that the polariton changes with respect photon presence. Looking at the map section for fixed r_s at the side of each map, we see how fast is the transition between $|\alpha_{\mathbf{Q}}|^2 = 0$ and $|\alpha_{\mathbf{Q}}|^2 = 1$ changing δ. So, we decide to make a distinction between mostly excitonic polariton superfluid, when $|\alpha_{\mathbf{Q}}|^2 < 0.1$ (SF), polariton superfluid, when $0.1 < |\alpha_{\mathbf{Q}}|^2 < 0.9$ (SF$_{pol}$), and mostly photonic polariton superfluid (SF$_{ph}$).

In Fig. 5.3 we summarize together the results mentioned above in an inclusive phase diagram. First of all, as expected for the unscreened case, there is no normal state in both single layer and bilayers configurations. The excitonic region, that is always below the FFLO-SF transition threshold founded in the previous chapter – dashed lines in the pictures, is characterized by an excitonic FFLO phase. One expects to recover, for $\delta \to \infty$, the limit studied before, and so the FFLO-SF transition represents the asymptotically limit of the right side of the region. Outside we have only superfluid phase. Differently from the excitonic case, now the photon influence

allows superfluid phase also for very high density, due to the enhancement of the electron-hole interaction. Finally, on the right side of each diagram we plot the value of Rabi splitting for $r_s \to \infty$, using both Eq. (1.65) – red line – and Eq. (1.67) -black line. This energy splitting represents the effective experimental control on the strength of the coupling in the cavity. From this one can re-obtain the values of g and k_c. So knowing the magnitude of the splitting gives important information of the system.

Summary of results and conclusion

What we can conclude is that the photon presence changes the ranges of r_s in which is possible to detect an FFLO state. While long-range Coulomb interactions promote the formation of the finite momentum FFLO condensed phase, the mixing with a low-mass photon suppress that phase, or contrariwise the coupling to light is inhibited by the formation of an FFLO state. The competition between these two effects leads to interesting results. In particular, when δ is negative the FFLO is completely eliminated, and only a mostly photonic polariton region is present. For very high values of δ one expect to recover exactly the same case studied before, with an FFLO state that, in the unscreened case, is extended until very small values of r_s. Instead for small positive values of the detuning the FFLO region shape depends strictly on α and d. From Fig. 5.3 we can see that, considering the single layer case in the high density limit, the FFLO region is more suppressed for bigger values of α. Contrarily, for higher value of r_s, the SF phase suppresses the FFLO region more when $\alpha = 0.25$ than for $\alpha = 4$. The frustrated FFLO phase is a signature of the enhanced interaction between electron and hole, mediated by the photon, that permits bound state with $\mathbf{Q} = 0$ for value of r_s not allowed without confinement. In the SF_{ph} the photon contribution is maximal, allowing superfluid state in the very high density limit. In the SF_{pol} phase there is a strongest mixing between light and matter, but only occurs at intermediated densities, in a small interval of photon detuning, in a phase where polariton condensation occurs, as expected, at zero center of mass momentum. In the SF state the interaction is mainly Coulomb attraction, but the photon presence is such that the FFLO-SF transition is slightly shifted towards lower values of r_s with respect the case studied before. To conclude, the overall effect of increasing the distance is to favours the SF state over the FFLO one in the low density regime.

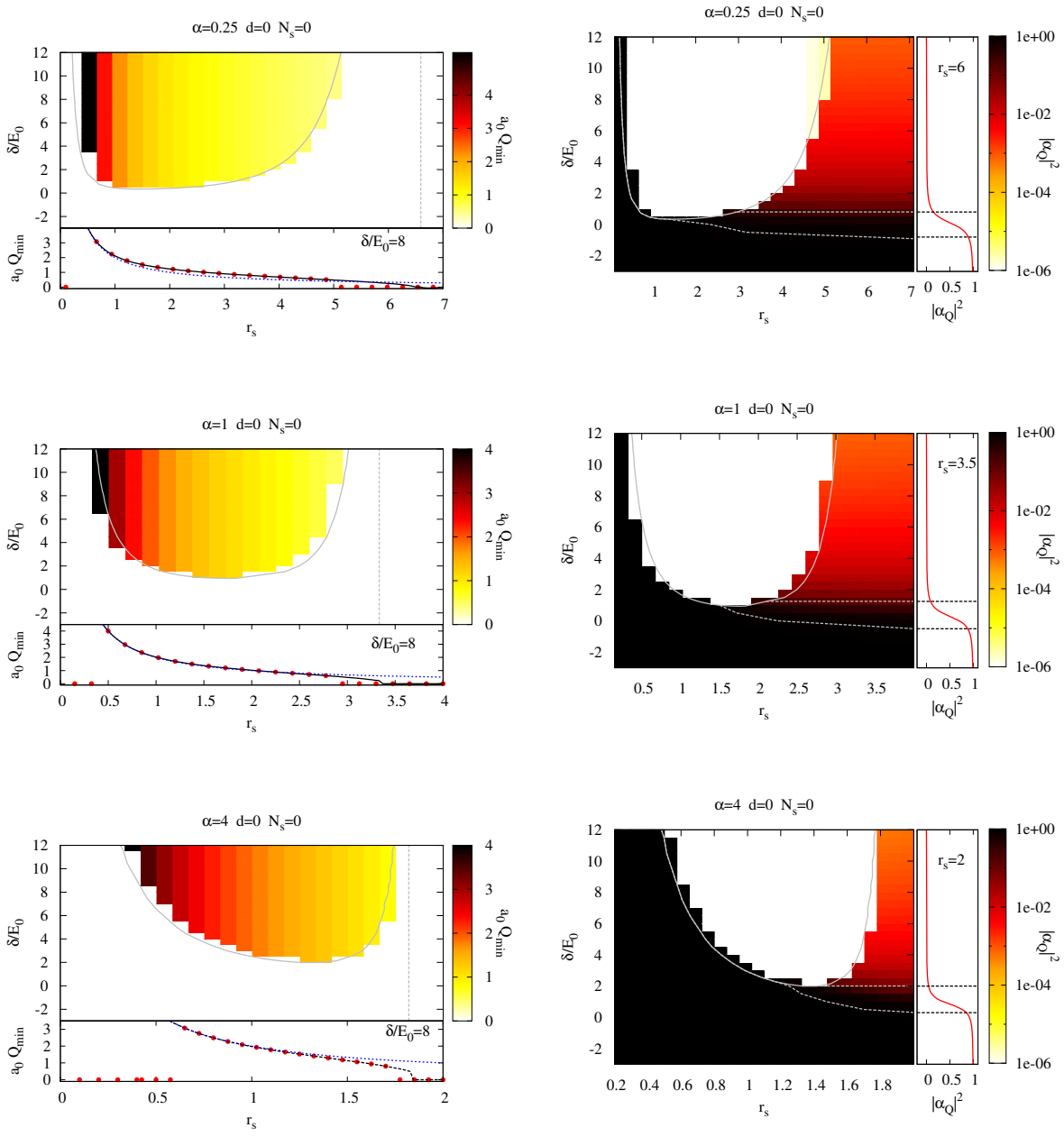

Figure 5.1: For the production of these maps we set the light-matter strength $g = E_0 a_0$ and the momentum cut-off at $k_c = 2/a_0$, considering the unscreened Coulomb interaction between the two fermionic species contained in a single layer. Left panels: minimum value of the momentum $\mathbf{Q}_{min}$ relative to the minimum energy of the system as a function of detuning δ and r_s. The grey line delimits the excitonic region.. Below each map, we show a section at fixed δ. Right panels: photon fraction as a function of δ and r_s. In the excitonic region its value is very low. Outside the photon fraction increase. Next to each graphs we plot a section for fixed r_s. The dashed lines indicate the area in which the value of photon fraction is between 0.1 and 0.9

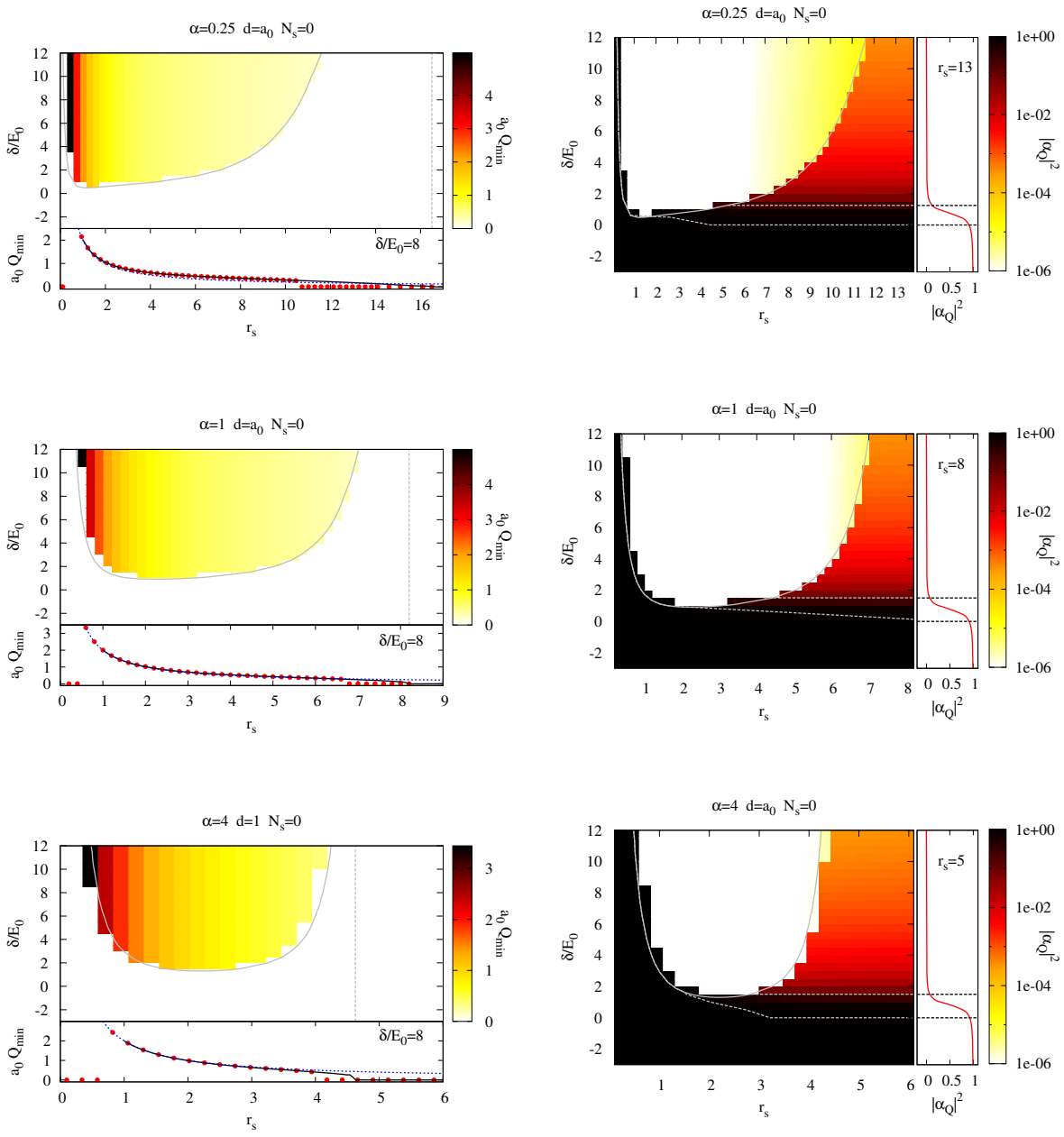

Figure 5.2: Same figure as Fig. 5.1, with now $d = a_0$.

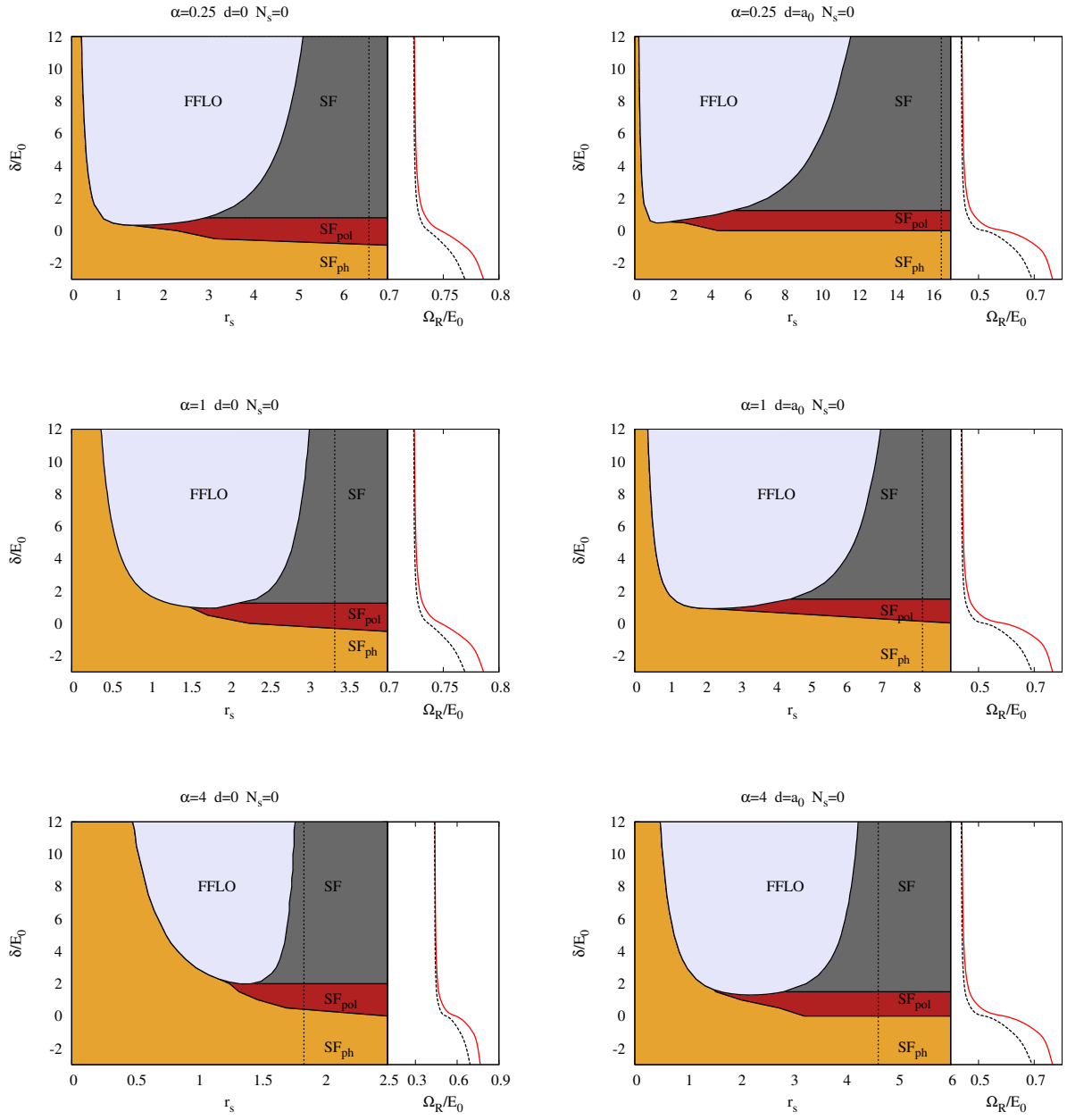

Figure 5.3: Outside the region the three different polaritonic states are shown: mostly excitonic polariton superfluid phase (SF), polariton superfluid (SF_{pol}) and mostly photonic polariton superfluid phase (SF_{ph}). On the left of each diagram the Rabi splitting for $r_s = \infty$ is shown, calculated with Eq. (1.65) – red line – and Eq. (1.67) – black dashed line.

5.2.2 Screened case

The discussion on Figs. 5.5 and 5.6 for the screened case is the same as before, where again is possible to detect the presence of an excitonic region where $|\alpha_{\mathbf{Q}}|^2$ is very low. Now we need to be aware of the possible presence of a normal state, and in Fig. 5.7 we show the comparison between the energy of the ground state $E(\mathbf{Q}_{min})$ and the normal energy E_3^N, obtaining the definitive phase diagrams for the single layer and bilayers confined into a microcavity. In each diagram we show the threshold of the N-FFLO transition – dotted line – and of the FFLO-SF transition – dashed line – for the unconfined system. In the single layer case, we see that the normal phase N_3 is slightly shifted towards greater values of r_s respect the normal phase founded in the unconfined case, reducing the FFLO phase. In order to re-obtain the case treated in the previous chapter for $\delta \to \infty$, one expects this transition threshold asymptotically tends to the old one. However in our diagrams the N_3-FFLO transition appears not depending on δ, because in the range chosen E_3^N doesn't change significantly. The superfluid phase remain mainly untouched. If now one considers the bilayers system, the normal state start to have a greater impact. In Fig. 5.7 the normal phase completely suppress the FFLO state, influencing also the excitonic polariton superfluid state, that result frustrated. However, as already said, we expect to recover the result found previously when $\delta \to \infty$. So we expect a re-entrance of the normal phase, with the consequent re-appearance of the FFLO state for greater value of δ. As an example, in Fig. 5.4, we show that for $\alpha = 4$ and $r_s = 6$ the re-appearance of the FFLO state is expected for a value of the detuning of the order of $\approx 400 E_0$.

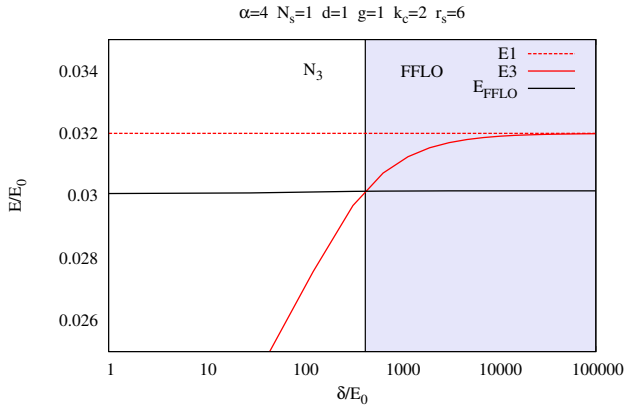

Figure 5.4: Comparison between the energy of the FFLO state – black line – with respect E_3^N – red line, when $\alpha = 4$ and $r_s = 6$. The re-appearance of the FFLO state is expected for a value of the detuning of the order of $\approx 400 E_0$

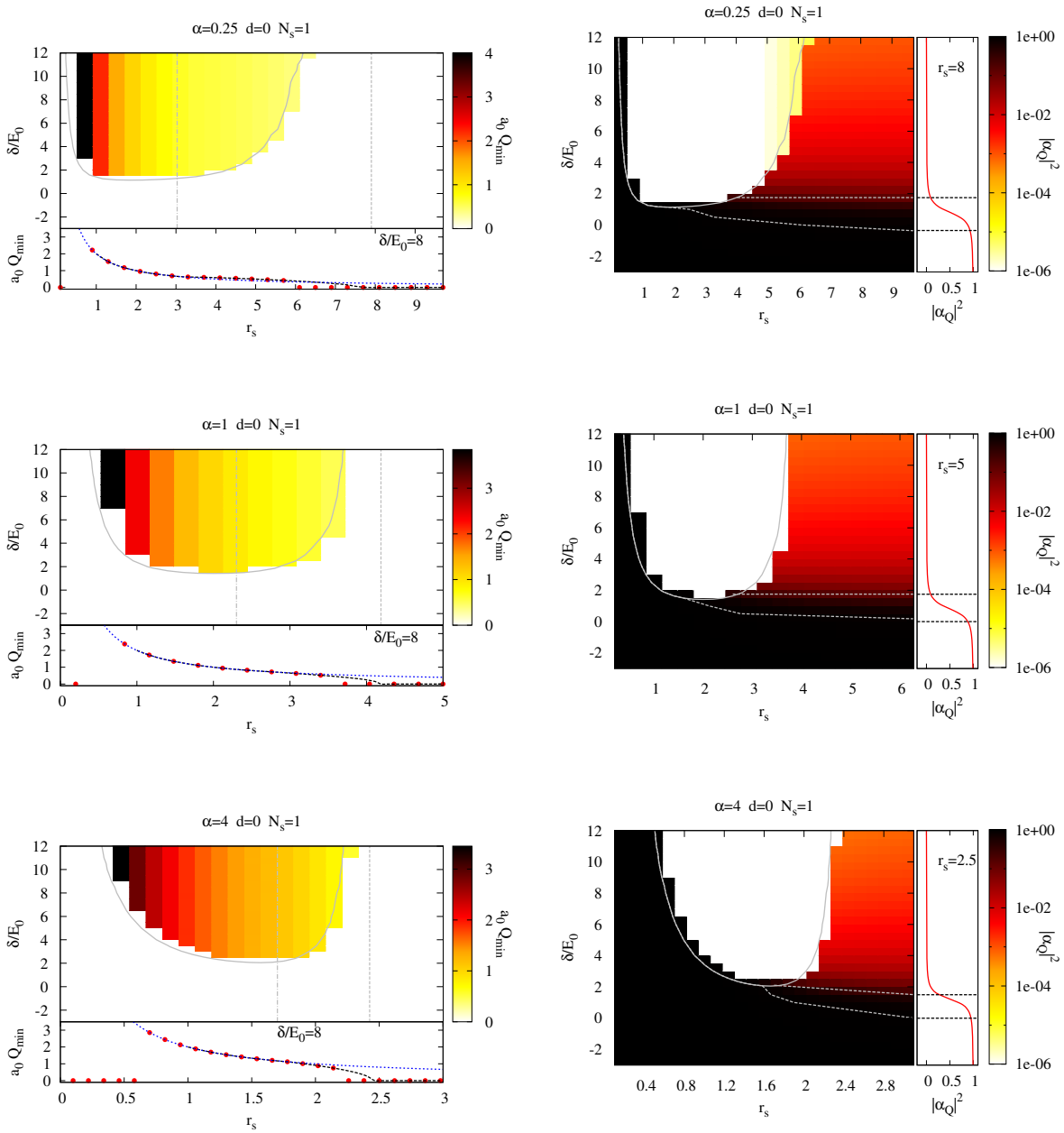

Figure 5.5: Same figure as Fig. 5.1 where now the Coulomb interaction considered is screened. The dot-dashed line is the N-FFLO transition threshold found in Chapter 4.

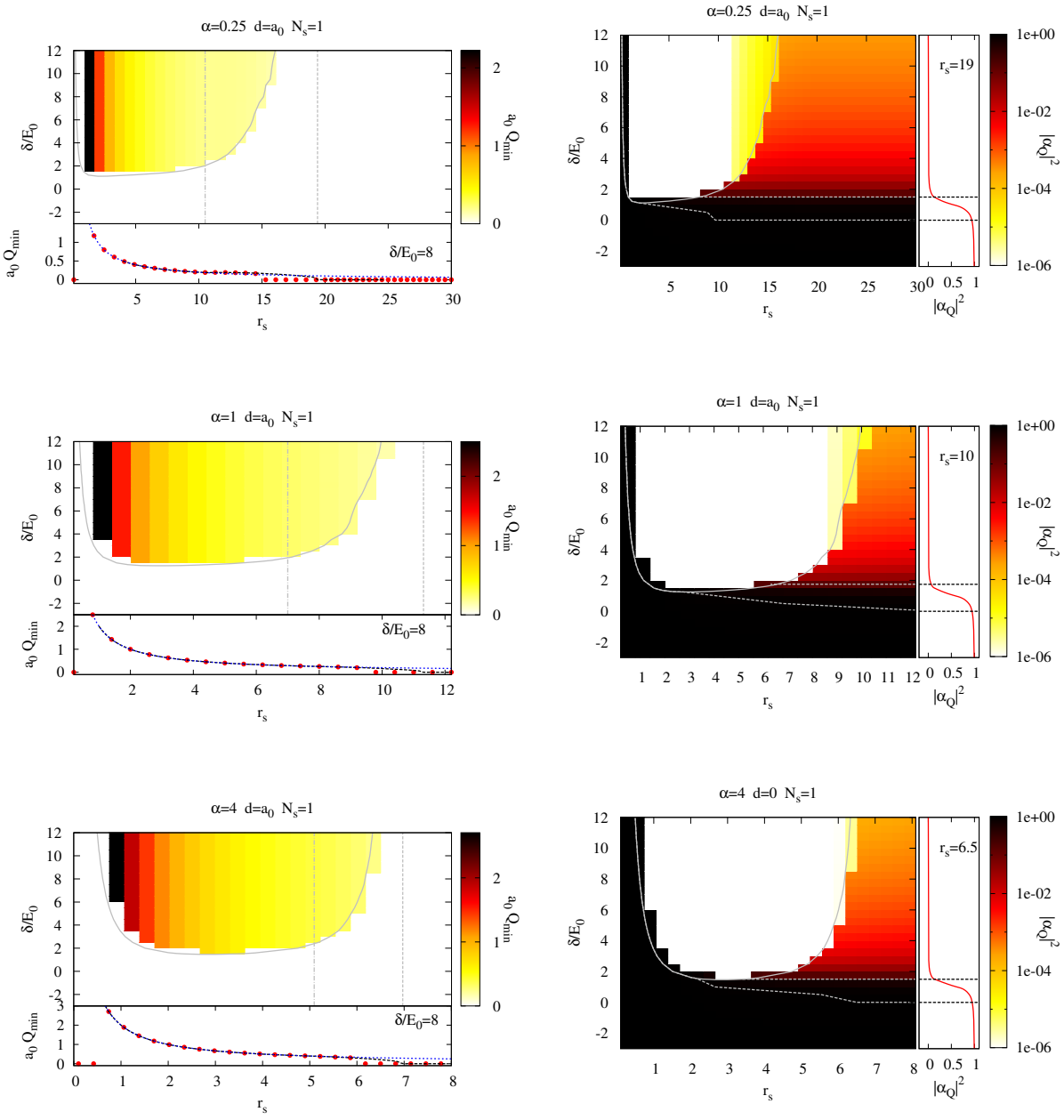

Figure 5.6: Same figure as Fig. 5.5 where now $d = a_0$.

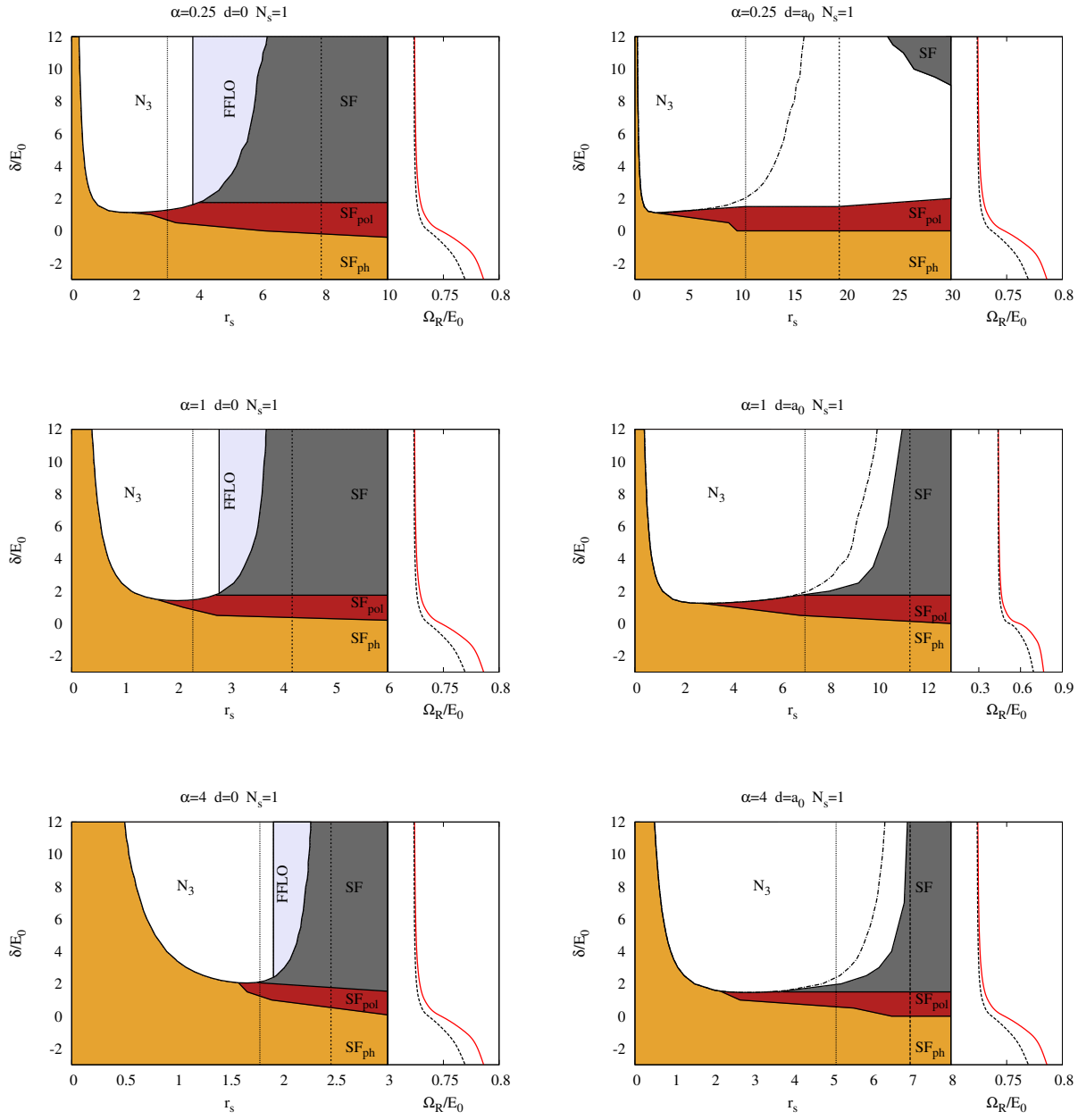

Figure 5.7: Same figure as Fig. 5.3, where now the interaction is screened, and normal phase is present.

Summary of results and conclusions

The conclusions in this case are quite similar to the ones previously highlighted. However, the most important result obtained studying the screened case is that now, not only the coupling to light is limiting the FFLO state, favouring the SF phase, but also the appearance of a phase where the finite momentum coupling between electrons and holes is only weakly mediated by finite momentum photons. In the single layer case the two effects allows the presence of an FFLO region, which, as in the unscreened case, at low density results more inhibited for $\alpha = 0.25$ than for $\alpha = 4$. However, more drastic effects happen when we consider bilayer structures, with a distance $d = a_0$. Here the normal phase completely suppress the FFLO, that can reappear only increasing the detuning. In this case the normal phase have an energy lower than the SF phase too, that again will reappear for greater δ, as clearly shown for $\alpha = 0.25$.

Appendices

A Gauss-Legendre method

Gauss-Legendre quadrature is a numerical integration method, which tries to solving the following function

$$\int_{-1}^{1} f(x)dx = \sum_{i=1}^{\infty} w_i f(x_i) \approx \sum_{i=1}^{n} w_i f(x_i) \tag{17}$$

by picking approximate value of n, w_i and x_i. While defined for the interval [-1,1], it is quite easy to convert the limits of the integration for an interval $[a, b]$:

$$\int_a^b f(x)dx = \frac{b-a}{2}\int_{-1}^{1} f\left(\frac{b-a}{2}x_i + \frac{b+a}{2}\right)dx \approx \sum_{i=1}^{n} w_i f\left(\frac{b-a}{2}x_i + \frac{b+a}{2}\right) . \tag{18}$$

The summation function is called Legendre-Gauss quadrature because the abscissae are defined as the n-roots of the n-order Legendre polynomial.

We choose to implement this method in our Python code, in order to solve the complex integrals in our study. The main advantage of this method is that it is an open integration, because doesn't integrate over the integration limits, and so this is pretty good to handle integrals with infinite range, especially when one expects a smooth function. Let's suppose to have

$$\int_a^{\infty} f(x)dx . \tag{19}$$

Changing the integration variable $x = tan\beta$, we have now an integral on a limited interval $\beta \in (\text{atan}(a), \pi/2)$. Applying the quadrature method, the function will be evaluated in equally spaced abscissae, that, after reconversion to the original integration variable x, will result more accumulated near a then for greater values of x.

A.1 Electron-hole bilayer with large density imbalance

The problem that we want to solve is the following eigenvalue equation

$$E\varphi_{\mathbf{k},\mathbf{Q}} = \left(\epsilon_{\mathbf{Q}-\mathbf{k},2} + \epsilon_{\mathbf{k},1} - \frac{1}{\Omega}\sum_{\mathbf{k}'<k_F} U^{sc}_{\mathbf{k}-\mathbf{k}'}\right)\varphi_{\mathbf{k},\mathbf{Q}} - \frac{1}{\Omega}\sum_{\mathbf{k}'>k_F} V^{sc}_{\mathbf{k}-\mathbf{k}'}\varphi_{\mathbf{k}',\mathbf{Q}} . \tag{20}$$

In this form this equations is not symmetric, and can not be transformed in a diagonalized matrix equation, solvable with a numerical approach.

To start with, we rescale energies by the exciton Rydberg E_0 and wave-vectors by the inverse exciton Bohr radius a_0 and introduce the dimensionless variables:

$$\tilde{k} = ka_0 \qquad \tilde{d} = \frac{d}{a_0} \qquad \tilde{\epsilon}_{\mathbf{k},1} = \frac{\epsilon_{\mathbf{k},1}}{E_0} = \frac{\alpha}{1+\alpha}\tilde{k}^2 \qquad \tilde{\epsilon}_{\mathbf{k},2} = \frac{\tilde{k}^2}{1+\alpha} . \tag{21}$$

In dimensionless units, changing from discrete to continuum, Eq. (20) becomes

$$\tilde{E}\phi_{\mathbf{k},\mathbf{Q}} = \left[\frac{\alpha}{1+\alpha}\tilde{k}^2 + \frac{\left(\tilde{Q}^2+\tilde{k}^2-2\tilde{Q}\tilde{k}cos\theta\right)}{1+\alpha} - \int_{k'<k_F}\frac{d^2k'}{(2\pi)^2}U_{\tilde{\mathbf{k}}-\tilde{\mathbf{k}}'}\right]\phi_{\mathbf{k},\mathbf{Q}} + \\ + \int_{k'>k_F}\frac{d^2k'}{(2\pi)^2}V_{\tilde{\mathbf{k}}-\tilde{\mathbf{k}}'}\phi_{\mathbf{k}',\mathbf{Q}}\,. \quad (22)$$

We can now solve the integrals using the Gauss-Legendre quadrature, obtaining again a discrete eigenvalue problem. To start, we want the eigenvector to be normalized.

$$1 = \frac{1}{2\pi}\int_0^{2\pi}d\theta\frac{1}{2\pi}\int_{2/r_s}^{\infty}d\tilde{k}\tilde{k}|\varphi_{\mathbf{kQ}}|^2 = \sum_{i_2}^{N_t}w_{i_2}^t\frac{1}{2\pi}\sum_{i_1}^{N_k}\tilde{w}_{i_1}^k\tilde{k}_{i_1}|\varphi_{i_1i_2\mathbf{Q}}|^2 = \sum_{i_2}^{N_t}\sum_{i_1}^{N_k}|\tilde{\varphi}_{i_1i_2\mathbf{Q}}|^2\,, \quad (23)$$

where we change the integration variables θ and $\tilde{k}$ to

$$t = \frac{\theta}{2\pi} \qquad t\in[0,1]$$
$$\tilde{k} = \tan\beta \qquad \beta\in\left[\text{atan}(\frac{2}{r_s}),\frac{\pi}{2}\right) \qquad \tilde{w}^k = \frac{w^\beta}{\cos^2\beta}\,,$$

with the transformation of $\tilde{k}$ useful to integrate over an infinite range. We also rescale

$$\tilde{\varphi}_{i_1i_2\mathbf{Q}} = \sqrt{\frac{w_{i_2}^t\tilde{w}_{i_1}^k\tilde{k}_{i_1}}{2\pi}}\varphi_{i_1i_2\mathbf{Q}}\,. \quad (24)$$

N_k and N_t represent the number of point used in the approximation of the integral, and $\tilde{w}^k$ and w^t are the weights. We can rewrite Eq. (20) as

$$\tilde{E}\tilde{\varphi}_{i_1i_2\mathbf{Q}} = \left(\tilde{k}_{i_1}^2 + \frac{\tilde{Q}^2}{1+\alpha} - \frac{2}{1+\alpha}\tilde{Q}\tilde{k}_{i_1}\cos(2\pi t_{i_2}) - \text{intra}(i_1)\right)\tilde{\varphi}_{i_1i_2\mathbf{Q}} \quad (25)$$

$$- \sum_{j_1}^{N_k}\sum_{j_2}^{N_t}\left(\frac{\sqrt{w_{i_2}^t\tilde{w}_{i_1}^k\tilde{k}_{i_1}w_{j_2}^t\tilde{w}_{j_1}^k\tilde{k}_{j_1}}\tilde{q}_{i_1i_2j_1j_2}e^{-\tilde{q}_{i_1i_2j_1j_2}\tilde{d}}}{\tilde{q}_{i_1i_2j_1j_2}^2 + N_s\frac{1+\alpha}{2\alpha}[\tilde{q}_{i_1i_2j_1j_2} - \sqrt{\tilde{q}_{i_1i_2j_1j_2}^2 - \frac{16}{r_s}}\Theta(\tilde{q}_{i_1i_2j_1j_2} - \frac{4}{r_s})]}\right)\tilde{\varphi}_{j_1j_2\mathbf{Q}} \quad (26)$$

where $\tilde{q}_{i_1i_2j_1j_2} = \sqrt{\tilde{k}_{i_1}^2 + \tilde{k}_{j_1}^2 - 2\tilde{k}_{i_1}\tilde{k}_{j_1}\cos[2\pi(t_{i_2}-t_{j_2})]}$. The intra-layer interaction term is given by

$$\text{intra}(i_1) = \int_0^1 dt'\int_0^{2/r_s}d\tilde{k}'\tilde{k}'\frac{\tilde{q}_{i_1,t'}}{\tilde{q}_{i_1,t'}^2 + N_s\frac{1+\alpha}{2\alpha}[\tilde{q}_{i_1,t'} - \sqrt{\tilde{q}_{i_1,t'}^2 - \frac{16}{r_s}}\Theta(\tilde{q}_{i_1,t'} - \frac{4}{r_s})]} \quad (27)$$

$$\tilde{q}_{i_1,t'} = \sqrt{\tilde{k}_{i_1}^2 + \tilde{k}'^2 - 2\tilde{k}_{i_1}\tilde{k}'\cos(2\pi t')}\,.$$

Following the same procedure, the dimensionless energy $\tilde{E}_N$ of the normal state $|\Psi_N\rangle$ is given by

$$\tilde{E}_{1,N} = \frac{\alpha}{1+\alpha}(\frac{2}{r_s})^2 - \text{intra}(\frac{2}{r_s})\,. \quad (28)$$

Note that, for an unscreened interaction, the intra-layer interaction term evaluate at k_F can be evaluated analytically:

$$\text{intra}_{unsc}(\tilde{k}_{i_1} = \frac{2}{r_s}) = \int_0^1 dt'\int_0^{2/r_s}d\tilde{k}'\tilde{k}'\frac{1}{\frac{4}{r_s^2} + \tilde{k}'^2 - \frac{4}{r_s}\tilde{k}'\cos(2\pi t')} = \frac{4}{\pi r_s}\,. \quad (29)$$

A.2 Electron-hole bilayer confined in a microcavity

Now we want to solve the coupled eigenvalue equations (5.6) and (5.7). Introducing the dimensionless variables

$$\tilde{k} = ka_0 \quad \tilde{d} = \frac{d}{a_0} \quad \tilde{\delta} = \frac{\delta}{E_0} \quad \tilde{\epsilon}_{\mathbf{k},1} = \frac{\epsilon_{\mathbf{k},1}}{E_0} = \frac{\alpha}{1+\alpha}\tilde{k}^2 \quad \tilde{\epsilon}_{\mathbf{k},2} = \frac{\tilde{k}^2}{1+\alpha} \quad \tilde{g} = \frac{g}{E_0 a_0}\,. \tag{30}$$

and following the same procedure as before

$$\begin{aligned}
\tilde{E}\tilde{\varphi}_{i_1 i_2 \mathbf{Q}} = &\left(\tilde{k}_{i_1}^2 + \frac{\tilde{Q}^2}{1+\alpha} - \frac{2}{1+\alpha}\tilde{Q}\tilde{k}_{i_1}\cos(2\pi t_{i_2}) - \text{intra}(i_1)\right)\tilde{\varphi}_{i_1 i_2 \mathbf{Q}} + \\
&- \sum_{j_1}^{N_k}\sum_{j_2}^{N_t}\left(\frac{\sqrt{w_{i_2}^t \tilde{w}_{i_1}^k \tilde{k}_{i_1} w_{j_2}^t \tilde{w}_{j_1}^k \tilde{k}_{j_1}}\tilde{q}_{i_1 i_2 j_1 j_2} e^{-\tilde{q}_{i_1 i_2 j_1 j_2}\tilde{d}}}{\tilde{q}_{i_1 i_2 j_1 j_2}^2 + N_s\frac{1+\alpha}{2\alpha}[\tilde{q}_{i_1 i_2 j_1 j_2} - \sqrt{\tilde{q}_{i_1 i_2 j_1 j_2}^2 - \frac{16}{r_s}}\Theta(\tilde{q}_{i_1 i_2 j_1 j_2} - \frac{4}{r_s})]}\right)\tilde{\varphi}_{j_1 j_2 \mathbf{Q}} + \\
&+ \sqrt{\frac{w_{i_2}^t \tilde{w}_{i_1}^k \tilde{k}_{i_1}}{2\pi}}\tilde{g}e^{-(\frac{\tilde{k}_{i_1}}{\tilde{k}_c})^2}\alpha_{\mathbf{Q}}
\end{aligned} \tag{31}$$

$$\tilde{E}\alpha_{\mathbf{Q}} = \left(\tilde{\delta} - 1 + \frac{\tilde{Q}^2}{2(m_C/m)}\right)\alpha_{\mathbf{Q}} + \sum_{j_1}^{N_k}\sum_{j_2}^{N_t}\sqrt{\frac{w_{j_2}^t \tilde{w}_{j_1}^k \tilde{k}_{j_1}}{2\pi}}\tilde{g}e^{-(\frac{\tilde{k}_{j_1}}{\tilde{k}_c})^2}\tilde{\varphi}_{j_1 j_2 \mathbf{Q}}\,, \tag{32}$$

where now the considered normalization condition is

$$\begin{aligned}
1 &= \frac{1}{2\pi}\int_0^{2\pi} d\theta \frac{1}{2\pi}\int_{2/r_s}^{\infty} dk k |\varphi_{\mathbf{k},\mathbf{Q}}|^2 + |\alpha_{\mathbf{Q}}|^2 \\
&= \sum_{i_2}^{N_t} w_{i_2}^t \frac{1}{2\pi}\sum_{i_1}^{N_k} w_{i_1}^k k_{i_1} |\varphi_{i_1 i_2 \mathbf{Q}}|^2 + |\alpha_{\mathbf{Q}}|^2 \\
&= \sum_{i_2}^{N_t}\sum_{i_1}^{N_k} |\tilde{\varphi}_{i_1 i_2 \mathbf{Q}}|^2 + |\alpha_{\mathbf{Q}}|^2\,,
\end{aligned} \tag{33}$$

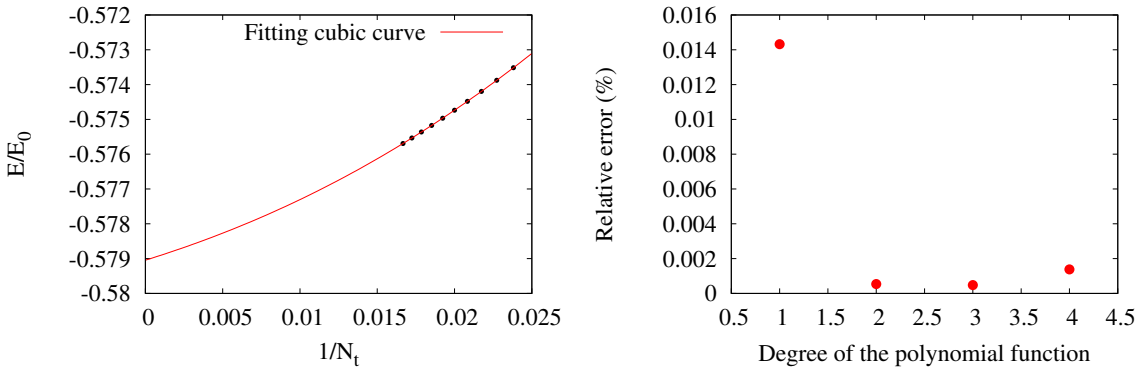

Figure 8: Left panel: lowest rescaled eigenvalue E/E_0 (black dots) for $\alpha = 0.25$, $d = a_0$, $N_s = 0$, $r_s = 1$ and $Q = k_F$, as a function of $1/N_t$ for $N_k = 3N_t/2$. The solid line represents a fit with a cubic polynomial from which we extract the y-intercept giving the minimum relative error. It is clearly convergent for $N_t \to \infty$ Right panel: relative error obtained for the y-intercept for the same data on the left panel by using a fitting polynomial of different degrees.

B Convergence with respect to N_t and N_k

We numerically solve the discretized eigenvalue coupled equation (25) and find the lowest eigenvalue E for a finite number of points N_t (angle) and N_k (momentum). For the intra-layer term (27) we also use a Gauss-Legendre quadrature for both angular $t \in [0, 1]$ and momentum $\tilde{k}' \in [0, \frac{2}{r_s}]$ integrals with a fixed number of points N_t and N_k. The choice of both N_t and N_k doesn't affect significantly the result and we have chosen $N_t = N_k = 100$. The numerical convergence of this term can be tested by comparing it with the analytical result obtained for unscreened interactions (29).

We have then studied the convergence of the lowest eigenvalue with respect to both N_k and N_t. We have find faster convergence by fixing $N_k = 3N_t/2$ and extracted the $N_t \to \infty$ limit of the lowest eigenvalue by fitting the data as a function of $1/N_t$ with a cubic polynomial and extracting the y-intercept. An example is shown in the left panel of Fig. 8, where we have plotted the lowest rescaled eigenvalue E/E_0 (black dots) for $\alpha = 0.25$, $r_s = 1.0$, $Q = k_F$ and unscreened interactions $N_s = 0$ as a function of $1/N_t$ for $N_k = 3N_t/2$. We extrapolate the $N_t \to \infty$ eigenvalue by fitting the data with polynomials of different degrees (right panel). We obtain that the lowest relative error of the y-intercept is given by the fit with a cubic polynomial. The error obtained in the extrapolation procedure is generally very low (never higher than $\approx 0.01\%$) but it depends on the specific choice of the system parameters.

We have implemented an automatic extrapolation procedure in our code so that to eliminate the dependence on the two cut-offs N_k and N_t.

References

[1] Steven T. Cundiff, Tianhao Zhang, Alan D. Bristow, Denis Karaiskaj, and Xingcan Dai. Optical two-dimensional fourier transform spectroscopy of semiconductor quantum wells. *Accounts of Chemical Research*, 42(9):1423–1432, 2009.

[2] J. Frenkel. On the transformation of light into heat in solids. i. *Phys. Rev.*, 37:17–44, 1931.

[3] Gregory H. Wannier. The structure of electronic excitation levels in insulating crystals. *Phys. Rev.*, 52:191–197, 1937.

[4] Schwoerer M. and Wolf H. C. Wiley-Blackwell, 2008.

[5] Nasser Peyghambarian, Stephan W. Koch, and Andre Mysyrowicz. *Introduction to Semiconductor Optics*. Prentice-Hall, Inc., 1993.

[6] G. Bastard. *Wave mechanics applied to semiconductor heterostruc- tures*. Les Editions de Physique, Paris, 1989.

[7] David A. B. Miller. Optical physics of quantum wells, 1996.

[8] R. P. Smith. Quantitative measurements of many-body exciton dynamics in gaas quantum-well structures. Master's thesis, 2010.

[9] Ronald L. Greene and K. K. Bajaj. Binding energies of wannier excitons in gaas-$ga_{1-x}al_xas$ quantum-well structures in a magnetic field. *Phys. Rev. B*, 31:6498–6502, 1985.

[10] R. C. Miller, D. A. Kleinman, W. T. Tsang, and A. C. Gossard. Observation of the excited level of excitons in gaas quantum wells. *Phys. Rev. B*, 24:1134–1136, 1981.

[11] A. Siarkos, E. Runge, and R. Zimmermann. Center-of-mass properties of the exciton in quantum wells. *Phys. Rev. B*, 61:10854–10867, 2000.

[12] Alexey Kavokin, Jeremy J. Baumberg, Guillaume Malpuech, and Fabrice P. Laussy. *Microcavities*. Oxford University Press, Inc., New York, NY, USA, 2008.

[13] C. Fabry and A. Pérot. Théorie et applications d'une nouvelle méthode de spectroscopie interférentielle. *Ann. de Chim. et de Phys*, 16, 1899.

[14] J. Keeling, F. M. Marchetti, M. H. Szymańska, and P. B. Littlewood. Collective coherence in planar semiconductor microcavities. *Semiconductor Science and Technology*, 22(5), 2007.

[15] Sun Yongbao. Exciton-polaritons in thermal equilibrium : from bose-einstein condensation to exciton-polaritonics. Master's thesis, 2017.

[16] E. M. Purcell. Spontaneous emission probabilities at radio frequencies. *Phys. Rev.*, 69, 1947.

[17] G. Khitrova, H. M. Gibbs, M. Kira, S. W. Koch, and A. Scherer. Vacuum rabi splitting in semiconductors. *Nature Physics*, 2, 2006.

[18] J.J. Hopfield. *Phys. Rev.*, 112, 1958.

[19] Gunnar Björk, Susumu Machida, Yoshihisa Yamamoto, and Kazuhiro Igeta. Modification of spontaneous emission rate in planar dielectric microcavity structures. *Phys. Rev. A*, 44:669–681, 1991.

[20] C. Weisbuch, M. Nishioka, A. Ishikawa, and Y. Arakawa. Observation of the coupled exciton-photon mode splitting in a semiconductor quantum microcavity. *Phys. Rev. Lett.*, 69:3314–3317, 1992.

[21] Fei Xue, Fengcheng Wu, Ming Xie, Jung-Jung Su, and A. H. MacDonald. Microscopic theory of equilibrium polariton condensates. *Phys. Rev. B*, 94, 2016.

[22] R. N. Hall, G. E. Fenner, J. D. Kingsley, T. J. Soltys, and R. O. Carlson. Coherent light emission from gaas junctions. *Phys. Rev. Lett.*, 9(9), 1962.

[23] S. De Palo, F. Rapisarda, and Gaetano Senatore. Excitonic condensation in a symmetric electron-hole bilayer. *Phys. Rev. Lett.*, 88:206401, 2002.

[24] J. Schleede, A. Filinov, M. Bonitz, and H. Fehske. Phase diagram of bilayer electron-hole plasmas. *Contributions to Plasma Physics*, 52(10):819–826.

[25] S. I. Shevchenko. Theory of superconductivity of systems with pairing of spatially separeted electrons and holes. *Sov. J. Low Temp. Phys.*, 2, 1976.

[26] M. Kellogg, J. P. Eisenstein, L. N. Pfeiffer, and K. W. West. Vanishing hall resistance at high magnetic field in a double-layer two-dimensional electron system. *Phys. Rev. Lett.*, 93:036801, 2004.

[27] M. Kellogg, I. B. Spielman, J. P. Eisenstein, L. N. Pfeiffer, and K. W. West. Observation of quantized hall drag in a strongly correlated bilayer electron system. *Phys. Rev. Lett.*, 88:126804, 2002.

[28] E. Tutuc, M. Shayegan, and D. A. Huse. Counterflow measurements in strongly correlated gaas hole bilayers: Evidence for electron-hole pairing. *Phys. Rev. Lett.*, 93:036802, 2004.

[29] University of Cambridge Semiconductor Physics Group. Electron hole bilayer. *https://www.sp.phy.cam.ac.uk/research/2d-transport/drag*.

[30] A. F. Croxall, K. Das Gupta, C. A. Nicoll, M. Thangaraj, H. E. Beere, I. Farrer, D. A. Ritchie, and M. Pepper. Anomalous coulomb drag in electron-hole bilayers. *Phys. Rev. Lett.*, 101, 2008.

[31] J. A. Seamons, C. P. Morath, J. L. Reno, and M. P. Lilly. Coulomb drag in the exciton regime in electron-hole bilayers. *Phys. Rev. Lett.*, 102, 2009.

[32] Giovanni Vignale and A. H. MacDonald. Drag in paired electron-hole layers. *Phys. Rev. Lett.*, 76:2786–2789, 1996.

[33] Ben Yu-Kuang Hu. Prospecting for the superfluid transition in electron-hole coupled quantum wells using coulomb drag. *Phys. Rev. Lett.*, 85:820–823, 2000.

[34] Mussie Beian, Mathieu Alloing, Edmond Cambril, Carmen Gomez Carbonell, Johann Osmond, Aristide Lemaître, and François Dubin. Long-lived spin coherence of indirect excitons in gaas coupled quantum wells. *EPL (Europhysics Letters)*, 110(2):27001.

[35] Byrnes Tim, Kim Na Young, and Yamamoto Yoshihisa. Exciton–polariton condensates. *Nature Physics*, 10, 2014.

[36] Peter Cristofolini, Gabriel Christmann, Simeon I. Tsintzos, George Deligeorgis, George Konstantinidis, Zacharias Hatzopoulos, Pavlos G. Savvidis, and Jeremy J. Baumberg. Coupling quantum tunneling with cavity photons. *Science*, 336(6082):704–707, 2012.

[37] O. Kyriienko, A. V. Kavokin, and I. A. Shelykh. Superradiant terahertz emission by dipolaritons. *Phys. Rev. Lett.*, 111:176401, 2013.

[38] A. V. Nalitov, D. D. Solnyshkov, N. A. Gippius, and G. Malpuech. Voltage control of the spin-dependent interaction constants of dipolaritons and its application to optical parametric oscillators. *Phys. Rev. B*, 90:235304, 2014.

[39] R. V. Gorbachev, A. K. Geim, M. I. Katsnelson, K. S. Novoselov, T. Tudorovskiy, I. V. Grigorieva, A. H. MacDonald, S. V. Morozov, K. Watanabe, T. Taniguchi, and L. A. Ponomarenko. Strong coulomb drag and broken symmetry in double-layer graphene. *Nature Physics*, 8, 2012.

[40] A. Imamoglu, R. J. Ram, S. Pau, and Y. Yamamoto. Nonequilibriumcondensates and lasers without inversion: Exciton-polariton lasers. *Phys. Rev. A*, 53, 1996.

[41] C. Comte and P. Nozières. Exciton bose condensation: the ground state of an electron-hole gas. *Journal de Physique*, 43:1069–1081, 1982.

[42] P B Littlewood, P R Eastham, J M J Keeling, F M Marchetti, B D Simons, and M H Szymanska. Models of coherent exciton condensation. *Journal of Physics: Condensed Matter*, 16(35):S3597, 2004.

[43] Kenji Kamide and Tetsuo Ogawa. What determines the wave function of electron-hole pairs in polariton condensates? *Phys. Rev. Lett.*, 105:056401, 2010.

[44] Tim Byrnes, Tomoyuki Horikiri, Natsuko Ishida, and Yoshihisa Yamamoto. Bcs wavefunction approach to the bec-bcs crossover of exciton-polariton condensates. *Phys. Rev. Lett.*, 105:186402, 2010.

[45] Keldysh L. V. and Kopaev Y. V. *Sov. Phys.—Solid State*, 6:2219, 1965.

[46] Peter Fulde and Richard A. Ferrell. Superconductivity in a strong spin-exchange field. *Phys. Rev.*, 135:A550–A563, 1964.

[47] A.I. Larkin and Yu.N. Ovchinnikov. Nonuniform state of superconductors. *Sov. Phys. JETP*, 20, 1965.

[48] J. R. Varley and D. K. K. Lee. Structure of exciton condensates in imbalanced electron-hole bilayers. *Phys. Rev. B*, 94:174519, 2016.

[49] M. M. Parish, F. M. Marchetti, and P. B. Littlewood. Supersolidity in electron-hole bilayers with a large density imbalance. *EPL (Europhysics Letters)*, 95(2):27007, 2011.

[50] P. Noziéres. *Some comments on Bose-Einstein condensation*, chapter 2, pages 15–19. Cambridge University Press, 1995.

[51] S. N. Bose. *Z. Phys.*, 26.

[52] A. Einstein. *Sitzungberichte, Pressische Akademie der Wis- senshaften*, 1, 1925.

[53] L. Landau. Theory of the superfluidity of helium ii. *Phys. Rev.*, 60:356–358, 1941.

[54] Oliver Penrose and Lars Onsager. Bose-einstein condensation and liquid helium. *Phys. Rev.*, 104:576–584, 1956.

[55] C. N. Yang. Concept of off-diagonal long-range order and the quantum phases of liquid he and of superconductors. *Rev. Mod. Phys.*, 34:694–704, 1962.

[56] A. Griffin, D. W. Snoke, and S. Stringari. *Bose-Einstein condensation.* Cambridge University Press, 1995.

[57] A. J. Leggett. *Modern trends in the theory of condensed matter.* Springer, 1980.

[58] P. Senellart and J. Bloch. Nonlinear emission of microcavity polaritons in the low density regim. *Phys. Rev. Lett.*, 82, 1999.

[59] R. Butté, G. Delalleau, A. I. Tartakovskii, M. S. Skolnick, V. N. Astratov, J. J. Baumberg, G. Malpuech, A. Di Carlo, A. V. Kavokin, and J. S. Roberts. Transition from strong to weak coupling and the onset of lasing in semiconductor microcavities. *Phys. Rev. B*, 65, 2002.

[60] Hui Deng, Gregor Weihs, Charles Santori, Jacqueline Bloch, and Yoshihisa Yamamoto. Condensation of semiconductor microcavity exciton polaritons. *Science*, 298(5591):199–202, 2002.

[61] G Malpuech, A Kavokin, A Di Carlo, and J.J. Baumberg. Polariton lasing by exciton-electron scattering in semiconductor microcavities. *Phys. Rev. B*, 65, 2002.

[62] A. Huynh, J. Tignon, G. Keller, Ph. Roussignol, C. Delalande, R. André, R. Romestain, and Le Si Dang. Collision broadening in ii-vi semiconductor microcavities. *Phys. Rev. B*, 68:165340, 2003.

[63] M. Richard, J. Kasprzak, R. André, R. Romestain, Le Si Dang, G. Malpuech, and A. Kavokin. Experimental evidence for nonequilibrium bose condensation of exciton polaritons. *Phys. Rev. B*, 72:201301, 2005.

[64] M. W. Zwierlein, J. R. Abo-Shaeer, A. Schirotzek, C. H. Schunck, and W. Ketterle. Vortices and superfluidity in a strongly interacting fermi gas. *Nature*, 435:1047–1051, 2005.

[65] M. H. Anderson, J. R. Ensher, M. R. Matthews, C. E. Wieman, and E. A. Cornell. Observation of bose-einstein condensation in a dilute atomic vapor. *Science*, 269(5221), 1995.

[66] A. Aspect, E. Arimondo, R. Kaiser, N. Vansteenkiste, and C. Cohen-Tannoudji. Laser cooling below the one-photon recoil energy by velocity-selective coherent population trapping. *Phys. Rev. Lett.*, 61:826–829, 1988.

[67] Wolfgang Ketterle and N.J. Van Druten. Evaporative cooling of trapped atoms. volume 37 of *Advances In Atomic, Molecular, and Optical Physics*, pages 181 – 236. Academic Press, 1996.

[68] S. Schmitt-Rink, D. S. Chemla, and D. A. B. Miller. Theory of transient excitonic optical nonlinearities in semiconductor quantum-well structures. *Phys. Rev. B*, 32:6601–6609, 1985.